UC Berkeley
UC Berkeley Electronic Theses and Dissertations

Title

Engineered virus-like particles for the efficient delivery of therapeutics

Permalink

https://escholarship.org/uc/item/1v69j98k

Author

Pistono, Paige Elizabeth

Publication Date

2024

Peer reviewed|Thesis/dissertation

eScholarship.org Powered by the California Digital Library
University of California

Engineered virus-like particles for the efficient delivery of therapeutics

by

Paige Pistono

A dissertation submitted in partial satisfaction of the

requirements for the degree of

Doctor of Philosophy

in

Chemistry

in the

Graduate Division

of the

University of California, Berkeley

Committee in charge:

Professor Matthew Francis, Chair
Professor Alanna Schepartz
Professor Andreas Stahl

Spring 2024

Engineered virus-like particles for the efficient delivery of therapeutics

Copyright 2024
by
Paige Pistono

Abstract

Engineered virus-like particles for the efficient delivery of therapeutics

by

Paige Pistono

Doctor of Philosophy in Chemistry

University of California, Berkeley

Professor Matthew Francis, Chair

Virus-like particles (VLPs) comprise the structural components of a virus that are recombinantly expressed as self-assembling, non-infectious particles. The development of VLPs for biomedical applications is of interest due to their improved safety profile and ease of production compared to live viruses. The first recombinant VLP-based vaccine was approved for human papillomavirus (HPV) in 2009, and many more have since been approved or are in clinical development. VLPs are also of interest for applications such as drug delivery, but they need to be further engineered with new functionalities for cargo encapsulation, release, and targeting. Throughout this work, we describe the advancements in the development of VLPs for drug delivery applications as well as the engineering of bacteriophage MS2-based VLPs for improved cellular uptake and drug delivery. Using the single amino acid fitness landscape of the MS2 coat protein, we were able to design locally supercharged mutants with positive surface charge and increased cellular uptake. The biophysical properties and biological activity of the best-performing mutants were characterized, and mutant capsids were able to deliver a cytotoxic cancer drug in cell culture with greater than 50-fold increases in efficacy compared to wild-type MS2 in proof-of-concept drug delivery experiment. To study the effects of particle size on cellular uptake, we created a new set of locally supercharged MS2 variants combined with a single point mutation that was previously shown to create smaller capsids. These engineered triple mutants retained their ability to internalize and deliver small-molecule drugs into mammalian cells, but exhibited increased thermal stability and unexpected assembly geometries. Through experimental measurements and computational predictions, we investigate how these mutations at the VLP interfaces affect particle size and stability. This work demonstrates the utility of genetic screening methods such as fitness landscaping for VLP engineering and explores the use of biophysical and *in silico* characterization methods to assess VLP properties and function for biomedical applications.

Dedicated to my mother, Mary Jones Pistono

Contents

Contents **ii**

List of Figures **iv**

List of Tables **vi**

1 Introduction **1**
1.1 Abstract . . . 1
1.2 Introduction . . . 1
1.3 Virus-like particle structure and function . . . 2
1.4 Self-assembly of virus-like particles . . . 7
1.5 Engineered virus-like particles with new functions for drug delivery . . . 12
1.6 Conclusion . . . 21

2 Fitness landscape-guided engineering of locally supercharged virus-like particles with enhanced cell uptake properties **22**
2.1 Abstract . . . 22
2.2 Introduction . . . 23
2.3 Results and Discussion . . . 24
2.4 Conclusion . . . 41
2.5 Materials . . . 44
2.6 Methods . . . 45
2.7 Acknowledgements . . . 56

3 Exploring the effects of intersubunit interface mutations on virus-like particle structure and stability **57**
3.1 Abstract . . . 57
3.2 Introduction . . . 58
3.3 Results and Discussion . . . 59
3.4 Conclusion . . . 76
3.5 Materials . . . 76
3.6 Methods . . . 79

3.7 Supplementary Figures 85
3.8 Acknowledgements 85

Bibliography **111**

List of Figures

1.1 Governing principles of structural virology 3
1.2 Enveloped and non-enveloped VLPs 5
1.3 Virus-like particles with unexpected assembly states 9
1.4 Genetic approaches for VLP engineering 11
1.5 Peptide display on virus-like particles 12
1.6 Chemical modification of virus-like particles 13
1.7 Enzymatic modification of virus-like particles 15
1.8 Functionalization of VLPs for drug delivery 17

2.1 Apparent fitness scores for MS2 variants with positive surface charge 25
2.2 HPLC SEC traces of MS2 CP variants 27
2.3 LC-MS analysis of MS2 CP variants 28
2.4 Fluorophore-maleimide coupling to MS2 29
2.5 LC-MS analysis of MS2-fluorescein conjugates 30
2.6 MS2-fluorescein uptake into mammalian cells 31
2.7 Fluorescence microscopy images of MS2 cellular uptake 32
2.8 Cellular uptake of MS2 variants with all possible mutations at residues 71 & 73 33
2.9 Calculated pK_as at residues 71 & 73 35
2.10 LDH cytotoxicity assay 37
2.11 MTS cytotoxicity assay & hemolysis assay 38
2.12 Biophysical characterization of MS2 CP variants 39
2.13 Cellular uptake of MS2 in the presence of endocytosis inhibitors 40
2.14 MMAE coupling to MS2 42
2.15 Cellular delivery of MMAE to glioblastoma cells 43

3.1 Structures of wild-type and miniMS2 capsids 60
3.2 LC-QTOF-MS analysis of S37P/N87C MS2 CP variants 61
3.3 Characterization of MS2 S37P capsid assembly states 62
3.4 Characterization of MS2 rod-like assembly state 63
3.5 MS2 variant diameter measurements 64
3.6 Thermal shift assay 65
3.7 MS2 input structures for molecular dynamics simulations 67
3.8 Molecular dynamics simulations of different MS2 capsid assembly states 68

3.9 Comparison of hydrogen bonding occupancy and interdimer contact angles between different MS2 input structures 69
3.10 Fluorophore labeling of MS2 S37P/N87C variants 70
3.11 LC-QTOF-MS analysis of MS2 fluorophore labeling 71
3.12 Cellular internalization of locally supercharged MS2 S37P variants 72
3.13 Flow cytometry histograms of MS2-Rho uptake into U-251 MG cells 73
3.14 MS2 conjugation to MMAF 74
3.15 MS2 conjugation to MMAF 75
3.16 Delivery of MMAF with locally supercharged MS2 variants 77
3.17 Additional thermal shift assay data 85
3.18 TEM images of MS2 S37P/T71R/N87C capsids 86
3.19 TEM images of MS2 S37P/T71K/N87C capsids 87
3.20 TEM images of MS2 T71R/G73R/N87C capsids 88
3.21 TEM images of MS2 T71R/G73K/N87C capsids 89
3.22 TEM images of MS2 T71K/G73R/N87C capsids 90
3.23 TEM images of MS2 T71K/G73K/N87C capsids 91
3.24 TEM images of MS2 N87C capsids 92
3.25 TEM images of MS2 T71R/N87C capsids 93
3.26 TEM images of MS2 S37P/N87C capsids 94
3.27 TEM images of MS2 G73R/N87C capsids 95
3.28 TEM images of MS2 G73K/N87C capsids 96
3.29 TEM images of MS2 S37P/T71K/G73R/N87C capsids 97
3.30 TEM images of MS2 S37P/T71R/G73K/N87C capsids 98
3.31 TEM images of MS2 S37P/G73R/N87C capsids 99
3.32 TEM images of MS2 S37P/G73K/N87C capsids 100
3.33 TEM images of MS2 T71K/N87C capsids 101
3.34 Measured diameters of MS2 variants 102
3.35 wtMS2 6CP2-2MS2 molecular dynamics 103
3.36 wtMS2 10CP2-2MS2 molecular dynamics 103
3.37 S37P 10CP2-4ZOR molecular dynamics 104
3.38 S37P 6CP2-2MS2 molecular dynamics 105
3.39 S37P 10CP2-2MS2 molecular dynamics 106
3.40 T71K/G73R 6CP2-2MS2 molecular dynamics 107
3.41 T71K/G73R 10CP2-2MS2 molecular dynamics 107
3.42 S37P/T71K/G73R 6CP2-2MS2 molecular dynamics 108
3.43 S37P/T71K/G73R 10CP2-2MS2 molecular dynamics 109
3.44 S37P/T71K/G73R 10CP2-4ZOR molecular dynamics 110

List of Tables

1.1 Clinically approved VLP-based vaccines 7
1.2 Clinically approved viral gene therapies 19

2.1 Apparent fitness scores for R/K mutants at positions 71 and 73 25
2.2 MS2 CP fluorescein-maleimide modification masses 26
2.3 Fluorescence intensity values for MS2-fluorescein internalization into HeLa cells 34
2.4 Fluorescence intensity values for multiple cell types screen 34
2.5 Isoelectric point (pI) estimates 35
2.6 pK_a estimates 36
2.7 Fluorescence intensity values for endocytosis inhibitors screen 41
2.8 MS2 CP MMAE modification masses 43
2.9 Primer names for EMPIRIC cloning to generate MS2 variants 46
2.10 Primer sequences for EMPIRIC cloning to generate MS2 variants 47
2.11 Molecular mechanics conformational search results 55

3.1 TEM capsid diameter measurements 64
3.2 Thermal shift assay 65
3.3 Expected and observed masses of S37P/N87C MS2 CP variants. 70
3.4 Fluorescence intensity values for MS2-fluorescein internalization into U-251 MG cells 72
3.5 MS2 CP MMAF modification masses 76
3.6 Primer sequences for QuickChange site-directed mutagenesis to generate MS2 S37P variants 79

Acknowledgments

Thank you to everyone who has supported me in my graduate school and other endeavors over the past five years. So many people have helped create an environment filled with support and advice and have been there for me during many amazing and challenging times. First, I would like to thank my family for supporting me throughout my education. They have always encouraged me to realize my dreams and do my best work. Mom, Grandpa Jones, Grandma Jones, Grandpa Pistono, Grandma Pistono, and Dad have always encouraged me to take my education seriously and allowed me to pave my way forward in my future career. Even though my sisters, Molly and Jenna, probably won't end up getting PhDs (because they're both way cooler than me), I think we've all become academic weapons in our own right, and I am so excited to see what their futures hold. Molly will be an amazing doctor thanks to her fantastic communication skills, genuinely caring personality, and excellent work ethic. Jenna will stand out in any career she pursues, thanks to her diligent study habits, mature composure, calmness, and ability to get along with everyone.

My mom, Mary, has been there for me from the very beginning (literally). She encouraged me to explore a wide range of interests and hobbies from a young age. That helped spark my interest in science and appreciate other areas such as art, music, and languages. Although I might have been annoyed by her pushing me to do my best in school sometimes, she taught me to figure things out independently, take accountability for my actions, and try to do things right the first time.

Grandpa Jones has supported my education and is always eager to hear my latest research updates. I hope Grandpa Pistono is proud that there will be at least one more academic in the Pistono family. He always loved quizzing me and my sisters and loved sharing his knowledge of history and gardening with us.

Next, I would like to thank my friends, old and new, for continually being there for me and always being a joy to spend time with. Johanna and I have been best friends since first grade (thanks, Ms. Duke), and we've continued to grow together as classmates in grade school, middle school, high school, college classmates, and roommates at UW-Madison, and now we are both pursuing our PhDs in Chemistry in the Bay Area. I don't know how that happened, but it's awesome! It has been amazing to count on our friendship during grad school, and I don't know what I'll do once we finally have to live more than one hour apart (or maybe that will never happen). If that happens, I will miss our weekly adventure meetups, whether hiking, skiing, camping, checking out a museum, or just generally exploring the Bay Area.

My friends and roommates, Annika and Cameron, have gone through all of grad school with me. We especially spent a lot of time together during the pandemic, where weird lab work shift schedules were accompanied by lots of time spent drinking Natty Light on the patio and playing endless rounds of Catan. I am also grateful for my weekly hikes with Jack and Cameron during that time, which allowed us to get out of the house and explore some awesome trails around the Bay Area. Annika and I have gotten involved with the East Bay natural winemaking community (shout out to TyTy wine!), bringing us closer over

our shared love of science, wine, and food and making us feel like we are part of a greater community. Cameron is always a joy to talk to about science things, and I can thank him for introducing me to the hyperpop music genre and our now shared love of 100 gecs. Feeling like part of and contributing to a community has always been important to me. I feel grateful to have been a part of so many different and awesome groups during college and graduate school. At UW-Madison, I found lifelong best friends in groups like Spanish Club, Alpha Chi Sigma, and the Granada study abroad chicas plus Tom, with the bonus of us all having similar academic interests. I also want to thank my greater Berkeley Chemistry cohort and friend group for always being down to do something fun on a weeknight or a weekend and becoming a large part of my community here in the Bay Area.

I want to thank all of my current and previous mentors for helping me grow into the scientist I am today. Trisha was my first mentor as an undergrad doing research for the Bio 152 independent project, and she taught me a lot about science communication and how to think about a project. I learned many important analytical chemistry techniques from Trisha and Sam, as well as how to work on projects with others and independently. Netta was my second mentor in the Hutt lab (go zebrafish!). I learned many essential molecular biology and microscopy skills from Netta, David, and the rest of the Hutt lab. I experienced how fun it can be to work in a lab setting with the right group of people. Both of these experiences led me to apply to grad school and set me up to be successful in an environment where independence and problem-solving are essential skills.

Finally, I would like to thank everyone in the Francis lab I worked with during my graduate school career. This is going to be a long one. First, Matt has been one of the best mentors and bosses to ask for as a PhD student. He is a professor who truly cares about the happiness and needs of his students and wants to make sure everyone in the lab has the opportunity to succeed in their project and whatever future career path they take, whether academic, industry, or non-scientific careers. I've learned the importance of telling a story, communicating my project to different audiences, and trying to solve a problem just because it's interesting, which usually leads to new or unexpected results. I will always be grateful for our lab ski trips and summer trips, which further help usurp the traditional power dynamic between advisors and their students and create an incredibly unique, caring, and supportive environment in the Francis lab.

Over the past five years, I've worked with many past and present students and postdocs in the Francis lab. They have all been integral in one way or another, whether through their hard work in helping to keep the lab running, continued mentorship, insightful thoughts and suggestions, or just being awesome people to work with. Dan was my rotation mentor and my first introduction to the Francis lab. As the resident god of MS2, coffee, and figuring out how to do awesome new techniques like fitness landscaping and machine learning, he was (and still is) always my go-to when I have questions about a project's bigger picture and technical details. Even though I broke Lady Gaggia on one of the first days of my rotation, he still allowed me to work with him. He provided the foundation for learning the Francis lab basics, from molecular biology and protein expression to bioconjugation.

Paul and I have worked together since the depths of COVID lockdown in 748 and have

collaborated extensively on MS2 drug delivery projects. "Good ideas Paul" is a fitting namesake, as he truly knows everything and everyone's projects. Paul is one of the hardest-working people I know and is always willing to help develop a new method, troubleshoot the QTOF, or do a cell experiment with someone. He cares so much about the lab and has also been a great mentor to many undergrads and rotation students. I am lucky to have met and been able to work with Junyi for the past 2.5 years. She has grown into an outstanding young scientist, and I can't wait to see what her future holds at Yale and beyond. She has mastered the basics of molecular biology. She has contributed so much to the miniMS2 project, where she characterized many different mutants and developed new methods, such as the thermal shift assay. She's also secretly hilarious, and it's always fun to hear what K-pop concerts she attended over the weekend.

Although Johnathan wasn't officially my mentor, he has been one of the most helpful people in the lab regarding suggestions or advice regarding my project. He always had something interesting to say during subgroup, and I believe he will be an amazing professor one day. Deborah has brought joy and excitement about science to the lab from day one. She is always down to talk about anything, science-related or not, and always down for random adventures. I am thankful for our friendship over the past few years, and I can't wait to see what she accomplishes in the future. Erin and I have had the pleasure of working together on MS2-related projects during her rotation and later when she joined the lab. As her papa, watching her grow into a more independent scientist over the past year has been amazing. I love working with Erin because she will always try to figure something out but is also not afraid to ask many questions and is always down for a midday chat session. Paloma is one of the most positive and joyful people I have ever met, and her energy fills every room she walks into. She is so excited about science and fun to talk to, making the lab a better place for everyone. Kate is another positive and rational force in the lab. She has put a lot of effort into planning and organizing important things for the lab, like dealing with safety and getting new instruments installed. She is also an amazing communicator, whether about science- or people-related things. I always love listening to her subgroups and group meetings because they are so easy to understand. I have enjoyed Jack's presence in the lab and appreciate his hard work ethic and eagerness to work on a collaborative project. We've also been able to bond over things like music and thrifting. I'm very excited to see what he accomplishes in the future. Derek's lab presence has helped create a fun-loving, positive, and accepting environment. I look up to him so much for being his authentic self every single day, and I wish I was confident enough to wear some of his amazing outfits. He is very efficient in the lab, and I strive to achieve that level of experimental planning. I'm always happy when I see Jenny in the lab. Even as an undergrad, she has become such an important part of the Francis lab, has contributed a lot to cell culture, and has helped with some experiments for my project. I am so excited to see what she accomplishes at UC Davis. Avery is another Francis lab fashion icon who is just thrilled about science. Her Twitter is legendary, and I am excited to see what she accomplishes during the rest of her time in the lab. Amanda is a joy to work with. She is among the most humble, kind, and levelheaded people I have met. When we worked together, she cared a lot about the lab and was an

amazing ski trip buddy, EYH co-chair, and conference travel partner. Wendy is so helpful, positive, and always eager to chat with anyone. Whenever I walked into 733 with a question, I knew someone there would be there to help me. Marco is a Francis lab stalwart. He put so much work into the lab, in the form of being in charge of the QTOF and TOF, as well as creating an environment where it's easy to get excited about science every single day. He is such a positive force, and I look forward to seeing what he accomplishes with Catena. Arya was a great lab manager and lab mate. She was instrumental in getting the lab running after the move and was very good at helping to organize things in general. I am excited to follow her graduate career at UC Davis and see what she accomplishes. Hannah has been a great person to work with on MS2-related projects. She always brings positive energy to the lab and is a great mentor to others. Valerie is a joy to be around. She is hilarious and always excited about science. She has helped me a lot in using various structural techniques, such as SAXS and X-ray crystallography, to characterize MS2. Vanessa is a rockstar both in and out of the lab. It is always so inspiring to hear about her latest athletic and home construction-related accomplishments, and she was even spotted working out at the climbing gym with a broken leg. Jamie is like a lab mom to me. She is someone everyone looks up to for being a great scientist and a caring person who gives great advice and is not afraid to stand up for herself and others. Alex is such a kind person and was a great lab mate. Kylee's energy is unmatched, and she has done a great job of making everyone in the lab feel included by organizing events for people's birthdays and other important occasions. Nick has been a constant grounding force in the lab and has always been very good at organizing things like lab cleanup and moving to Stanley. It is always fun to hear what he did over the weekend. Preeta has become an important part of team IDP in a short time and is very good at developing new methods systematically. There are so many other people I've had the chance to work with in the lab, even if we didn't interact much on a daily basis. Thank you to Annika, Alexi, Tatiana, Ian, Celine, Alan, Sarah, Lauren, Jing, Kristen, Cameron, Nicole, Cardy, Riley, Casey, Zoey, and everyone else who has made the Francis lab a great place to be over the years.

Chapter 1

Introduction

1.1 Abstract

Virus-like particles (VLPs) are useful platforms for the study of biomolecular self-assembly and possess several features that make them ideal candidates for development as vaccines, diagnostic tools, and drug delivery vehicles. VLPs can be recombinantly expressed at high yields, can resemble natural viruses or be engineered with new functionalities, and are non-infectious and therefore a safe alternative to using live viruses for therapeutic applications. VLP capsids can be genetically or chemically modified to facilitate the encapsulation of cargo or the multivalent display of antigens and targeting groups. This chapter summarizes the current state of the art in VLP technology and strategies for the continued development of VLPs for biomedical applications. VLP structure and function, the self-assembly of VLPs, and methods to engineer VLPs with new features for drug delivery are discussed here.

1.2 Introduction

Virus-like particles (VLPs) are composed of viral structural components that can self-assemble when recombinantly expressed as non-infectious particles. VLPs are safe alternatives to live viruses for use as vaccines and gene therapies, as they lack a viral genome and other necessary components for viral replication. The development of VLPs as vaccines has been successful, with clinically approved recombinant vaccines for hepatitis B, hepatitis E, malaria, and human papillomaviruses. Their ability to multivalently display surface antigens makes them highly immunogenic and especially promising for developing new vaccines and immunotherapy agents. VLPs are also useful for the encapsulation and delivery of a wide range of therapeutic payloads, including small molecules, nucleic acids, and proteins. Different VLPs are ideal for specific applications, and further engineering of VLPs with new functionalities is required for optimal cargo encapsulation, release, and targeting. Both enveloped and non-enveloped VLPs have been developed from mammalian, plant, and bacteriophage viruses. Human-derived enveloped VLPs have shown promise for the targeted

delivery of therapeutic proteins and nucleic acids (i.e., gene editing ribonucleoproteins) with minimal engineering, while plant- and bacteriophage-derived non-enveloped VLPs are ideal for the delivery of small molecules and require further engineering for targeted delivery of other payloads. This review chapter focuses on the underlying principles of VLP structure and function, the use of VLPs to study protein self-assembly, and methods to develop VLPs with new functions for drug delivery applications.

1.3 Virus-like particle structure and function

Virus-like particles are self-assembling protein nanoparticles that possess similar structural features to live viruses while remaining non-infectious due to the absence of a viral genome and replication machinery. VLPs can be made of natural viral proteins or designed with new functionalities, providing a platform to study self-assembly and create new systems for a wide range of applications at the intersection of biology and nanotechnology. Protein engineering techniques such as computational protein design and directed evolution can be used to create new protein particles with virus-like architectures that are completely *de novo* or based on non-viral structural proteins. Notable examples include the use of HBV- and HPV-based VLPs for vaccines against hepatitis B and cervical cancer. The ability of VLPs to elicit robust immune responses makes them especially suited as candidates for vaccine and immunotherapeutic development. Other applications of interest are the use of VLPs for gene therapy, drug delivery, diagnostic, and agricultural applications. Discussed here are the structural principles of VLP assemblies, techniques to study and engineer VLP self-assembly and other properties, and methods to engineer VLPs for applications such as drug delivery.

Governing principles of structural virology

All viruses have several common characteristics, such as the ability to encapsulate and protect their DNA or RNA genomes within a protein capsid. However, they can differ in virion architecture, with icosahedral, helical, or more complex assemblies. The governing principles of structural virology over the past 60 years are known as *genetic economy* and *quasi-equivalence*. At the fundamental level, icosahedral viral capsids comprise 20 equilateral triangle faces. Viral capsid proteins assemble to form each triangular face of the capsid; the simplest form is three capsid proteins, defined as the structural unit [1]. The high degree of symmetry found in viral architectures was termed *genetic economy* by Watson and Crick as a way to describe the viral genome favoring symmetric architectures with reduced coding costs, generating coding capacity for other viral components [2]. A single structural unit can repeat to form a complete icosahedron, creating a capsid with 20 structural units and 60 capsid protein monomers, also known as a $T = 1$ icosahedron. The structural unit can be repeated to form a larger icosahedral face and particles with a larger T (triangulation) number (Figure 1.1), enabling the formation of particles with more than 60 subunits. The functional organization and geometric constraints that govern the assembly of icosahedral virus par-

ticles are widely discussed problems in structural virology. As first described by Caspar and Klug, not all capsid protein monomers will be present in identical conformations in an icosahedral virus with well-defined symmetry [3]. This theory is known as *quasi-equivalence*, where chemically identical capsid proteins can occupy conformationally unique spaces in order to assemble higher-order icosahedral structures [3]. The fundamental assumption of quasi-equivalence is that the viral capsid is composed of the same capsid proteins with similar intermolecular interactions, but the chemical structure of each capsid protein monomer may be slightly deformed relative to the other monomers. Although these theories have dominated structural virology, some capsid protein structures cannot be classified through these descriptions, indicating that the fundamental design principles and genetic constraints of viral architecture are still not fully understood [4].

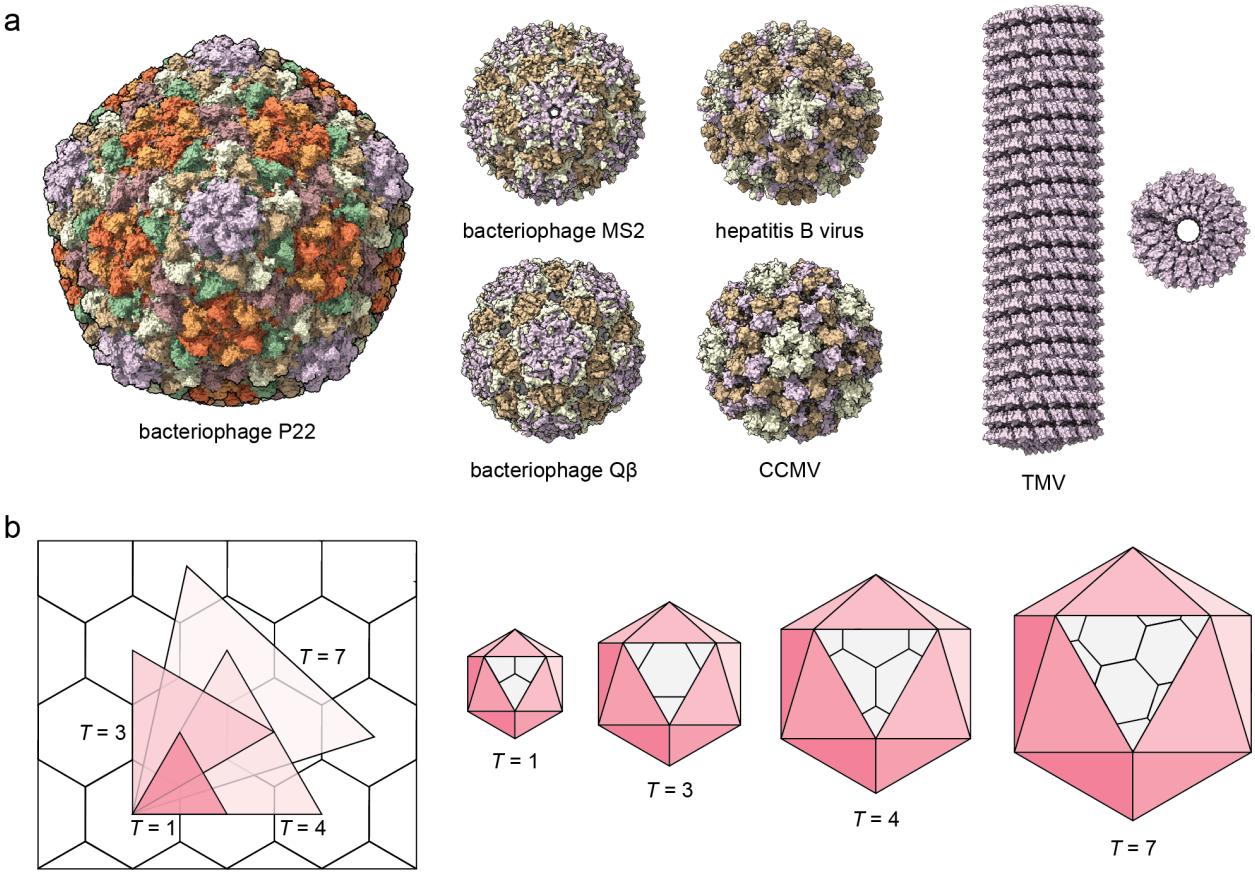


Figure 1.1: **(A)** Structures of common virus-like particle (VLP) capsid protein assemblies. Shown here are P22 (PDB ID: 5UU5), MS2 (PDB ID: 2MS2), Qβ (PDB ID: 1QBE), hepatitis B virus core antigen protein (PDB ID: 1QGT), cowpea chlorotic mottle virus (CCMV, PDB ID: 1CWP), and tobacco mosaic virus (TMV, PDB ID: 2TMV). **(B)** One triangular face of an icosahedron is superimposed on a hexagonal grid to show the four smallest icosadedral structures ($T = 1$, $T = 3$, $T = 4$, $T = 7$, dark pink to light pink, respectively) that can be assembled according to the Caspar and Klug model of viral assembly. The corresponding icosahedral assemblies are shown to the right. This figure panel is adapted from [4].

Non-enveloped virus-like particles

Non-enveloped VLPs are composed of many copies of a single or multiple capsid structural proteins (Figure 1.2). Due to the absence of a lipid envelope, non-enveloped VLPs are typically more stable than their enveloped counterparts. This stability makes them attractive candidates for vaccines and other drug delivery applications where cold-chain storage requirements are costly and impractical in developing countries or for agricultural applications. The most simple capsid structure comprises a single coat protein that assembles into icosahedral capsid structures and can be derived from enveloped and non-enveloped viruses such as HBV, HPV, plant viruses, and single-stranded RNA bacteriophages like MS2 and Qβ. These single-monomer capsids are of interest due to their ease of expression in both prokaryotic and eukaryotic systems. Non-enveloped VLPs made of multiple structural proteins are more complex in production. Complex, non-enveloped VLPs derived from viruses such as enterovirus or rotavirus need to be expressed in yeast, insect cells, or plant cells to ensure proper folding and assembly [5–8]. Aside from their widespread use as recombinant vaccines, non-enveloped VLPs can be co-opted for intracellular delivery of small molecule, protein, and nucleic acid cargo. Cargo molecules can be loaded through covalent modification or by non-covalent interactions with the inner surface of VLP capsids. These cargo-loaded VLPs possess a wide range of uses, including vaccines, drug delivery, diagnostic, biocatalytic, and agricultural applications.

Enveloped virus-like particles

Enveloped virus-like particles comprise multi-layer internal structures that assemble below a lipid membrane (Figure 1.2). Due to their requirement for expression in eukaryotic cells, enveloped VLPs obtain their lipid membranes from their host cell during the budding process. Surface glycoproteins can be expressed to anchor into the lipid envelope of these VLPs, enabling surface display of target antigens for cellular targeting and immune recognition. The assembly and release of enveloped VLPs is more complex than that of non-enveloped VLPs, and thus, the formation and engineering of these VLPs is more complex and not as well understood. The ability of enveloped VLPs to cross lipid bilayers during cellular exit (budding) and entry (fusion) increases the efficacy of cytosolic delivery of encapsulated cargo. The design of enveloped VLPs must incorporate specific viral structural components depending on the virus type to ensure successful VLP formation and budding. The expression of coronavirus and flavivirus glycoproteins alone can lead to the release of enveloped VLPs, while the budding of most retroviruses occurs via the presence of the major structural Gag core protein and does not require the presence of glycoproteins [9, 10].

The development of engineered enveloped VLPs is of particular interest for genome editing applications. In recent work, the Doudna and Liu labs have both developed engineered VLPs for the targeted delivery of therapeutic gene editing proteins such as CRISPR-Cas9 ribonucleoproteins (RNPs), base editors, and prime editors [11–14]. For gene editing agent delivery, these systems can engineer existing retroviral scaffolds for RNP and transgene

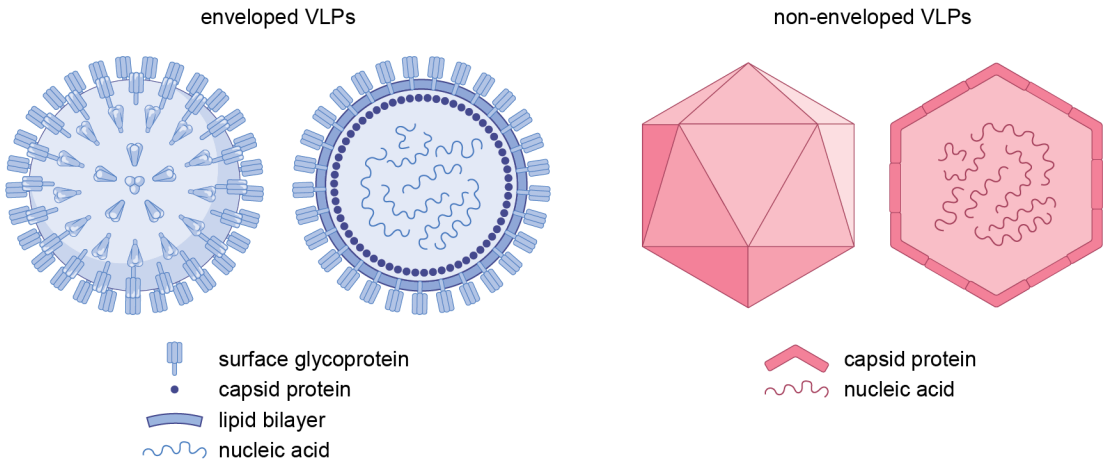


Figure 1.2: Diagram showing the main structural components of enveloped (left, blue) and non-enveloped (right, pink) VLPs.

delivery [12] or create new, DNA-free VLPs that can efficiently package and deliver different gene editing RNPs [11]. To package Cas9 in lentiviral HIV-1 VLPs, Cas9 was fused to the C-terminus of the Gag polypeptide with an HIV-1 protease cleavable linker in between Gag and Cas9 to promote separation upon virion maturation [12]. These enveloped HIV-1 particles were shown to target and edit CD4+ T cells in an *ex vivo* co-culture environment with CD8+ T cells, providing an adaptable platform for targeted immune cell engineering [12]. Lentiviral and retroviral scaffolds offer great promise for protein delivery due to their flexibility, allowing for protein cargo incorporation without the rigid symmetry constraints typical of non-enveloped icosahedral viruses [15]. To enable intracellular delivery of base editors, ABE8e, an adenine base editor, was fused to the C-terminus of the Friend murine leukemia virus (FMLV) Gag polypeptide with an FMLV protease-cleavable linker peptide in between the two sequences [11]. Base editor(BE)-VLPs were produced by transfecting HEK293 cells with plasmids encoding the FMLV Gag-ABE8e construct, wild-type FMLV Gag–pro–pol polyprotein, the vesicular stomatitis virus G (VSVG) envelope glycoprotein, and sgRNA targeting HEK293T cell genomic sites 2 or 3. *In vitro* transduction of HEK293T cells with purified BE-VLPs resulted in editing efficiencies exceeding 97% [11]. This system was then used for *in vivo* base editing in mice, leading to a 78% reduction in Pcsk9 levels and partial restoration of vision in a genetic blindness mouse model.

Expression and purification of virus-like particles

VLPs can be recombinantly expressed in prokaryotic (bacteria) or eukaryotic (yeast, baculovirus/insect cell, plant, mammalian) expression systems. An appropriate expression system must be used to ensure that proper protein folding, post-translational modifications, and quaternary structure are achieved. Bacterial systems can be used to express non-enveloped

VLPs, such as those derived from bacteriophages [16]. *E. coli* expression systems are preferred for the production and distribution of low-cost vaccines in the developing world and have demonstrated the ability to produce safe and effective VLP-based vaccines. Hecolin® and HeberNasvac® are the first clinically approved VLP-based vaccines derived from *E. coli* for vaccination again HEV and HBV, respectively [17]. Yeast, insect, and mammalian expression systems are used to produce enveloped VLPs that require glycosylation or other PTMs for VLP function and appropriate immune response. Yeast expression systems such as *S. cerevisiae* and *P. pastoris* are frequently used for recombinant protein and VLP production due to their ability to create high-yielding and cost-effective post-translationally modified proteins. To date, there are three VLP-based vaccines, Engerix-B® (HBV), Gardasil® (HPV), and Mosquirix® (malaria) produced in *S. cerevisiae* that are FDA-approved [18–20]. Baculovirus-based insect expression systems can be used for the fast-paced production of vaccines against viruses like influenza with rapidly evolving surface antigens between outbreaks. Like yeast-based expression, baculovirus-based systems can produce enveloped and non-enveloped VLPs with PTMs and complex, multi-subunit assembly states. Cervarix®, an FDA-approved HPV vaccine, is produced using an insect expression system in *T. ni* cells [21, 22]. Mammalian cell expression systems are useful platforms for producing VLPs with multiple structural proteins and complex PTMs and glycosylation patterns. Common cell lines for VLP production include baby hamster kidney-21 (BHK-21), human embryonic kidney 293 (HEK293), Chinese hamster ovary (CHO), Vero, and avian cell lines [16]. Traditional live-attenuated and inactivated vaccines made from infectious viruses are produced in mammalian cells. Notably, the seasonal influenza vaccine is manufactured in chicken eggs, but this platform lacks key features such as ease of scale-up and short development timelines that are crucial for the fast development of vaccines during a pandemic [23–25]. About 70% of all recombinant proteins are produced in mammalian cells, and therapeutics (mAbs, etc.) produced this way are associated with high costs due to challenging scale-up and risk of viral contamination [26]. Due to these challenges, only one clinically approved VLP-based vaccine is manufactured in mammalian cell lines (Table 1.1).

Many VLP-based vaccines are optimized for downstream purification by using a secretion-based expression system [27]. Secretion-based expression systems are most commonly used in mammalian, insect, and yeast-based expression systems but can also be engineered in bacterial systems to avoid cell lysis and extra protein extraction steps. As a general approach, a secretion signal peptide is appended to the recombinant VLP proteins to enable recognition by the host cell secretory pathway [28]. Downstream purification steps include VLP clarification, concentration, intermediate purification, and final polishing via methods such as ion exchange chromatography (IEX) or size exclusion chromatography (SEC) [27].

Clinical development of virus-like particle-based vaccines

Over the past three decades, virus-like particles have been continuously developed for use in vaccines, and several VLP-based vaccines are commercially available to protect against hepatitis B virus (HBV), human papillomaviruses (HPV), hepatitis E virus (HEV), and malaria

(Table 1.1). Many HBV VLP-based vaccines are clinically approved, all based on the hepatitis B surface antigen (HBsAg), and new third-generation vaccines incorporate three HBV surface antigens [29]. HBsAg VLP-based vaccines have been in development since the 1980s. The first generation isolated HBsAg particles from the blood of infected individuals, and subsequent generations developed vaccines with yeast and mammalian expression systems [30–32]. The FDA has also approved several VLP-based vaccines for the prevention of HPV infections that can lead to cervical and other cancers. Gardasil® and Gardasil9® are made of recombinant VLPs that self-assemble into particles comprised of HPV major capsid protein L1 and adjuvanted with aluminum [29]. There are many other VLPs currently in clinical trials that cover a wide range of infectious and non-infectious diseases, including SARS-CoV-2, influenza, malaria, Alzheimer's, HIV, melanoma, RSV, hPMV, and HPV [33, 34].

Name	Company	Year	Disease Target	Adjuvant	Production
Cervarix®	GSK	2009	L1 HPV	aluminum	baculovirus
Gardasil®	Merck	2006	L1 HPV	aluminum	*S. cerevisiae*
Gardasil9®	Merck	2014	L1 HPV	aluminum	*S. cerevisiae*
Cecolin®	Innovax	2019	L1 HPV	-	*E. coli*
Engerix-B®	GSK	2018	HBV S	aluminum	*P. pastoris*
Recombivax HB®	Merck	2018	HBV S	aluminum	*S. cerevisiae*
Hepilsav-B®	Dynavax	2017	HBV S	CpGs	*H. polymorpha*
PreHevbrio®	VBI Vaccines	2021	HBV S	aluminum	mammalian
Hecolin®	Innovax	2012	HEV 239	-	*E. coli*
Mosquirix®	GSK	2022	malaria CSP	AS01	*S. cerevisiae*
R21/Matrix-M®	Novavax	2023	malaria CSP	Matrix-M	*P. pastoris*

Table 1.1: A list of current clinically approved VLP-based vaccines[33, 35–37].

1.4 Self-assembly of virus-like particles

Protein self-assembly is a complex process that relies on interactions between protein monomers, yet these interactions can be easily disrupted. Many methods can be used to study self-assembly and engineer new self-assembling protein-based materials. Virus-like particles are a target of particular interest for protein engineering, as they assemble into well-defined particles and provide a platform for creating particles with new morphologies and functionalities. Protein-nucleic acid interactions play a critical role in the self-assembly process for VLPs, and particles with alternative assembly geometries can arise when capsid proteins are recombinantly expressed without the complete genomic RNA and associated packaging signals. Genetic screening methods can be used to study both the protein-protein and protein-nucleic acid interactions that are important for VLP self-assembly. These methods include protein fitness landscaping and directed evolution, which require a genotype-to-phenotype link for high-throughput sequencing-enabled quantification of mutant abundance after functional selections. Virus-like particles are an appealing platform for these studies because of their natural ability to encapsulate nucleic acids. Non-viral proteins can also be

used to create virus-like architectures with new functionalities. Protein nanoparticles can be engineered from existing self-assembling proteins or designed *de novo* using computational methods. These methods can be used to create VLPs and protein nanoparticles with tunable properties such as size, shape, thermostability, acid sensitivity, and chemical reactivity.

Natural occurrence of mixed assembly states

Although viral capsid assembly is well-defined, VLP populations with various mixed assembly states have been identified in work using various bacteriophage capsids from the *Leviviridae* family. These single-stranded RNA (ssRNA) viruses comprise 89 identical copies of a coat protein dimer and one maturation protein monomer that enables infection of *E. coli* through interaction with the F-pilus [38]. Differences in encapsulated RNA sequence and length when expressing the VLP recombinantly versus working with the infectious virion with the full viral genome can lead to unexpected structural assembly states. In establishing a model of genomic RNA (gRNA) inside of the bacteriophage Qβ, researchers discovered a variety of alternative capsid structures during wild-type phage infection and recombinant overexpression [39]. During wild-type phage infection, a small percentage of $T = 4$, prolate, and oblate Qβ capsids was observed and purified with gel filtration chromatography, which was previously unidentified in viral fractions purified via density gradient (Figure 1.3). An increased proportion of oblate and prolate capsid assembly states was identified during recombinant expression of just the Qβ coat protein, possibly due to the presence of shorter RNA sequences. A similar population of mixed capsid assembly states was identified in recombinantly expressed bacteriophage MS2 [40]. The MS2 coat protein (CP) was recombinantly co-expressed with a 155 bp sequence containing the TR stem loop that is known to drive capsid self-assembly, and both the expected $T = 3$ icosahedral capsid as well as a $T = 4$ capsid were identified (Figure 1.3). Structural analysis of the $T = 4$ variant revealed that this assembly state alters the maturation protein incorporation site, prohibiting infectious viron formation in the $T = 4$ assembly state.

Genetic screening methods to study self-assembly

Understanding the underlying forces of capsid assembly remains a challenging goal. The self-assembly of protein shells is governed by complex protein-protein and protein-nucleic acid interactions, and it is difficult to predict how specific amino acid mutations will affect viral function and architecture. Genetic screening methods can be used to describe how mutations affect VLP properties of interest quantitatively. One such method, termed protein fitness landscaping, is used to evaluate how systematic mutations (i.e., single amino acid mutations) affect the properties of a protein of interest [42]. This technique utilizes high-throughput sequencing to determine how a specific protein mutation affects a measurable phenotypic readout, such as viral capsid assembly or thermostability. Fitness landscapes have been generated for infectious viruses, including HIV, influenza, polio, and others, using infectivity as the selection readout [43–48].

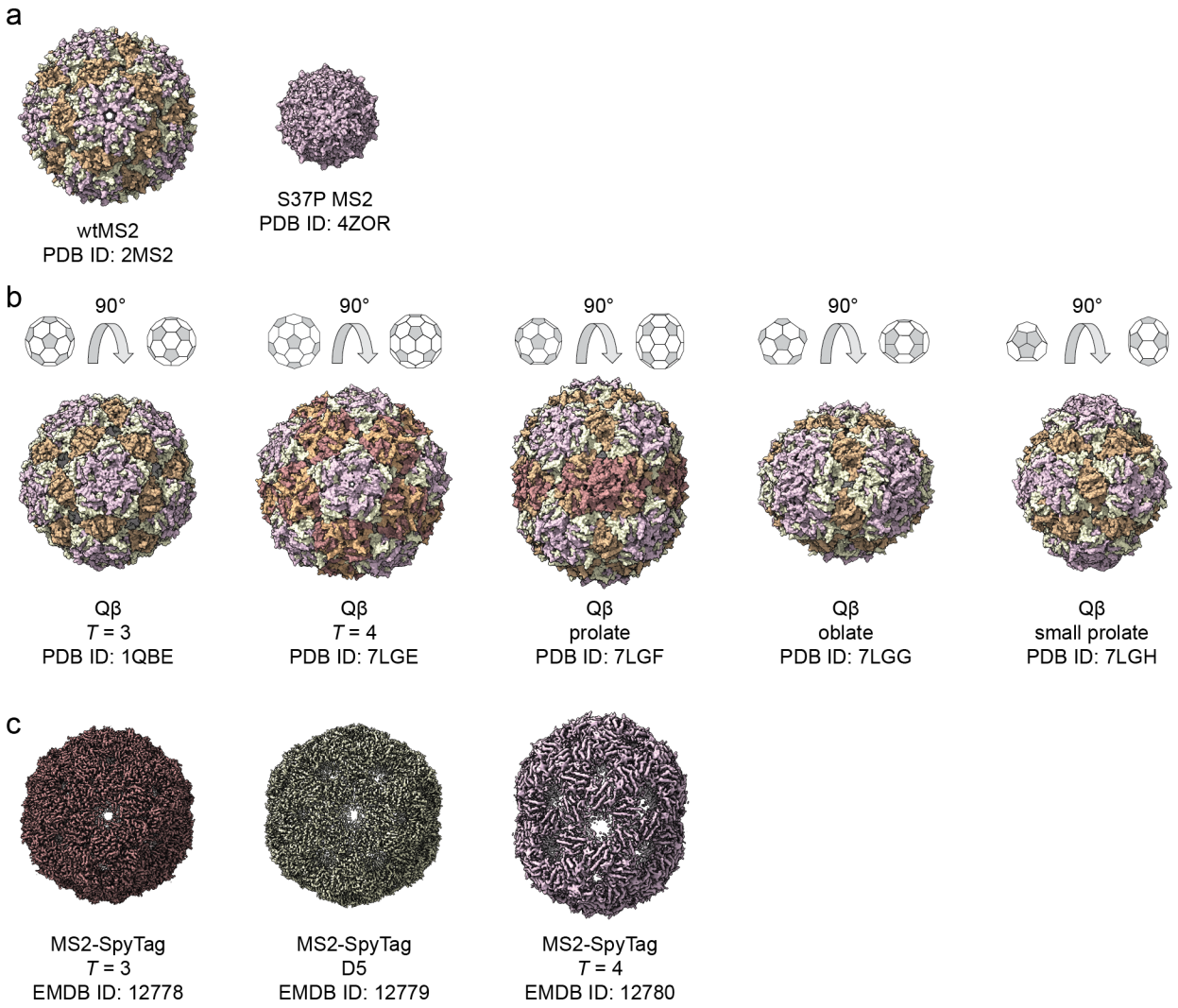


Figure 1.3: **(A)** Structures of wild-type MS2 (PDB ID: 2MS2) $T = 3$ capsid and S37P MS2 (PDB ID: 4ZOR) $T = 1$ capsid assemblies. **(B)** Cryo-EM structures of Qβ VLP symmetries. Shown from left to right are $T = 3$ (PDB ID: 1QBE), $T = 4$ (PDB ID: 7LGE), prolate (PDB ID: 7LGF), oblate (PDB ID: 7LGG), and small prolate (PDB ID: 7LGH) assemblies. This figure panel is adapted from [39]. **(C)** Cryo-EM density maps of MS2-SpyTag symmetries found when the SpyTag sequence was inserted into the MS2 AB loop. This figure panel is adapted from [41].

Our lab uses fitness landscaping to study the functional properties of bacteriophage MS2. Using a method called SyMAPS (Systematic Mutagenesis and Assembled Particle Selection), all single amino acid mutations at every position of the MS2 coat protein sequence were generated and selections were performed to identify mutants with tunable chemical and physical properties such as self-assembly competency, thermostability, and acid sensitivity (Figure 1.4) [49]. SyMAPS has also been used to study the influence of multiple mutations on MS2 structure and function, creating 2-dimensional and 3-dimensional protein fitness landscapes. A double mutant library was created to study the effects of epistasis at the FG loop, a highly mutable loop, allowing for the discovery of acid-sensitive mutants with increased thermostability properties relative to those identified in the 1-dimensional MS2 fitness landscape [49]. The effect of amino acid insertions at the MS2 FG loop and N-terminus has also been studied via 3-dimensional fitness landscapes, allowing for the identification of sequences that enable improved site-specific bioconjugation and VLP targeting for drug delivery applications [50, 51]. SyMAPS has also been used to identify MS2 VLPs with different assembly geometries and further establish the design rules related to shifting particle size [52–54]. A single amino acid variant, MS2[S37P], was identified and characterized as a smaller, $T = 1$ icosahedral capsid, which could be useful for exploring the effects of particle size on MS2 performance in drug delivery applications (Figure 1.3) [52].

There are many cases of genetic modification of VLPs to display targeting peptide sequences as N- or C-terminal genetic fusions or loop insertions (Figure 1.5). Of the *Leviviridae* bacteriophages, the PP7, MS2, and Qβ capsids are common VLP scaffolds in various biomedical applications. These VLPs are amenable to peptide extension and loop insertion to varying degrees [55–57]. Functional peptides displayed on VLP surfaces are useful for vaccine antigen presentation, cellular targeting, and peptide display for the identification of diagnostic and immunotherapeutic targets and epitope identification [58–60]. In some cases, loop insertion into fused-dimer variants of MS2 and PP7 resulted in populations of VLPs with unexpected assembly states, such as $T = 4$ capsids [41, 55]. The ability to control VLP particle size and geometry is an attractive feature, allowing capsid proteins to be engineered with new morphologies and properties. Recently, DNA origami has been used to direct the assembly of viral capsid proteins in a controlled manner to create multi-layer capsid-coated DNA origami structures [61]. Protein engineering techniques have also been used to design asymmetric HBV capsids with an engineered heterodimer, $\mathrm{CP149_{His}Cp149_{Y132A}}$, that allows for the assembly of hybrid capsids with a single, removable heterodimer hexamer nucleus surrounded by homodimers [62].

Protein engineering and *de novo* design of self-assembling virus-like architectures

Experimental and computational protein engineering techniques are used to design virus-like architectures with new functionalities. Protein cages found in nature, such as bacterial microcompartments, ferritin, lumazine synthase, and encapsulins, can be repurposed and

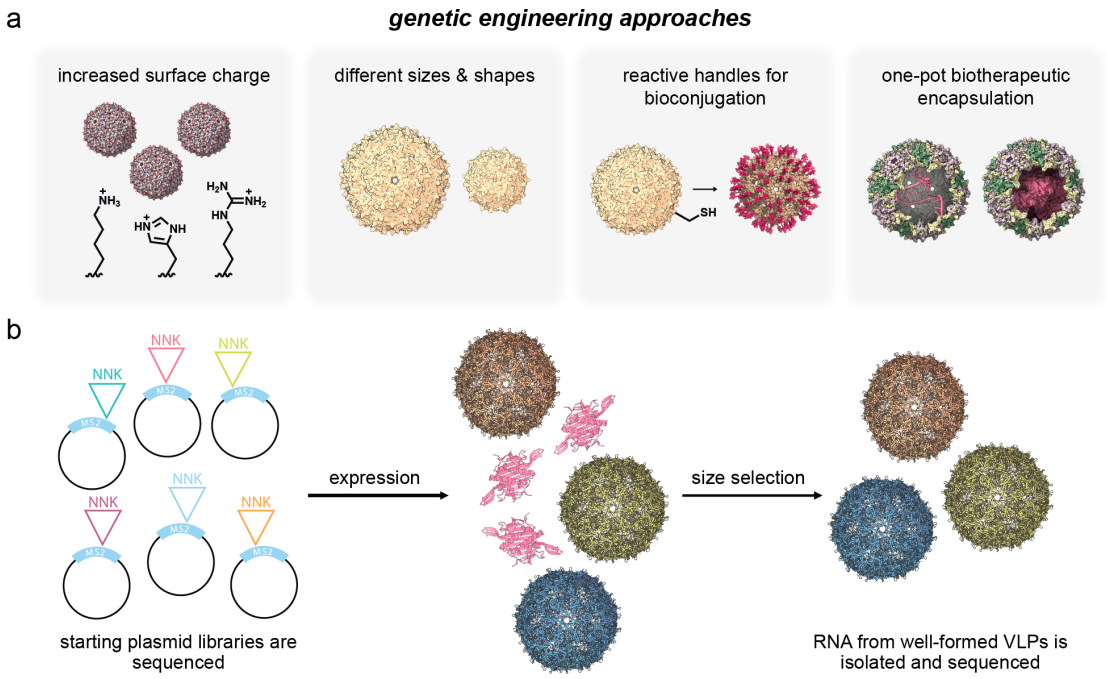


Figure 1.4: Genetic approaches for virus-like particle engineering. **(A)** Genetic engineering approaches can be used to identify VLPs with improved properties such as those shown left to right: increased surface charge, different sizes and shapes, reactive handles for bioconjugation, and one-pot biotherapeutic encapsultion. **(B)** Systematic Mutagenesis and Assembled Particle Selection (SyMAPS) has been used to identify MS2 and Qβ variants with improved properties after functional selection for particle assembly, size, stability, and other properties.

re-engineered as virus-like particles to encapsulate genetic material and other cargo [63–66]. Using a combination of rational design and subsequent rounds of directed evolution, a previously evolved 60-subunit nucleocapsid derived from *Aquifex aeolicus* lumazine synthase (AaLS) was redesigned to encapsulate its own mRNA transcripts that contain an RNA-packaging stem loop sequence [67, 68]. Protein nanocages have also been engineered to concurrently encapsulate protein and RNA, enabling the construction of more complex virus-like architectures with expanded therapeutic potential [69].

Icosahedral protein structures can be designed *de novo*, creating hyperstable protein shells with custom-made properties for any imaginable application or targeted delivery approach. Computational protein design has been used to create various protein shells and nanoparticles with virus-like architectures. The Baker lab has created icosahedral protein nanocages that self-assemble into trimeric building blocks (similar to the viral functional unit) and are highly stable in extreme conditions such as 6.7 M guanidine hydrochloride and 80 °C [70]. The King and Baker labs have also designed *de novo* protein nanoparticles with custom functions such as pH-responsive antibody nanoparticles, multi-component protein nanomaterials, RNA-

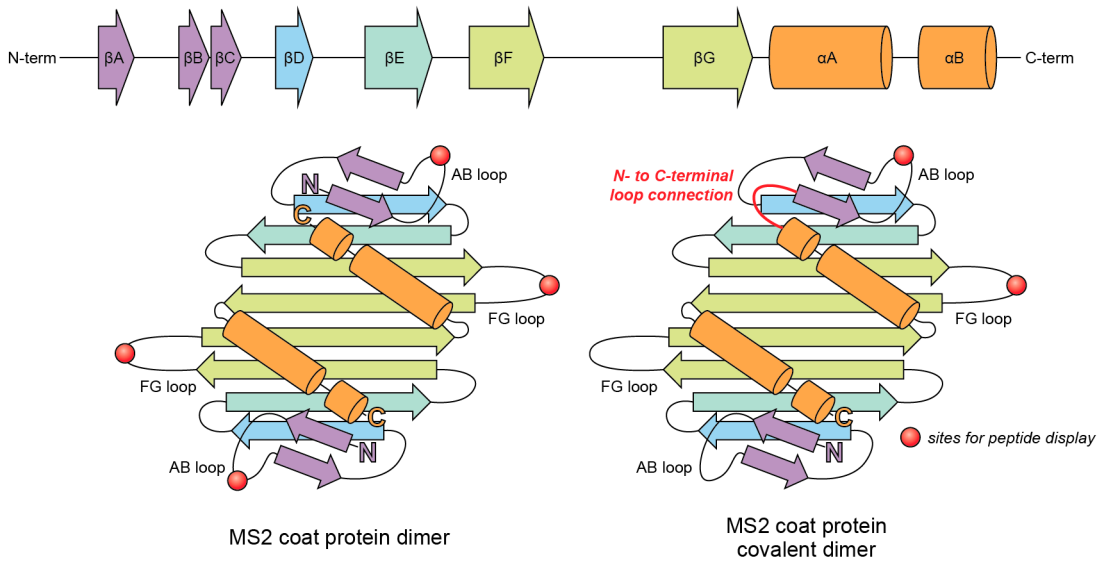


Figure 1.5: Peptide display on virus-like particles. VLPs from the *Leviviridae* family (MS2, Qβ, PP7) have been engineered for peptide display. Peptide sequences can be inserted into the AB or FG loop regions of the coat protein sequence (red spheres show insertion sites). Covalent coat protein dimers that fuse the N- to C-terminus of two dimers provide a platform for peptide display with improved VLP stability and the ability to display two or more different peptides per dimer.

packaging nucleocapsids, and pseudosymmetric nanoparticles with up to 960 subunits [71–74].

1.5 Engineered virus-like particles with new functions for drug delivery

Natural viruses have evolved to deliver their genetic payload to target cells and continue the viral replication cycle. The structural components of viruses can be further engineered as non-infectious VLPs for a wide variety of biomedical applications such as vaccines, diagnostic agents, and therapeutic small-molecule, protein, and nucleic acid delivery vehicles. VLP engineering strategies are crucial to enable the targeted delivery of unnatural payloads inside of VLPs, as most viruses in their natural state have evolved to deliver a small set of proteins and their genome and can only infect a specific cell type or organism. Various genetic, chemical, and enzymatic modification strategies can be employed to create tailored VLPs that carry drug payloads and reach specific cells or tissues with targeting groups appended to the VLP exterior. In many cases, VLPs must also be developed to release their cargo at the right time inside their target cell. Each available VLP platform has advantages and disadvantages, such as ease of production, ideal therapeutic payloads, additional engineering

or targeting requirements to facilitate cellular uptake, and *in vivo* biodistribution profiles. Thus far, these engineering strategies have facilitated the development of VLPs that have significant therapeutic potential.

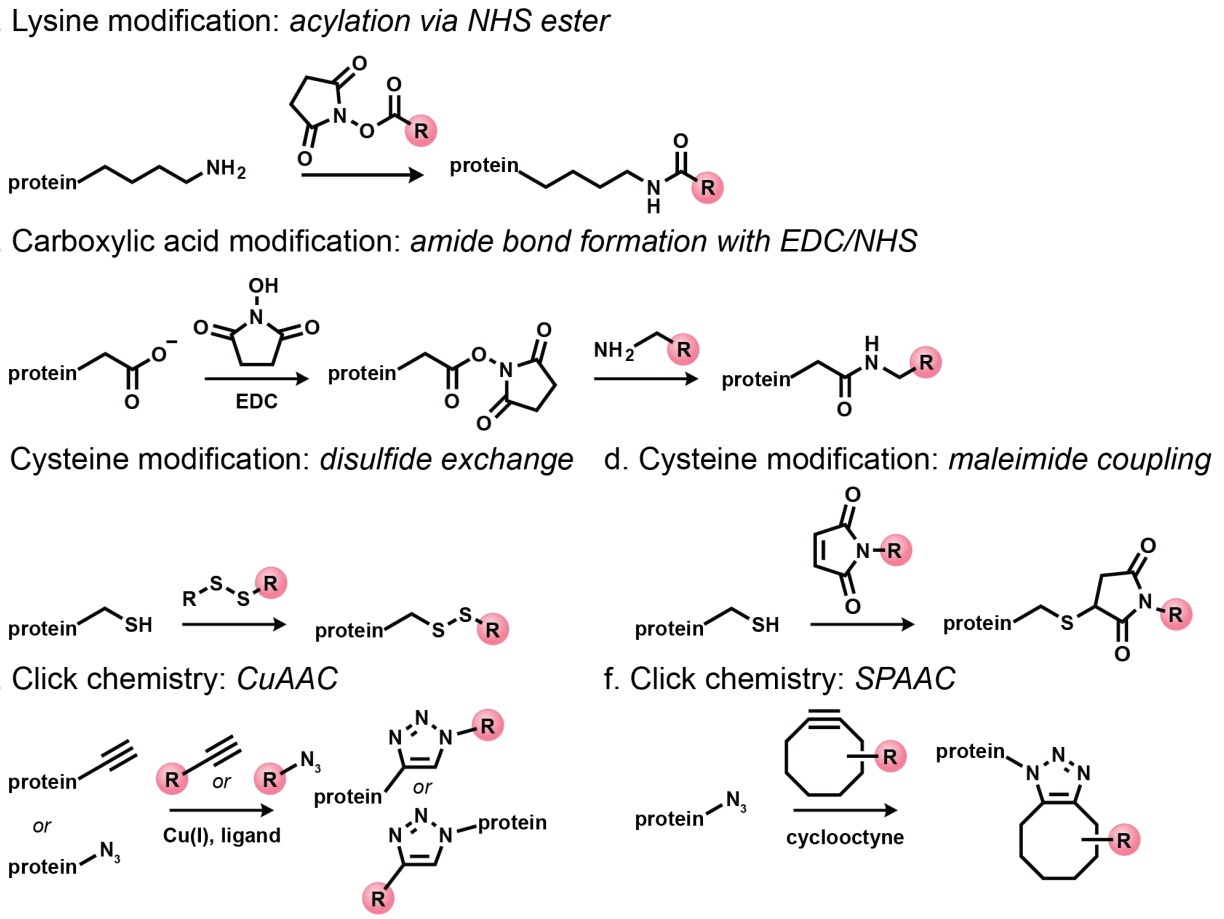


Figure 1.6: Commonly used reactions for the chemical modification of virus-like particles [75, 76]. **(A)** Lysine residues can be acylated with NHS-esters. **(B)** Glutamate, aspartate, and the C-terminus can undergo amide bond formation with primary amines following activation by EDC/NHS. **(C)** Cysteines can be modified via disulfide exchange. **(D)** Cysteines can also undergo maleimide couplings. **(E)** Copper-catalyzed azide-alkyne cycloaddition (CuAAC) can be used to functionalize unnatural azide and alkyne residues. **(F)** Strain-promoted azide-alkyne cycloaddition (SPAAC) can be used to modify unnatural azide residues.

Chemical and enzymatic modification of virus-like particles

Many bioconjugation reactions are used to modify both the interior and exterior of VLP capsids. Most of these reactions display selectivity for a specific amino acid type, and modifications can target native amino acids and sequence-engineered or bioorthogonal amino acids installed on a VLP. In the case of VLPs, chemical modification of a symmetric as-

sembly enables the construction of capsids that have been modified with targeting groups or drugs on every single capsid monomer, allowing for the dense, multivalent display of antigens or targeting groups and the ability to deliver many copies of a single drug molecule. If multiple reactive residues per monomer are present, such as with lysine, tyrosine, and carboxylic acids, heterogeneous mixtures of products can be produced, which can lead to variations in sample activity [77]. Site-specific modification is usually achieved via engineered cysteines, specific N-terminal residue combinations, or unnatural functional groups such as alkynes, azides, or anilines (Figure 1.6) [75]. Sometimes, chemical reactivity can be improved further via library-based selection methods. In the case of MS2 VLPs, N-terminal modification is incompatible with the native N-terminus due to its sterically hindered location. Constructing a library of MS2 capsids with three-amino acid N-terminal extensions with a terminal proline enabled the identification of variants modified to high yields by an oxidative coupling reaction [53]. Enzymatic methods can also be used to attach cargo to VLPs (Figure 1.7). Oxidative coupling reactions, enabled by small molecules or tyrosinase enzymes, allow for the conjugation of small molecule, peptide, and protein cargo to VLPs [78–82]. Sortase and SpyCatcher/SpyTag systems have also been used to create site-specific isopeptide bonds between VLPs and protein cargo on AP205, HBV, MS2, P22, and AAV capsids [41, 83–89].

Virus-like particles as vaccines

Although some VLP-based vaccines are already clinically approved, many are still in early discovery or clinical development. All currently approved VLP-based vaccines use systems that recombinantly express native viral proteins; new technologies are being developed to expand the repertoire of possible vaccine antigens. VLPs provide an especially promising platform for the antigenic display of viral epitopes for increased immune response. Immunogenic epitopes can be displayed on the surface of VLPs using chemical or genetic fusion methods. Non-enveloped virus-like particles have been engineered to display peptides on their capsid protein surface through loop insertions or N- or C-terminal genetic fusions. The terminal extension of bacteriophage coat protein sequences is quite common, as it is the basis for phage display platforms. In phage display, the N-terminus of minor and major coat proteins pIII or pVIII of filamentous phage M13 are used to display up to 2700 copies of a peptide or protein on the surface of a phage capsid, allowing for the selection of peptide and antibody fragments with specific binding properties for biomedical applications [91]. Insertion of peptide fragments into VLP loops is more limited due to the high potential of disrupting self-assembly. However, loop insertion has been successfully used to display peptide and scFv fragments on the surface of a variety of bacteriophage and plant virus scaffolds, including cowpea mosaic virus, flock house virus, PP7, and MS2 [55, 58–60, 92–96]. In the case of MS2, short peptide insertions can be displayed at its FG loop, while the use of a covalentl fused single-dimer chain is required for the insertion of peptides into the AB loop into one of the two fused monomers [51, 95]. The inability of many VLPs to tolerate the insertion of complex antigen targets is a significant drawback of using naturally occurring VLP scaffolds.

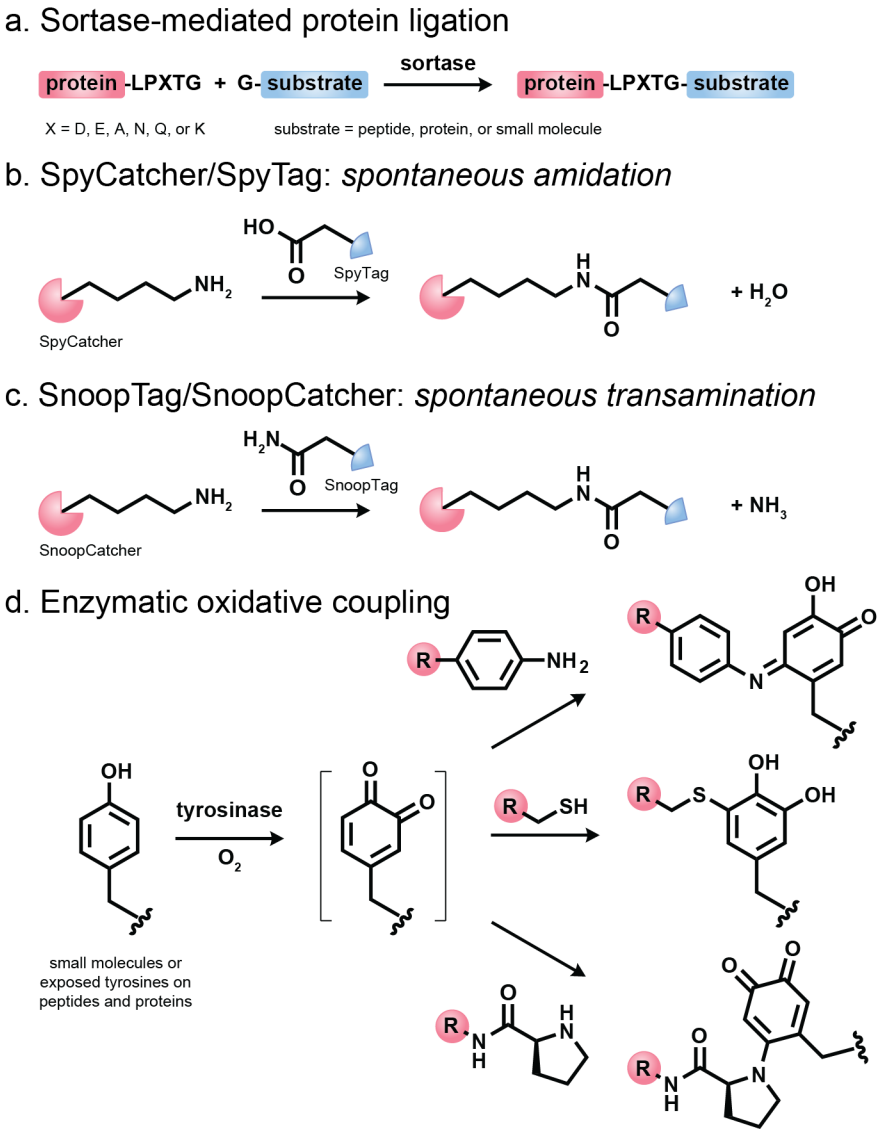


Figure 1.7: Enzymatic modification of virus-like particles [80, 87, 88, 90]. **(A)** Sortase-mediated protein ligation allows for the attachment of proteins and peptides with N- and C-terminal glycine and LPXTG tags, respectively. **(B)** The SpyCatcher/SpyTag split protein system allows for spontaneous amidation to occur between the SpyCatcher protein and proteins or peptides with the SpyTag sequence. **(C)** The SnoopCatcher/SnoopTag split protein system allows for spontaneous transamination to occur between the SnoopCatcher protein and protein or peptides with the SnoopTag sequence. **(D)** Phenols are oxidized by tyrosinase to give *o*-quinone intermediates that can react with a variety of nucleophiles on peptides, proteins, and small molecules.

Structure-guided computational protein design can also be used to create protein nanoparticle vaccines that display complex immunogens in a multivalent assembly [97]. Rather than relying on a fixed scaffold structure as a platform for antigen display, the ability to engineer vaccine candidates comprised of *de novo* self-assembling proteins allows for the creation of vaccine candidates that can display complex, heterologous antigens with increased complexity. This platform has been used to develop protein nanoparticle vaccine candidates for RSV and SARS-CoV-2, among other respiratory viruses [97–99]. Icosavax has developed several VLP-based vaccines using this method that are in various stages of clinical development, and was acquired by AstraZeneca for $1.1 billion in 2023.

Covalent modification strategies can also be used to attach antigens to both the inside and outside of VLPs for vaccine and immunotherapy applications. Chemoenzymatic approaches such as sortase, SpyTag:SpyCatcher, SnoopTag:SnoopCatcher, and split-intein domains allow for the site-specific, covalent attachment of proteins and peptides to the exterior of VLPs, and have been used with P22, HPV, AAV, and AP205 scaffolds [83, 85–89]. Other sites-specific modification strategies rely on the installation of reactive natural (cysteine, tyrosine, N-terminus) or unnatural (azide, alkyne, aniline) amino acids functional groups on the VLP exterior or interior surfaces [75, 100].

Non-site-specific modification strategies often use natural amino acids such as surface lysine to attach antigens to the VLP surface. Heterobifunctional linkers such as SPMH (succinimidyl 6-((beta-maleimidopropionamido)hexanoate)) and DBCO (dibenzocyclooctyne) NHS esters have been used to functionalize VLP surface lysines and attach synthetic peptides with C-terminal cysteines or azides [101]. Recently, glycan-decorated VLP vaccines have been developed for cancer immunotherapy. Surface lysines on bacteriophage PP7-derived VLPs were functionalized with a click-compatible azide handle and tumor peptide antigens and targeting mannose glycans were appended using copper-catalyzed azide-alkyne cycloaddition (CuAAC), creating dually functionalized PP7 VLPs with encapsulated ssRNAs from bacterial recombinant expression for TLR7 agonism and immune activation [102, 103].

Virus-like particles for small-molecule drug delivery

While the natural cargo of VLPs is nucleic acids, genome-free capsids can be produced and loaded with or assembled around a variety of synthetic small-molecule cargo for drug delivery applications (Figure 1.8). VLPs can be disassembled *in vitro* by changing conditions such as buffer pH and ionic strength, releasing the viral genome, and producing a solution of dimers or monomers ready for reassembly [104]. For example, CCMV will disassemble and release its RNA at physiological pH or high ionic strength and reassemble at low pH or low ionic strength. In contrast, MS2 capsids will disassemble and precipitate encapsulated nucleic acids at high concentrations of acetic acid and can reassemble in the presence of osmolytes, negatively charged cargo, or DNA/RNA-packaging signal oligomers [105–107]. These *in vitro* reassembly techniques have been used to encapsulate a wide variety of cargo without the need for covalent modification, such as quantum dots, small-molecule drugs, proteins, and oligonucleotides. Successful encapsulation and reassembly can depend on factors such as

cargo size and charge, leading to favorable electrostatic or affinity-based interactions during the assembly process. Depending on the VLP, bioconjugation strategies can be used to covalently attach small molecules to the exterior and interior of the capsid. Reassembled and covalently-modified MS2 VLPs have been used to deliver apoptosis-inducing cancer therapeutics such as porphyrins and Tl^{+} [100, 108]. However, the therapeutic effects in these studies were modest and could benefit from further capsid engineering or targeting strategies to improve cellular uptake and *in vivo* biodistribution.

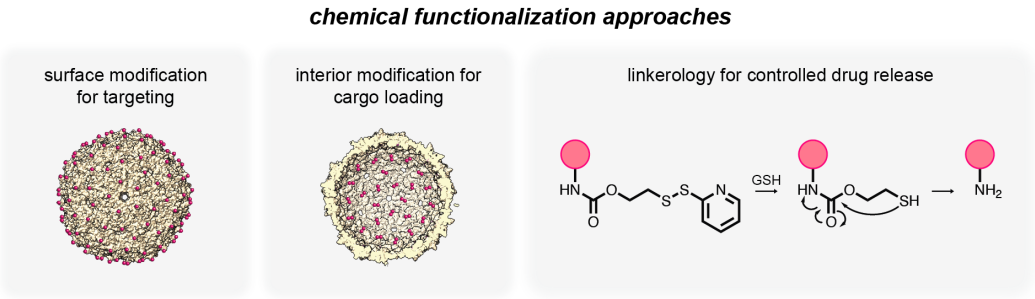


Figure 1.8: Chemical functionalization of virus-like particles for drug delivery. Chemical and enzymatic modification strategies can be used to add targeting groups to VLP surfaces and load drug molecules into VLP interiors. Linker chemistries can be used to facilitate drug release upon intracellular delivery.

Virus-like particles for diagnostic and imaging applications

Many diagnostic and medical imaging technologies rely on delivering contrast agents *in vivo* with optimal signal-to-noise ratios and minimal side effects. VLPs are promising vehicles for the delivery of imaging agents due to their ability to be modified to target specific cells or tissues, carry a wide range of cargo, and possess short circulation time and biodegradability when compared with synthetic nanoparticles [104]. VLPs labelled with fluorophores or contrast agents can be used in *in vitro* and *in vivo* studies to measure cellular uptake and biodistribution and allow for the targeted imaging of diseased states. In one example, MS2 capsids radiolabelled with ^{64}Cu isotopes displaying anti-EGFR antibodies were able to target EGFR+ tumors and were imaged with positron emission tomography–computed tomography (PET/CT) *in vivo* and *ex vivo* [109]. Many other bacteriophage (MS2) and plant virus-based (CCMV, TMV, PhMV) VLPs have also been used for molecular imaging studies for cancer imaging, fibrin imaging, and the stratification of atherosclerotic plaques [104, 110–113].

Virus-like particles for therapeutic protein delivery

Both enveloped and non-enveloped virus-like particles have been used for protein cargo encapsulation. While many of these systems focus on protein delivery for therapeutic applications, they are also useful in biocatalysis. As viruses possess native machinery for genome and non-structural protein encapsulation, these approaches can be used to develop strategies for encapsulating foreign protein cargo in VLPs. Two common approaches are the use of (1) native biomolecular interactions or (2) capsid protein fusions. The size and type of cargo that can be encapsulated in a specific VLP depends on capsid size, assembly mechanisms, and potential protein-protein interactions between the capsid interior and encapsulated cargo. Non-covalent interactions can be taken advantage of for protein encapsulation, including electrostatic-, peptide-protein-, and peptide-nucleic acid-mediated encapsulation of target cargo proteins [114]. Encapsulation by electrostatic interactions relies on favorable charge-charge interactions between the cargo protein and capsid interior, which is often positively charged for genome encapsulation. This has been taken advantage of widely in bacteriophage MS2, Qβ, and PP7 systems, where protein cargo that is naturally anionic, engineered with negatively charged tags, or conjugated to anionic nucleic acid tags can readily be encapsulated [105, 115–117]. This approach provides a flexible platform for the loading of many different types of protein cargo. However, loading efficiencies tend to be lower than platforms that rely on specific affinity or covalent attachment [114].

The interactions between the coat proteins and scaffold proteins (SP) of many bacteriophage VLPs are a native protein-protein interaction that can be re-engineered for foreign protein encapsulation. This approach has been successful for the encapsulation of fluorescent proteins and enzymes in T4 and P22 VLPs, where up to 330 copies of a truncated SP-protein cargo fusion protein can be encapsulated inside of a single P22 capsid [118, 119]. Sequence-specific protein-RNA interactions can also be utilized for protein encapsulation in VLPs. RNA packaging signals (PS) are commonly used to initiate encapsulation of the viral genome. These short RNA hairpins can also be chemically conjugated to protein cargo as an encapsulation strategy. This strategy has been applied to MS2, using the 19-nt RNA or DNA stem loop *TR* to encapsulate proteins, siRNA, and other molecules of interest inside of MS2 VLPs [105, 107, 120]. A similar interaction between an RNA hairpin and the Qβ coat protein has been used for protein encapsulation as well, using a bifunctional packaging hairpin-RNA aptamer molecule to encapsulate protein cargo of interest in an *in vivo* co-expression system [121, 122]. When fluorescent proteins with an N-terminal Rev tag were coexpressed with Qβ coat protein and the a-Rev RNA aptamer, VLPs encapsulating the tagged fluorescent protein were able to highly stabilize the encapsulated proteins towards heat, chaotropes, and proteolysis compared to the non-encapsulated analogs [123]. In both cases, MS2 and Qβ VLPs could encapsulate between 3 to 5 and 2 to 18 copies of a protein per capsid, representing a much lower protein delivery payload compared to other VLPs.

Covalent attachment strategies rely on genetic fusion or post-translational conjugation of protein cargo to capsid proteins. The genetic fusion method specifically allows for *in vivo* cargo encapsulation during recombinant expression of VLPs. This method is more common

for protein encapsulation in enveloped VLPs, whose lack of structural symmetry allows for the flexible incorporation of cargo compared to non-enveloped icosahedral viruses [15]. However, protein encapsulation via genetic fusion has been achieved in some non-enveloped VLPs, allowing for the encapsulation of 120 GFP molecules in bluetongue virus (BTV) and rotavirus VLPs for cellular imaging and protein delivery [124, 125]. In the case of enveloped VLPs, lentivirus-based VLPs have been engineered for protein encapsulation for the delivery of various therapeutic proteins [126, 127]. To promote the packaging of Cas9 protein in HIV-1 capsids, Cas9 was fused to the C-terminus of the Gag polypeptide and packaged during VLP production, allowing for the targeted *ex vivo* and *in vivo* transfection and editing of human T cells without electroporation [12, 13]. Engineered VLPs based on Friend murine leukemia virus (FMLV) have been used for the delivery of adenine base editors by genetic fusion of the base editor protein to the C-terminus of the FMLV Gag polyprotein, enabling *in vivo* base editing of 63% in the liver and partially restoring visual function in blind mice [11, 14].

Virus-like particles for therapeutic nucleic acid delivery

The delivery and release of nucleic acids from virus-like particles is a promising method to increase the efficacy of nucleic acid therapeutics such as small-interfering RNAs (siRNA), mRNA vaccines, and gene therapies. Many mammalian viruses have been used for nucleic acid delivery, but there are concerns regarding immunogenicity and genome integration when using these systems. Though less explored, virus-like particles derived from mammalian, plant, and bacteriophage viruses offer an alternative method to develop new engineered systems for nucleic acid delivery. Adeno-associated virus (AAV) vectors are currently the leading platform for gene delivery, with many AAV-based therapeutics in clinical development. There are currently seven FDA-approved viral gene therapies that use adenovirus, AAV, or herpes simplex virus to treat several genetic conditions, including bladder cancer, muscular atrophy, hemophilia, and blindness (Table 1.2) [128].

Name	Company	Year	Disease	Vector
Adstiladrin®	Ferring Pharma A/S	2022	bladder cancer	adenovirus
Elevidys®	Sarepta Therapeutics	2023	Duchenne muscular dystrophy	AAV
Hemgenix®	CSL Behring	2022	hemophilia B	AAV
Luxturna®	Spark Therapeutics	2017	genetic blindness	AAV
Zolgensma®	AveXis/Novartis	2019	spinal muscular atrophy	AAV
Roctavian®	BioMarin	2023	hemophilia A	AAV
Vyjuvek®	Krystal Biotech	2023	wound treatment	topical HSV-1

Table 1.2: A list of current clinically approved viral gene therapies [128].

AAV is a single-stranded DNA (ssDNA) virus that is endocytosed into host cells after recognition by glycosylated cell surface receptors [129]. In the low pH environment of the endosome, the VP1/VP2 capsid proteins undergo a structural change that mediates endosomal escape, initiating viral transport to the nucleus for genome uncoating [129]. Inverted termi-

nal repeats (ITRs) in the AAV genome allow for recombination to form circular genomes that can persist in the nucleus, and can also undergo integration into the host genome, albeit at very low frequencies [129]. AAV capsid engineering is a major pursuit for developing capsids with specific properties and characteristics. New capsids can be developed by natural discovery, rational design, directed evolution, and *in silico* methods. These methods can yield AAV capsids with increased tissue or cell-type specificities for targeted gene delivery, which are currently most successful for delivery to the liver, muscle, and central nervous system (CNS). Key challenges of using AAVs for gene therapy include vector manufacturing costs and immunological barriers.

The use of non-human viruses and VLPs in humans is a potentially safer alternative to mammalian viruses for gene therapy, as they cannot replicate, infect, or integrate into host cell genomes [130]. It has been shown that plant viruses and VLPs can be administered to mice at doses of up to 100 mg per kilogram bodyweight without toxicity effects [131, 132]. Immunogenicity still presents a problem when using plant- and bacteriophage-derived systems, as they are moderately immunogenic [133]. This can be useful for certain applications such as immunotherapy but can also be avoided by chemical surface modification strategies such as PEGylation [134, 135]. Cowpea chlorotic mosaic virus (CCMV) has been used to deliver heterologous RNAs to mammalian cells with Lipofectamine 2000 to enable cellular uptake, showing that plant viruses can release functional RNAs after cellular uptake [136]. Tobacco mosaic virus (TMV) has been used to create pseudoviruses that encapsulate RNA from other viruses *in vitro* for gene transfection in mammalian cell lines [137–139]. Bacteriophages such as MS2, PP7, and Qβ have been studied as systems to deliver various RNA-based therapeutics. Using *in vitro* encapsulation and reassembly methods, MS2 VLPs with targeting peptides were able to deliver up to 85 siRNA molecules per capsid and induce growth arrest and apoptosis of targeted cancer cell lines [107]. MS2, PP7, and Qβ systems have also been engineered for the *in vivo* coexpression and encapsulation of shRNA, miRNA, and mRNA in *E. coli* and *S. cerevisiae* [140–145]. Various VLPs have also been developed for DNA delivery applications, using the capsid proteins of DNA viruses such as Polyomavirus and hepatitis B to successfully deliver GFP plasmids to target cells [146, 147].

Engineered virus-like particles for cargo release

One drawback of using non-mammalian viruses and VLPs for therapeutic protein and nucleic acid delivery is that they often must be further engineered to release their cargo once cellular internalization has occurred. It is difficult to determine the mechanism of capsid disassembly, endosomal escape, and cargo delivery inside target cells. Capsids can be engineered to have increased or decreased assembly stability under diverse conditions to facilitate the encapsulation and release of cargo at the desired location inside of a cell. Work has been done to chemically modify the interior of some capsids to stabilize the VLP and its encapsulated cargo for drug delivery. CCMV capsid proteins were loaded with lysozyme via Sortase A-mediated N-terminal functionalization, creating capsids with His_6 tags that can be stabilized in the presence of Ni^{2+} ions [148]. Cysteine modification-based nonreversible

and reversible crosslinking strategies have also been employed to stabilize CCMV VLPs, the latter of which is especially useful for drug delivery to promote capsid disassembly in the reducing environment of the cell interior [149, 150]. Fitness landscaping studies have enabled the identification of acid-sensitive MS2 capsids that disassemble at pH 5.5, which would be useful for releasing cargo in the endosomal-lysosomal uptake pathway [49, 151].

1.6 Conclusion

In this review, the use of virus-like particles as platforms for the study of self-assembly and the development of vaccines and therapeutic delivery vehicles is discussed in depth. VLP structure and function must be considered when choosing a system to develop for one's intended application, as certain features are naturally present, and others must be engineered depending on the VLP. Essential features to consider for drug delivery include VLP production, cell-specific targeting, cellular uptake efficiency, and cargo encapsulation and release. Through recombinant expression, VLPs can easily be produced recombinantly in mammalian, plant, bacterial, and yeast systems. Protein engineering techniques can be used to create VLPs with specific sizes, shapes, surface charges, stabilities, and other tailored features. The sequence-defined nature of VLPs allows for site-specific genetic or chemical modification by taking advantage of genetic fusions and reactive amino acid residues on VLP capsid surfaces or interiors. These strategies can be used to load drugs and append exterior targeting groups to increase specificity for cell- or tissue-specific delivery applications. Methods to load cargo via non-covalent interactions can be developed using *in vitro* or *in vivo* encapsulation strategies for protein and nucleic acid cargo. With continued efforts in VLP engineering, protein-based nanoparticles provide a promising platform for developing delivery vehicles that can be translated to the clinic.

Chapter 2

Fitness landscape-guided engineering of locally supercharged virus-like particles with enhanced cell uptake properties

2.1 Abstract

Protein-based nanoparticles are useful models for the study of self-assembly and attractive candidates for drug delivery. Virus-like particles (VLPs) are especially promising platforms for expanding the repertoire of therapeutics that can be delivered effectively, as they can deliver many copies of a molecule per particle for each delivery event. However, their use is often limited due to poor uptake of VLPs into mammalian cells. In this study, we use the fitness landscape of the bacteriophage MS2 VLP as a guide to engineer capsid variants with positively charged surface residues to enhance their uptake into mammalian cells. By combining mutations with positive fitness scores that were likely to produce assembled capsids, we identified two key double mutants with internalization efficiencies as much as 67-fold higher than that of wtMS2. Internalization of these variants with positively charged surface residues depends on interactions with cell surface sulfated proteoglycans, and yet they are biophysically similar to wtMS2 with low cytotoxicity and an overall negative charge. Additionally, the best-performing engineered MS2 capsids can deliver a potent anticancer small molecule therapeutic with efficacy levels similar to antibody-drug conjugates. Through this work, we were able to establish fitness landscape-based engineering as a successful method for designing VLPs with improved cell penetration. These findings suggest that VLPs with positive surface charge could be useful in improving the delivery of small molecule- and nucleic acid-based therapeutics.[1]

[1]Portions of this chapter are reprinted with permission from Pistono, P. E.; Huang, P.; Brauer, D. D.; Francis, M. B. Fitness Landscape-Guided Engineering of Locally Supercharged Virus-like Particles with Enhanced Cell Uptake Properties. *ACS Chemical Biology* 2022. https://doi.org/10.1021/acschembio.2c00318; Copyright 2022 American Chemical Society, licensed under CC-BY 4.0 [152].

2.2 Introduction

Engineered nanoparticles are promising materials for use in drug delivery, with the potential to enhance cellular uptake, improve cargo stability and solubility, and allow cell-specific targeting [153]. The most well-characterized nanomaterials for drug delivery include lipid-based and polymeric nanoparticles (NPs), with lipid-based NPs being the most common class of FDA-approved nanomedicines [154]. Here, we discuss the use of a virus-like particle (VLP) as a potential drug delivery vehicle. Unlike polymer- and lipid-based NPs, VLPs can be inexpensively produced by recombinant expression, are homogenous in particle size, and are easily degradable in the body [155, 156]. Protein-based materials can be genetically engineered with new functionalities and site-specific modification can be achieved through insertion of specific natural or non-canonical amino acids into the protein sequence [50, 74, 157]. Although protein-based nanoparticles possess many attractive features, their exploration has thus far been limited due to poor cellular uptake, with the exception of the use of viral vectors for gene therapy and vaccines [158].

The utility of engineered, sequence-defined protein nanoparticles with desirable properties would benefit from strategies to fine tune their surface charge, a key property that dictates their stability and interactions with biological components. In monomeric form, it is well established that cationic peptides and proteins can enter and deliver cargo to mammalian cells, ranging from cell-penetrating peptides such as HIV-Tat to mini cationic proteins and full-sized supercharged proteins [159–162]. Unlike the prior examples, the mutational effects of installing cationic residues on VLPs would be amplified by the regular periodicity of their nanostructure. We hypothesized that local supercharging on nanoscale particles could result in cellular uptake enhancement with decreased cytotoxicity when compared with commercially available cationic liposomes, thus avoiding a major bottleneck in the application of these nanoparticles for drug and biotherapeutic delivery [163]. Additionally, expanding the understanding of VLP design rules by altering particle charge could bestow the ability to tune other properties, such as thermostability and pH sensitivity.

Bacteriophage MS2 is a well-studied VLP that forms 27 nm capsids with 2 nm pores and a hollow interior cavity that can be used for cargo loading [156]. MS2 can be recombinantly expressed as a non-infectious variant at high yields. Importantly, the capsids can encapsulate segments of mRNA during expression and self-assembly, providing a direct genotype-to-phenotype link that can be used for fitness landscaping [164]. Recently, our lab developed a method known as SyMAPS, or Systematic Mutation and Assembled Particle Selection, that was used to characterize the assembly properties of all single amino acid variants of MS2-based VLPs [151]. Using this method, subsequent fitness landscaping studies of MS2 have identified assembly competent, thermostable, acid sensitive, and chemically modifiable variants [49, 51, 52, 151].

One property that these fitness landscaping experiments have not selected for is mammalian cell internalization. Previous studies reporting MS2 capsids as delivery vehicles have shown the benefit of targeting groups, such as transferrin, peptides, aptamers, and antibodies that are conjugated to the exterior surfaces of the capsids. Although these strategies are

important for enhancing cell binding, some of these studies also noted that MS2 internalization levels were lower than that of other delivery vehicles such as lipid-based nanoparticles [81, 107, 109, 165]. The usefulness of MS2 as a drug delivery vehicle would be expanded immensely by improving its inherent cellular uptake efficiency. With this in mind, we sought to use the single amino acid fitness landscape of MS2 as a guide to design variants that are capable of carrying internal cargo into mammalian cells. We envisioned that we could capitalize on the dense, symmetrical quaternary assembly of MS2 to generate supercharged patches along the capsid surface without significantly shifting the global charge of the particle. This engineering approach would not be possible with other nanoparticle systems whose structures are not sequence-defined.

Here, we use fitness landscape-guided engineering to identify well-assembled MS2 variants with positively charged amino acids in specific positions to increase mammalian cell uptake. We identified two key double mutants that produce capsids with localized pockets of positive charge and internalization efficiencies up to 67-fold higher than that of wtMS2. Current evidence suggests that these MS2 variants with positively charged surface residues enter cells through an energy-dependent endocytic pathway that is mediated by binding to sulfated proteoglycans on the cell surface. These engineered variants are biophysically similar to wtMS2, including its negative overall charge, and are non-toxic to cells. We also found that these variants can deliver monomethyl auristatin E (MMAE), a potent anticancer therapeutic, to glioblastoma cells with efficacy comparable to antibody-drug conjugates. These findings indicate that virus-like particles with strategically placed positive surface charges could overcome key limitations in the delivery of a wide range of small molecule- and nucleic acid-based therapeutics.

2.3 Results and Discussion

Design and characterization of MS2 variants with positively charged surface residues

MS2-based virus-like particles (VLPs) consist of 180 identical copies of the coat protein (CP) in the form of 90 dimers, forming a $T = 3$ icosahedron with several unique interfaces [164]. Assembly of MS2 VLPs is triggered by a conformational switch from the symmetric C/C dimer to the asymmetric A/B dimer upon binding of genetic material such as RNA [40, 166]. Binding of genetic material also provides a direct genotype-to-phenotype link for fitness landscaping, for which our laboratories have developed a technique known as Systematic Mutagenesis and Assembled Particle Selection (SyMAPS) [151]. SyMAPS was used to characterize the assembly competency of all single amino acid variants of MS2, generating an apparent fitness landscape (AFL) for the capsid that assigns a quantitative apparent fitness score (AFS) for every variant at every position along the backbone of the MS2 CP. These data thus indicate all of the positions in which new lysine, arginine, and histidine residues can be introduced while still allowing capsid assembly, providing a useful

guide for engineering variants with increased cell internalization efficiency.

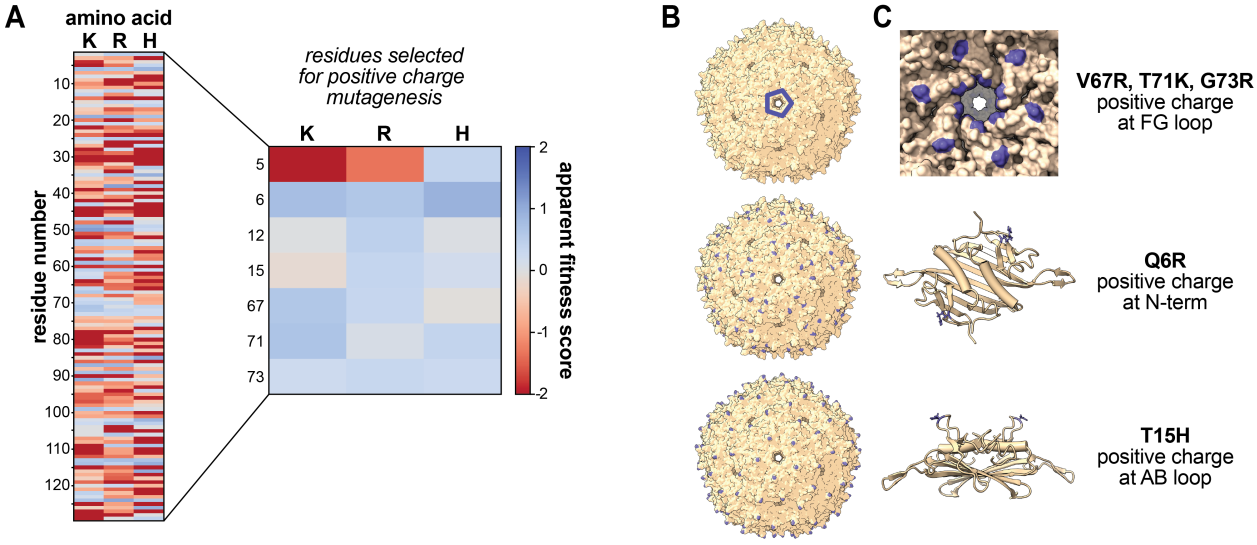


Figure 2.1: **(A)** Apparent fitness scores (AFS) for all Lys (K), Arg (R), and His (H) variants of the MS2 coat protein (MS2 CP). Positive (blue) AFS represent increased variant abundance, and negative (red) AFS correspond to decreased variant abundance. The scale is logarithmic, encompassing a 10,000-fold range of assembly propensity. **(B)** The locations of positive charge mutations (blue) mapped onto assembled MS2 CP (PDB ID = 2MS2). **(C)** The locations of positive charge mutations (blue) mapped onto the MS2 CP dimer structure (PDB ID = 2MS2).

MS2 Variant	AFS	Assembly	Thermostability
wild type	0.72	0.30	0.42
T71K	0.69	0.27	0.52
T71R	0.11	0.30	0.45
G73K	0.30	0.15	0.35
G73R	0.40	0.27	0.35
T71K/G73K	0.27	-0.13	-0.23
T71R/G73R	-0.21	-0.05	-0.40
T71K/G73R	0.37	-0.12	-0.29
T71R/G73K	-0.31	-0.1	-0.54

Table 2.1: Apparent fitness scores (AFS), assembly scores, and thermostability scores for wild-type MS2, and all Arg and Lys single and double mutants at positions 71 and 73 [49, 151].

Figure 2.1 shows the apparent fitness scores for lysine, arginine, and histidine at every position in the MS2 CP, which were used to select mutations with positive fitness scores that were likely to produce assembled capsids (Table 2.1). Histidine mutations were included to probe the possibility of making capsids that would become positively charged in acidic conditions such as the cancer extracellular microenvironment [167]. Mutations were selected

in three different surface-exposed regions of the capsid: the N-terminus (residues 1-6), the AB loop (residues 11-17), and the FG loop (residues 71-76). Mutations near the N-terminus and AB loop would result in an even distribution of positive charges over the capsid surface, while mutations in the FG loop would create localized pockets of positive charge at the capsid pores (Figure 2.1). Double and triple mutants were created at the FG loop to probe the effects of concentrated positive charge further. An initial panel of twelve MS2 CP variants containing an interior cysteine (N87C) for bioconjugation was designed and expressed. The assembly state of each variant was confirmed via size exclusion chromatography. Ten of the twelve designed variants were able to produce assembled capsids (Figure 2.2). The high success rate of capsid assembly among the twelve MS2 CP variants would not have been possible without fitness landscape-guided design. Out of the 45 surface-exposed residues on the capsid exterior, the assembly success rates for all lysine, arginine, and histidine mutants are 40%, 42%, and 51%, respectively, compared with an 83% assembly rate for capsid mutations chosen from the MS2 single amino acid fitness landscape [151]. The successfully assembled MS2 CP variant sequences were also compared to the residues selected for positive charge mutagenesis by Rosetta supercharge, a popular computational method for protein supercharging [162, 168–170]. Among the 45 surface-exposed residues on the capsid exterior, Rosetta supercharge correctly selected an R or K mutation that would result in assembled MS2 capsids with a 70-80% success rate depending on the input structure. Despite this high success rate, Rosetta did not predict two mutations that were selected in this work, N12K and G73R. The MS2 CP fitness landscape contains a wealth of information that cannot always be predicted computationally, such as how mutations will affect quaternary structure properties in the case of capsid assembly. Fitness landscaping can complement these powerful computational tools for protein engineering, serving to further probe the sequence-structure-function relationships underlying closely related proteins [171–173].

MS2 Variant	Unmodified Mass	+FITC Mass (Expected)	+FITC Mass (Observed)	+GSH Mass	%FITC Modification
N87C	13717	14144	14145	14024	87
T5H/N87C	13753	14180	14181	14060	83
Q6R/N87C	13746	14173	14173	14053	88
N12K/N87C	13717	14144	14145	14024	88
T15H/N87C	13753	14180	14181	14060	91
V67R/N87C	13775	14202	14202	14082	82
T71K/N87C	13745	14172	14172	14052	89
G73R/N87C	13816	14243	14244	14123	74
T71K/G73R/N87C	13843	14270	14270	14150	87
Triple*/N87C	13900	14327	14327	14207	81
T71R/N87C	13773	14200	14200	14080	84
G73K/N87C	13789	14216	14216	14096	87
T71R/G73R/N87C	13870	14297	14297	14177	90
T71K/G73K/N87C	13816	14243	14243	14123	77
T71R/G73K/N87C	13844	14271	14271	14151	72

Table 2.2: Masses (Da) of products obtained from MS2 CP variant fluorescein-maleimide labeling reactions determined by QTOF-ESI-MS. *Triple/N87C corresponds to MS2 CP variant V67R/T71K/G73R/N87C.

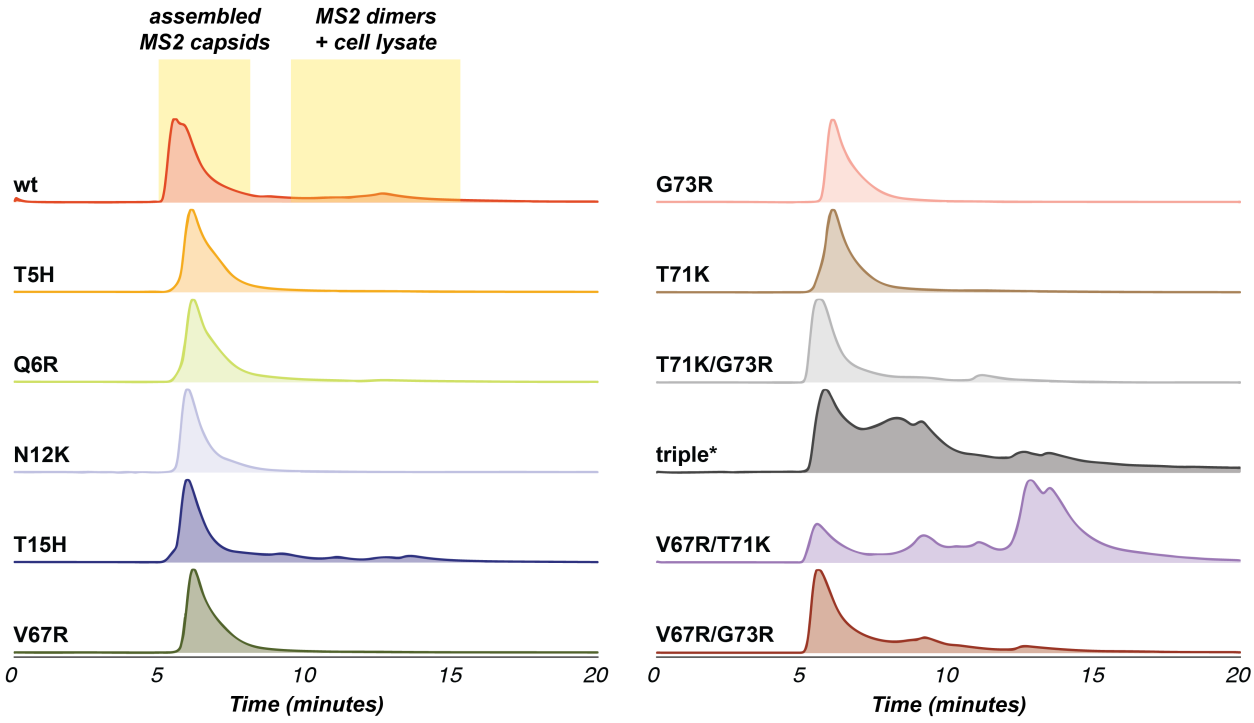


Figure 2.2: HPLC SEC traces of MS2 CP variants. Highlighted in yellow on the N87C trace are the expected elution times of assembled capsids (5-8 min) and dimers and cell lysate (10-15 min). *Triple corresponds to MS2 CP variant V67R/T71K/G73R.

Identification of MS2 variants with enhanced cellular uptake

To track their performance in cellular internalization studies, all assembled MS2 capsid variants were labeled with fluorescein-maleimide at the interior cysteine (N87C) and uptake into HeLa cells was screened via fluorescence microscopy and flow cytometry (Figures 2.4-2.5, Table 2.2). Cells were washed with heparin, which has been shown to remove positively charged surface-bound species, which we assumed could be useful for removing residual MS2 particles before imaging [161]. Of the ten variants analyzed, three variants (MS2 T71K, MS2 T71K/G73R, and MS2 V67R/T71K/G73R) exhibited significantly higher uptake compared to N87C (hereinafter referred to as wtMS2) capsids when visualized with fluorescence microscopy (Figure 2.6). The differences in overall uptake were quantified using flow cytometry, with the mean fluorescence intensity (MFI) of HeLa cells treated with MS2 T71K being 4.5-fold higher than that observed for cells treated with wtMS2. Interestingly, combining two single mutations that resulted in low or no internalization into a double mutant, MS2 T71K/G73R, produced an MFI 4-fold higher than cells treated with MS2 T71K and 18-fold higher than cells treated with wtMS2 (Figure 2.6, Table 2.3). Although we were expecting an additive effect with each additional positive charge, the MFI of cells treated with the triple mutant (V67R/T71K/G73R) was only 1.4-fold higher than that of the T71K/G73R double

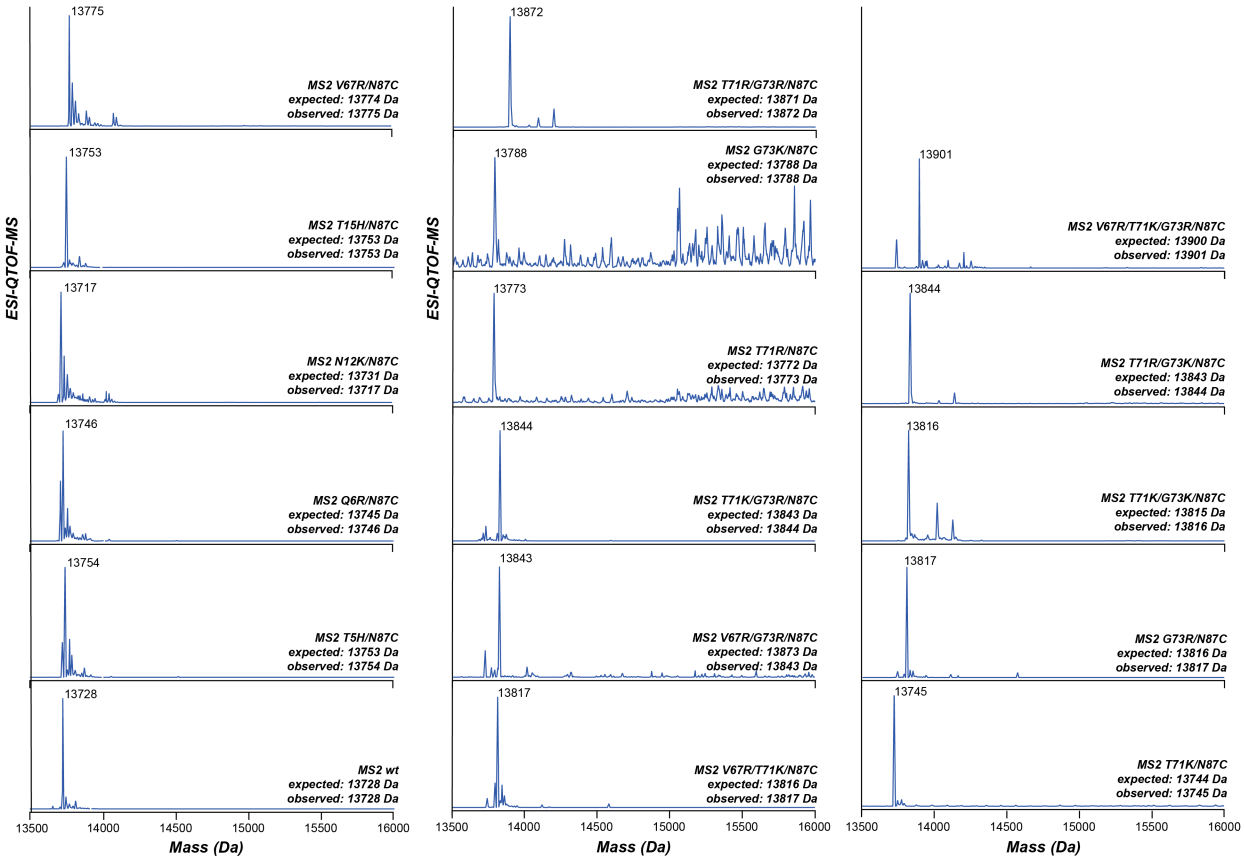


Figure 2.3: LC-MS analysis of MS2 CP variants.

mutant. Thus, the effects of additional positive surface charge on the internalization of MS2 capsids into mammalian cells were both position- and residue-dependent. Previous work on the effects of single mutations on VLP properties found that specific lysine-to-glutamine (K>Q) and lysine-to-glutamate (K>E) point mutants drastically altered Qβ binding to mammalian cells [175].

To explore the position and residue effects on uptake further, we created MS2 capsid variants representing every single and double mutant combination of arginine and lysine at backbone positions 71 and 73, located at the FG loop. This panel of eight MS2 CP variants was expressed, confirmed to assemble, and labeled with fluorescein for internalization experiments (Figures 2.4-2.5, Table 2.2). Imaging showed a visible divide in fluorescence between the single and double mutants, with all four single mutants showing low or no internalization (Figure 2.8). Interestingly, variants bearing a combination of arginine and lysine (MS2 T71K/G73R and MS2 T71R/G73K) exhibited significantly higher uptake than double mutants with the same charged residue (KK or RR). We further found that exchanging the position of arginine and lysine (T71K/G73R vs. T71R/G73K) resulted in a 3.8-fold enhancement in uptake, yielding a new best-performing variant with a 67-fold enhancement

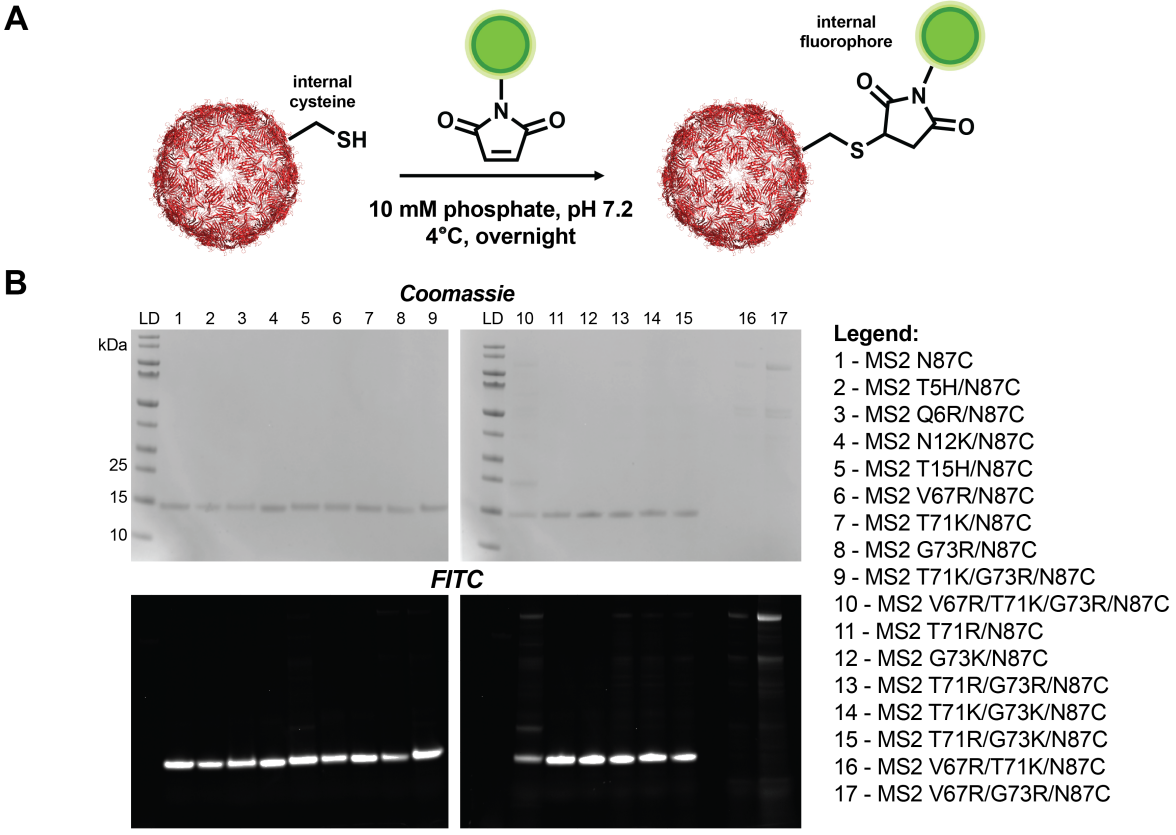


Figure 2.4: **(A)** Reaction scheme describing fluorophore-maleimide coupling to the internal cysteine N87C of each MS2 CP variant. **(B)** SDS-PAGE analysis illustrating the purity and normalization of each MS2-fluorescein conjugate before cell internalization assays. Each conjugate was normalized to 5 µM after fluorophore coupling and 15 µL was analyzed via SDS-PAGE.

in uptake relative to wtMS2 (Figure 2.8). Although a previous fitness landscape of double mutants in the FG loop (residues 71-76) region of MS2 provides information on the assembly and thermostability properties of these double mutants, their differences in cellular uptake efficiency could not have been predicted (Table 2.1) [49].

We compared the internalization of MS2 T71K/G73R into HeLa cells at a range of concentrations and found that punctate fluorescence in the cell interior could still be detected when treating with as low as 2.8 nM assembled capsid particles (0.5 µM MS2 CP monomer concentration) (Figure 2.7). To test uptake into other cell types of interest, U-87 MG glioblastoma cells, HEK293 embryonic kidney cells, and Saos-2 osteosarcoma cells were also treated with MS2, and internalization was evaluated via confocal microscopy and flow cytometry. Cellular uptake was observed in all four cell types, with 7.6-, 6.5-, 36-, and 29-fold increases in fluorescence intensities in MS2-treated HEK293T, HeLa, Saos-2, and U-87 MG cells, respectively (Figure 2.6, Table 2.4).

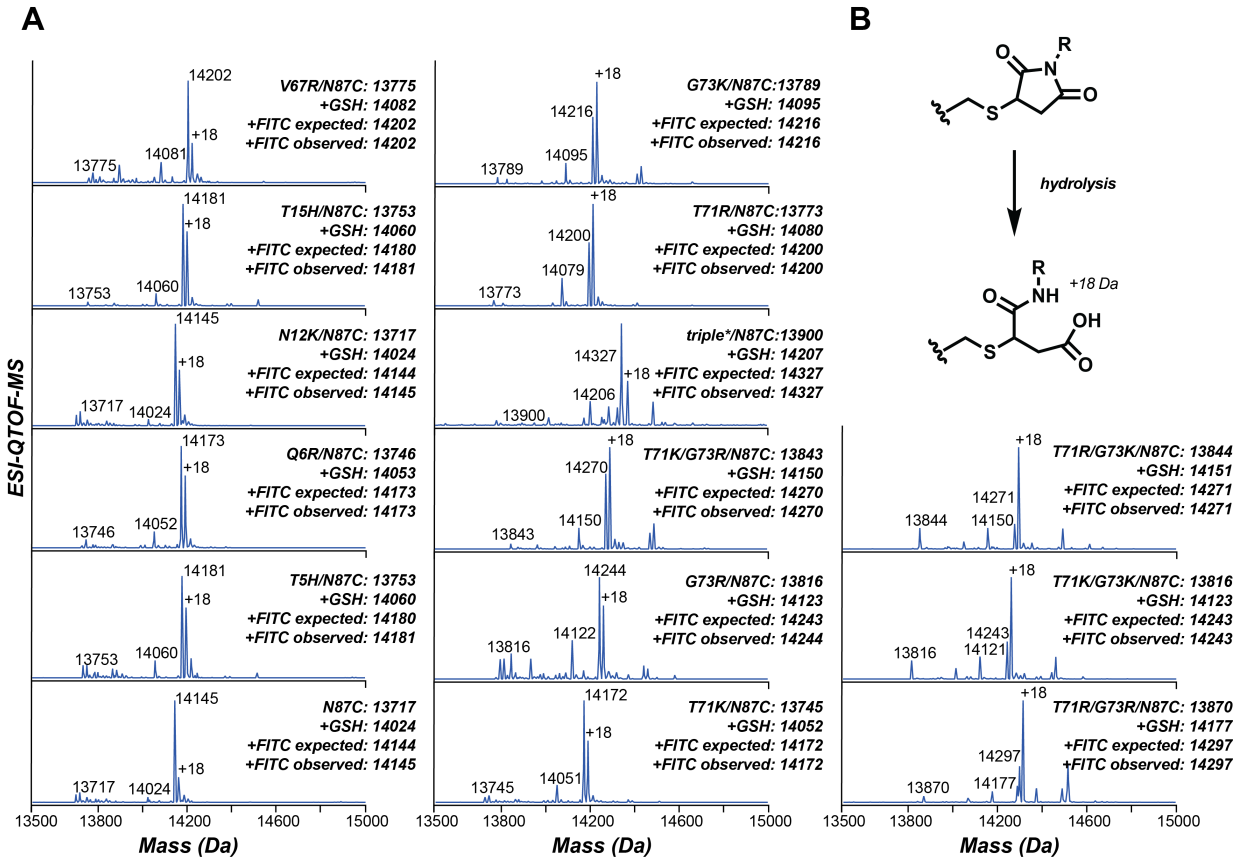


Figure 2.5: **(A)** LC-MS analysis of MS2-fluorescein conjugates. Each variant was modified 72-91% by fluorescein maleimide (FITC, +427 Da), and small amounts of a hydrolysis product (H_2O, +18 Da) and a glutathione (GSH, + 307 Da) addition product were observed. **(B)** Base-catalyzed hydrolysis product (+18 Da) of MS2-fluorescein maleimide conjugates observed in LC-MS traces [174].

Physical and biological characterization of MS2 variants with increased cellular uptake

The biophysical properties of the top-performing capsids with positively charged surface residues, MS2 T71K/G73R and MS2 T71R/G73K, were evaluated with dynamic light scattering (DLS) and compared with wtMS2. The diameters of all three capsids measured were found to be very similar at 28.2 ± 0.5 nm, 27.0 ± 0.6 nm, and 27.2 ± 0.5 nm for wtMS2, MS2 T71K/G73R, and MS2 T71R/G73K, respectively (Figure 2.12). These values are in accordance with literature reports that measured the diameter of wild-type MS2 to be 27 nm [176]. The aggregation point of each variant was measured via a temperature-dependent DLS size screen from 25 °C to 70 °C. The diameter of wtMS2 was stable until 70 °C, consistent with the previously reported melting temperature of 66 °C (Figure 2.12) [177]. The MS2 variants with positively charged surface residues exhibited somewhat lower aggregation

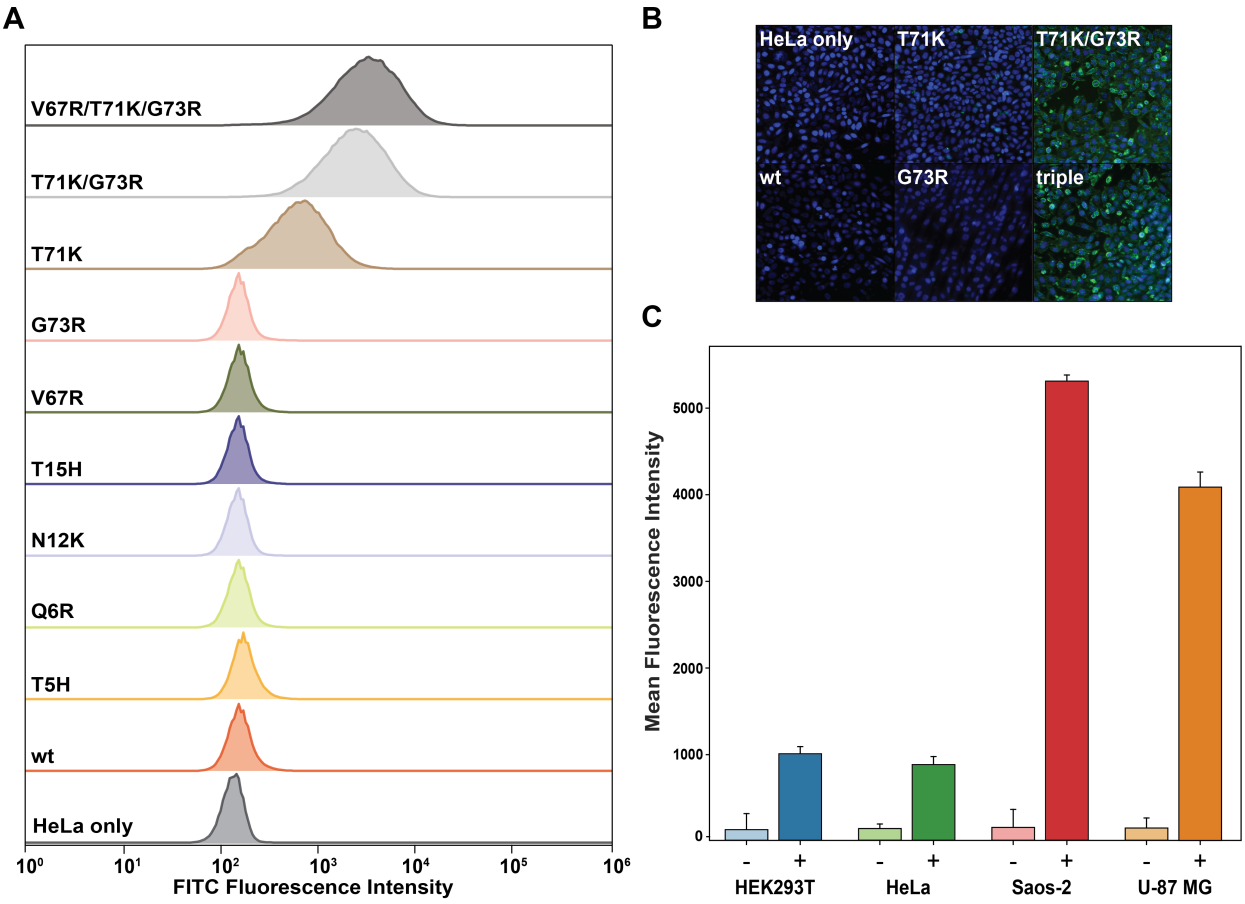


Figure 2.6: **(A)** Histograms showing uptake of MS2-fluorescein variants into HeLa cells. Data shown are a concatenation of three biological replicates. **(B)** Cellular uptake of select MS2-fluorescein variants assessed using fluorescence microscopy. Fixed cell images of HeLa cells treated with 5 µM of the indicated MS2 CP variants. Triple corresponds to MS2 CP variant V67R/T71K/G73R. **(C)** Cellular uptake of 5 µM MS2 T71K/G73R-fluorescein into four different cell types (HEK293T (blue), HeLa (green), Saos-2 (red), and U-87 MG (orange). Data shown are a concatenation of three biological replicates as measured by flow cytometry. Error bars show the coefficient of variation (CV).

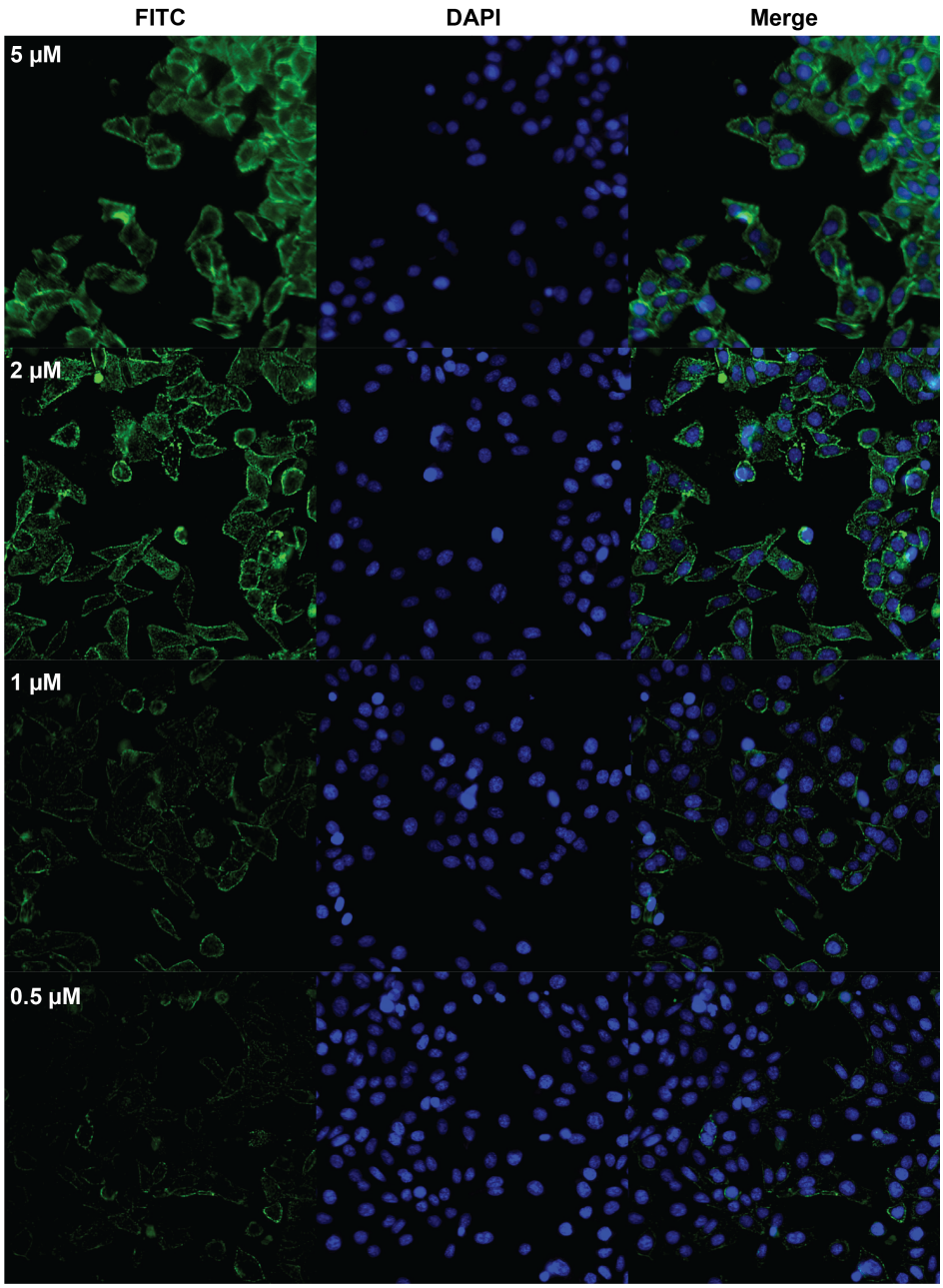


Figure 2.7: Fluorescence microscopy images of MS2-fluorescein internalization at different concentrations. From top to bottom: 5 µM monomers (28 nM capsids), 2 µM (11 nM capsids), 1 µM (5.5 nM capsids), 0.5 µM (2.8 nM).

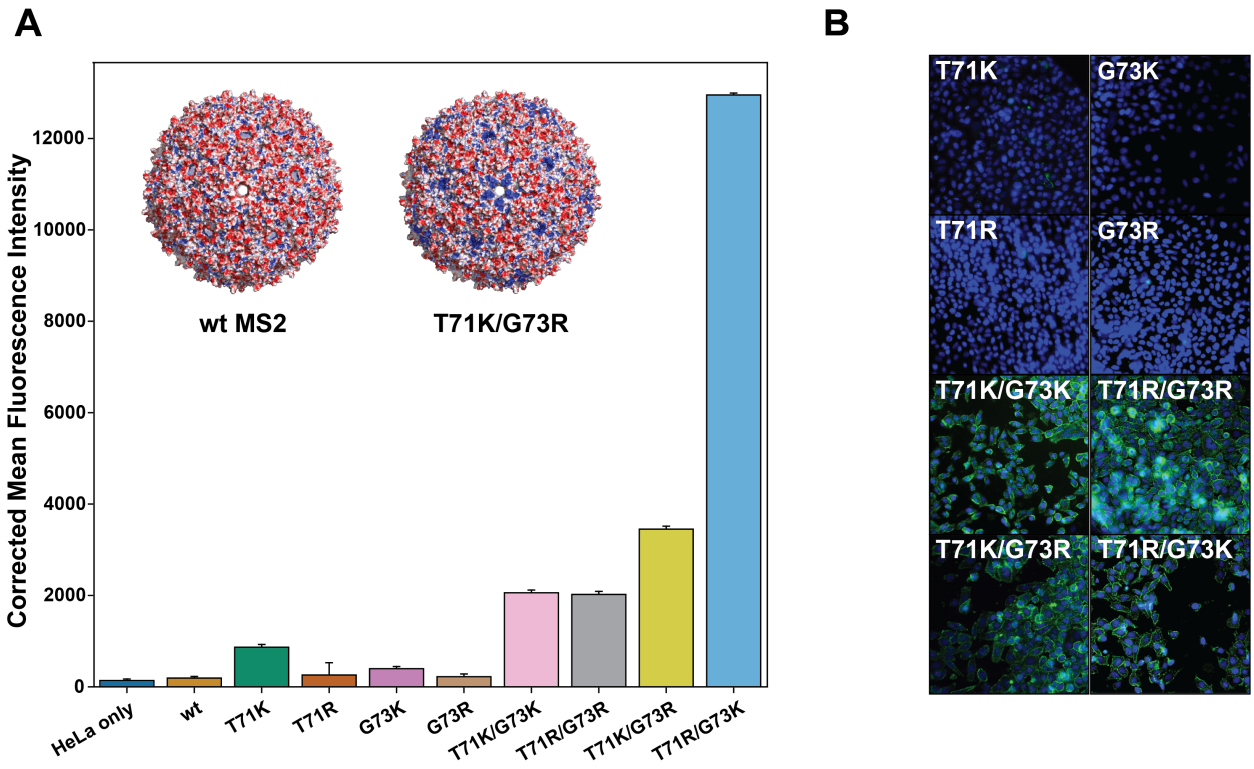


Figure 2.8: **(A)** Bar graphs showing corrected mean fluorescence intensity (MFI) of MS2-fluorescein internalization into HeLa cells. Error bars show the coefficient of variation (CV). Data shown are a concatenation of three biological replicates as measured by flow cytometry. Electrostatic surface potential maps of the wtMS2 and MS2 T71K/G73R capsid are inlaid in the upper portion of the bar graph. Red areas on the structure represent negative charge, while blue areas represent positive surface charge. **(B)** Cellular uptake of MS2-fluorescein variants with all combinations of positive charge at residues 71 and 73 assessed using fluorescence microscopy. Fixed cell images of HeLa cells treated with 5 µM of the indicated MS2 CP variants.

points, with MS2 T71K/G73R aggregating at 55 °C and MS2 T71R/G73K aggregating at 50 °C (Figure 2.12). We then compared the experimental stability of the MS2 variants to the fitness scores calculated in a previous study in our lab that explored the fitness landscape of all MS2 CP double mutants in the FG loop (residues 71-76) [49]. The trend of calculated thermostability scores for wtMS2, MS2 T71K/G73R, and MS2 T71R/G73K mirrored that of the experimental aggregation points, with a positive thermostability score for wtMS2 (0.42) and negative thermostability scores for MS2 T71K/G73R (-0.29) and MS2 T71R/G73K (-0.54) (Table 2.1).

Zeta potential measurements were taken for each MS2 variant. These measurements describe the electrostatic potential at the layer of ions bound to the surface of a particle in solution [178]. The zeta potentials were measured to be -31.2 ± 4.3 mV, -32.3 ± 1.3 mV, and -30.7 ± 1.5 mV for wt MS2, T71K/G73R, and T71R/G73K, respectively (Figure

Treatment	Cell Count	Mean Fluorescence Intensity	Coefficient of Variation	Corrected Mean Fluorescence Intensity
HeLa Only	80755	137	50.2	137
N87C	72234	167	51.9	192
T5H/N87C	86323	185	53.3	223
Q6R/N87C	75705	162	71.1	184
N12K/N87C	85552	157	40.2	178
T15H/N87C	75718	158	112	174
V67R/N87C	86426	163	50.2	199
T71K/N87C	78429	771	77.4	866
G73R/N87C	86475	164	75.3	222
T71K/G73R	86845	3002	79.6	3451
Triple*/N87C	68515	4081	81.2	5038
T71R/N87C	82468	217	285	258
G73K/N87C	80755	345	64.3	397
T71R/G73R/N87C	78588	1820	81.1	2022
T71K/G73K/N87C	79780	1584	76.4	2057
T71R/G73K/N87C	82054	9326	56.1	12953

Table 2.3: Mean flow cytometry fluorescence intensity values with coefficient of variation for MS2-fluorescein internalization into HeLa cells.

Treatment	Cell Count	Median Fluorescence Intensity	Mean Fluorescence Intensity	Coefficient of Variation
HEK293T only	35110	124	131	152
HEK293T + MS2	39081	678	997	103
HeLa only	62664	130	134	72.3
HeLa + MS2	70525	638	872	113
Saos-2 only	34362	130	148	227
Saos-2 + MS2	54264	4033	5299	90.7
U-87 MG only	79218	122	141	135
U-87 MG + MS2	20497	2084	4078	191

Table 2.4: Mean flow cytometry fluorescence intensity values with coefficient of variation for MS2 T71K/G73R-fluorescein internalization into HeLa, Saos-2, HEK293T, and U-87 MG cells.

2.12). The similarity of the zeta potentials is corroborated by the isoelectric points (pIs) of each variant and the pK_as of each residue between the single and double mutants calculated using PROPKA pK_a values (Figure 2.9, Table 2.5-2.6) [179, 180]. Negative zeta potential measurements for all capsid variants confirmed our prediction that locally supercharged MS2 particles would retain their negative charge overall. This differs from other most other well-characterized cationic protein delivery vehicles and super-charged proteins, which generally possess an overall net positive charge that can be visualized via theoretical electrostatic surface potential maps (Figure 2.12).

To gain some preliminary insight into the mechanism by which MS2 capsids with positively charged surface residues enter cells, internalization experiments were repeated after treating cells with drugs that inhibit different endocytosis pathways and quantitated by flow cytometry [181]. Treatment of cells with cytochalasin D, dynasore, taxol, or methyl-β-

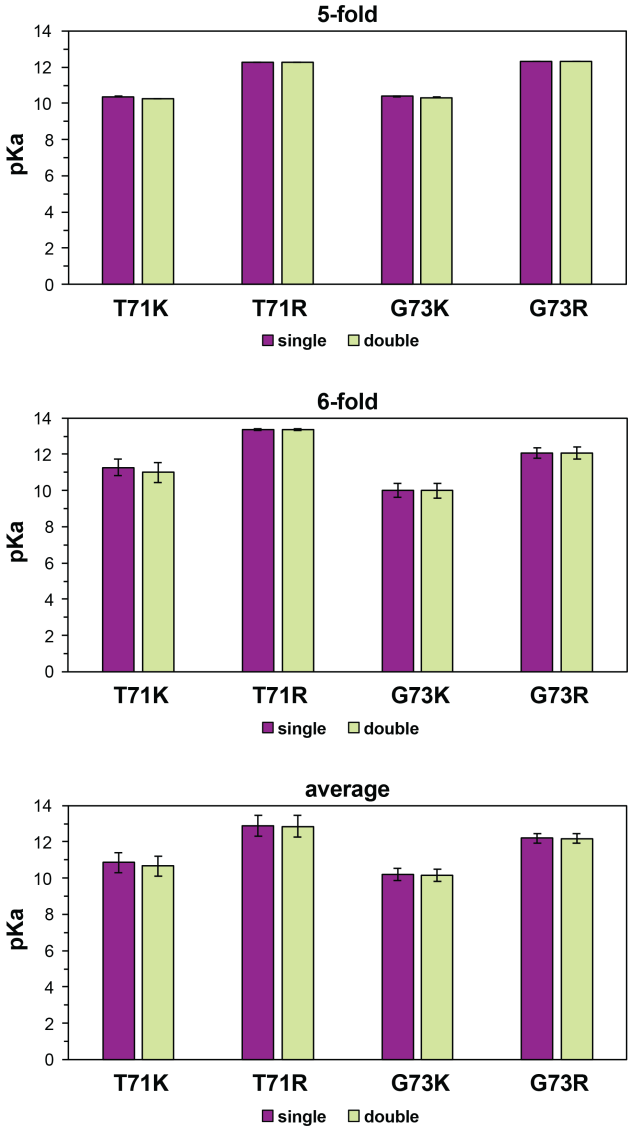


Figure 2.9: Comparison of calculated pK_as of residues at MS2 CP positions 71 and 73 between single and double mutants. Bar graph shows average single mutant pK_as (purple) and average double mutant pK_as (green). Error bars represent one standard deviation.

MS2 CP Variant	Expasy pI (sequence)	IPC2 pI (sequence)	PROPKA pI (20mer)	PROPKA pI (12mer)
wt	7.93	6.78	8.57	8.51
T71K/G73R	8.87	7.91	8.75	8.70
T71R/G73K	8.87	7.92	8.75	8.69

Table 2.5: Isoelectric point (pI) estimates for MS2 CP variants calculated using Expasy, IPC2, and PROPKA

MS2 CP Variant	Residue	20mer pK_a	12mer pK_a	Average pK_a
T71K/G73R	T71K	10.27	11.01	10.67
T71K/G73R	G73R	12.33	12.06	12.18
T71R/G73K	T71R	12.26	13.36	12.86
T71R/G73K	G73K	10.33	9.99	10.14
T71R	T71R	12.28	13.37	12.87
T71K	T71K	10.37	11.27	10.86
G73R	G73R	12.34	12.09	12.20
G73K	G73K	10.42	10.02	10.20

Table 2.6: pK_a estimated for MS2 CP variants calculated using PROPKA

cyclodextrin resulted in varied reduction of MS2 T71K/G73R or MS2 T71R/G73K internalization as measured by flow cytometry, but no major morphological changes in uptake were observed in confocal microscopy images (Figure 2.13).

Each of these inhibitors targets a different mechanism of endocytosis, with dynasore preventing the bifurcation of clathrin-coated endosomes, taxol stabilizing microtubules, and methyl-β-cyclodextrin (MβCD) extracting cholesterol from the plasmid membrane [181–183]. However, it is known that these inhibitors are not always direct and specific, and it is likely that MS2 T71K/G73R can enter cells through multiple endocytic pathways. Uptake of MS2 T71K/G73R and MS2 T71R/G73K was greatly reduced in cells cooled to 4 °C or treated with heparin, a heavily sulfated glycosaminoglycan, before and during MS2 exposure (Figure 2.13, Table 2.7). These results suggest that uptake of charged MS2 variants is an energy-dependent process that may depend on initial capsid binding to cell-surface heparan sulfate proteoglycans. This is consistent with previous reports of other positively-charged molecules, such as HIV-Tat and +36 GFP, that require binding for internalization [161, 181, 184].

To test for potential cytotoxic effects during internalization experiments, up to 20 µM concentrations (based on CP monomer) of either wtMS2 or the best-performing variants were incubated with HeLa and U-87 MG cells for 45 min (Figure 2.10). Under normal treatment concentrations of 5 µM MS2, low toxicity was observed in both HeLa (<12%) and U-87 MG (<4%) cells. Toxicity increased in both cell types with higher MS2 concentrations, reaching 28% and 22% cytotoxicity for HeLa and U-87 MG cells at a treatment concentration of 20 µM MS2. Similar cytotoxicity levels were observed whether cells were treated with wtMS2, MS2 T71K/G73R, or MS2 T71R/G73K, suggesting that these uptake-enhanced variants do not result in the increased cytotoxicity common to globally cationic materials [185, 186].

A hemolysis assay was also performed to evaluate the potential hemolytic activity of the best-performing MS2 variants (Figure 2.11) [187]. Up to 20 µM MS2 was incubated with red blood cells for 3 h at 37 °C, and released heme was measured. As a positive control, red blood cells (RBCs) were also incubated with Lipofectamine 2000, a cationic lipid-based DNA transfection reagent that is known to cause hemolysis and other cytotoxic effects [188, 189]. Very little (1%) hemolysis was observed in MS2-treated samples, even at the highest concentration of 20 µM MS2. Increasing hemolysis was observed in the Lipofectamine 2000-treated cells, with up to 7.3 ± 1.4% hemolysis in RBCs treated with the

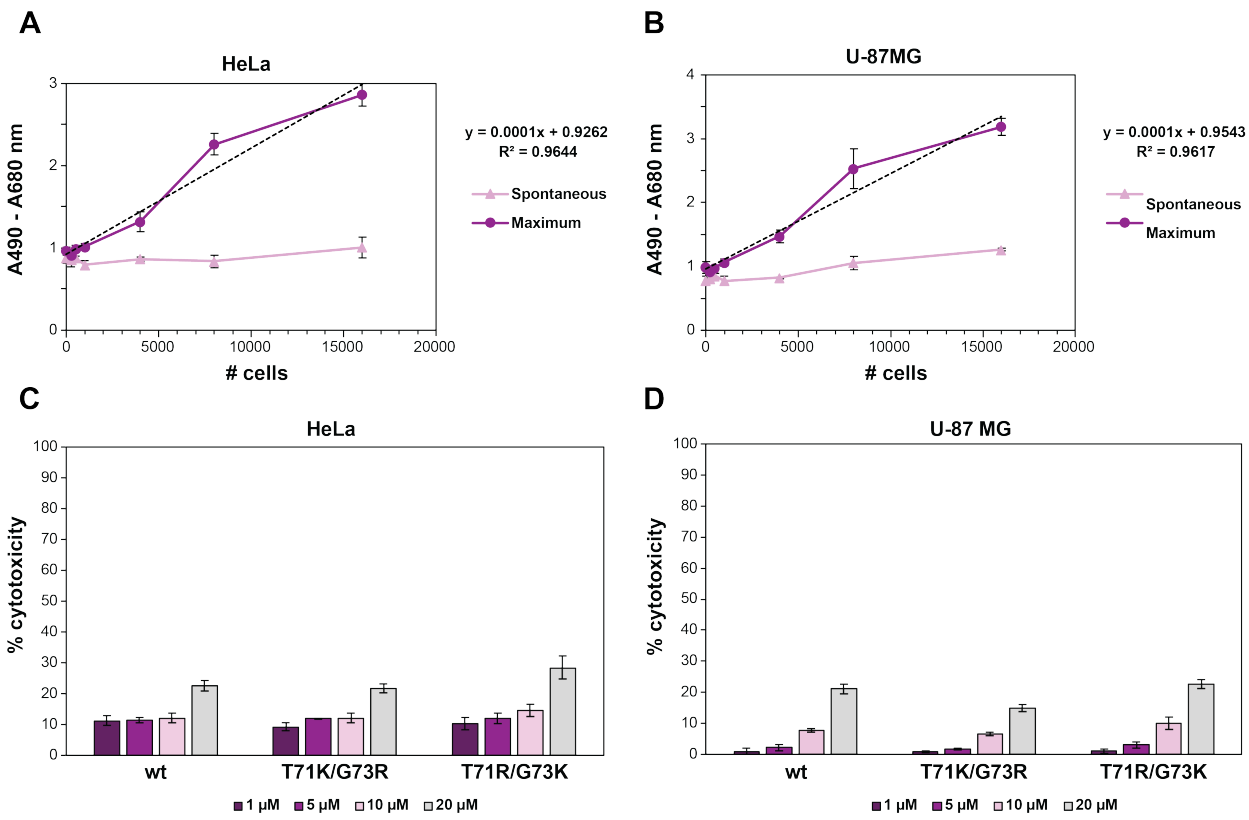


Figure 2.10: **(A)** LDH cytotoxicity assay standard curves for HeLa cells. **(B)** LDH cytotoxicity assay standard curves for U-87 MG cells. **(C)** LDH cytotoxicity assay for HeLa cells treated with 1, 5, 10, or 20 µM wt MS2, MS2 T71K/G73R, or MS2 T71R/G73K. Percent cytotoxicity shown as the mean of three biological replicates. Error bars show one standard deviation. **(D)** LDH cytotoxicity assay for U-87 MG cells treated with 1, 5, 10, or 20 µM wt MS2, MS2 T71K/G73R, or MS2 T71R/G73K. Percent cytotoxicity shown as the mean of three biological replicates. Error bars show one standard deviation.

highest Lipofectamine 2000 concentration of 0.05 mg/mL. Hemolysis levels did not change in cells treated with different MS2 variants. Taken together, these results indicate that capsids with positively charged surface residues have the potential to be safe and effective *in vivo* delivery vehicles for biotherapeutics.

Cationic MS2-mediated delivery of MMAE to glioblastoma cells

We next determined whether the uptake-enhancing mutations would lead to enhanced efficacy for a drug molecule. Monomethyl auristatin E (MMAE) is a potent antimitotic drug that is generally employed as a covalent construct to cancer-targeting monoclonal antibodies (mAbs) to produce antibody drug conjugates (ADCs). Engineered mAbs with substituted cysteines, known as THIOMABs, have been developed to allow the conjugation of drug molecules to antibodies using maleimide handles [190]. A dipeptide Val-Cit linker is typi-

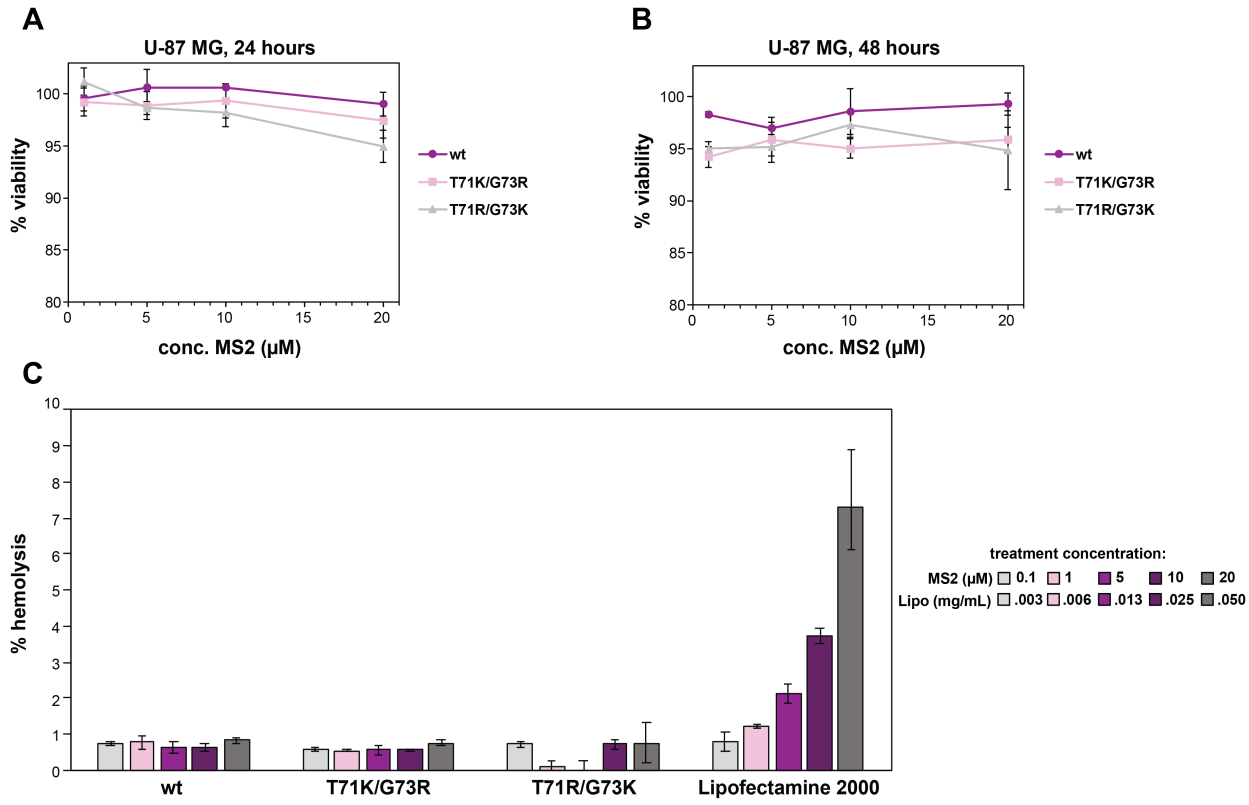


Figure 2.11: **(A)** MTS assay of 1, 5, 10, and 20 µM wt MS2 (purple circles), MS2 T71K/G73R (pink squares), or MS2 T71R/G73K (grey triangles) incubated with U-87 MG cells for 24 h. Plot shows average % viability of three biological replicates. Error bars represent one standard deviation. **(B)** MTS assay of 1, 5, 10, and 20 µM wt MS2 (purple circles), MS2 T71K/G73R (pink squares), or MS2 T71R/G73K (grey triangles) incubated with U-87 MG cells for 48 h. Plot shows average % viability of three biological replicates. Error bars represent one standard deviation. **(C)** Hemolysis assay measured after incubating 0.1-20 µM wt MS2, MS2 T71K/G73R, MS2 T71R/G73K, or 0.003-0.050 mg/mL Lipofectamine 2000 with red blood cells for 3 h at 37 °C. Percent hemolysis shown as the average of two biological replicates. Error bars show one standard deviation.

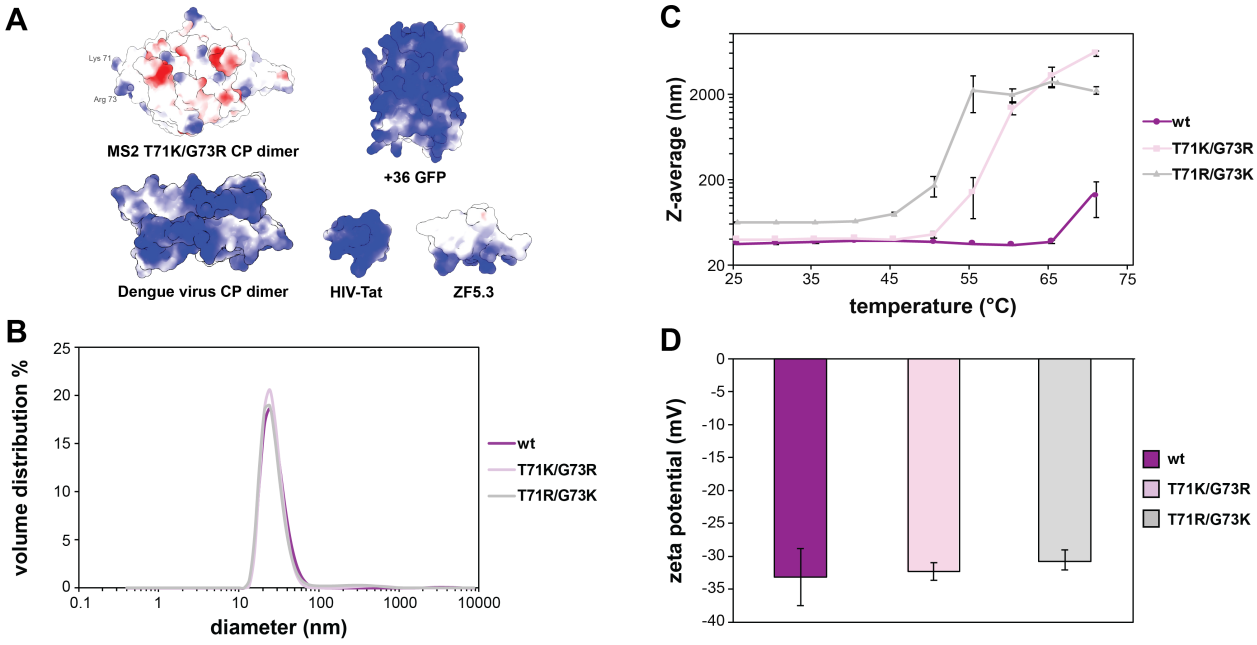


Figure 2.12: **(A)** Theoretical electrostatic potential maps of the MS2 T71K/G73R CP dimer exterior face, Dengue virus CP dimer exterior face (PDB: 1R6R), +36 GFP (PDB: 2B3P), HIV-Tat (PDB: 1TBC), and ZF5.3 (PDB: 2EOZ). Engineered structures were created using the PyMOL mutagenesis tool. **(B)** DLS spectra of wtMS2 (purple), MS2 T71K/G73R (pink), and MS2 T71R/G73K (grey) in 10 mM sodium phosphate, pH 7.2. **(C)** Z-average (nm) vs temperature (°C) for wtMS2 (purple circles), MS2 T71K/G73R (pink squares), and MS2 T71R/G73K (grey triangles) in 10 mM sodium phosphate, pH 7.2. Error bars show one standard deviation. (D) Zeta potentials (mV) of wtMS2 (purple), MS2 T71K/G73R (pink), and MS2 T71R/G73K (grey) in 10 mM sodium phosphate, pH 7.2. Error bars show one standard deviation.

cally incorporated, as it is cleaved by the cathepsin B lysosomal protease upon cell entry to release the free drug in a targeted delivery approach [191–193]. The half maximal inhibitory concentration (IC_{50}) of MMAE has been measured to be close to 1 nM in multiple cancer cell lines in *in vitro* experiments, and similar inhibitory concentrations have been calculated for MMAE ADCs as well [194]. We hypothesized that conjugating MMAE to MS2 variants with positively charged surface residues could produce an equally or even more potent dose response given its potential to load up to 180 copies of a drug molecule per capsid, in comparison to only two drug molecules per mAb in most ADCs [194]. Maleimide-Val-Cit-PAB-MMAE was conjugated to the interior cysteine of wtMS2, MS2 T71K/G73R, and MS2 T71R/G73K (Figure 2.15). Each MS2 CP variant was modified to 92-97% by monomer with MMAE, or about 165-175 molecules per capsid (Figure 2.14).

To test for potential cytotoxic effects during multi-day dose response experiments, up to 20 µM drug-free MS2 was first incubated with U-87 MG cells for up to 72 h. Cell viability decreased slightly with higher MS2 concentrations, but cells treated with all three MS2 variants were >85% viable after 72 h (Figure 2.15, Figure 2.11). The efficacy of MS2-

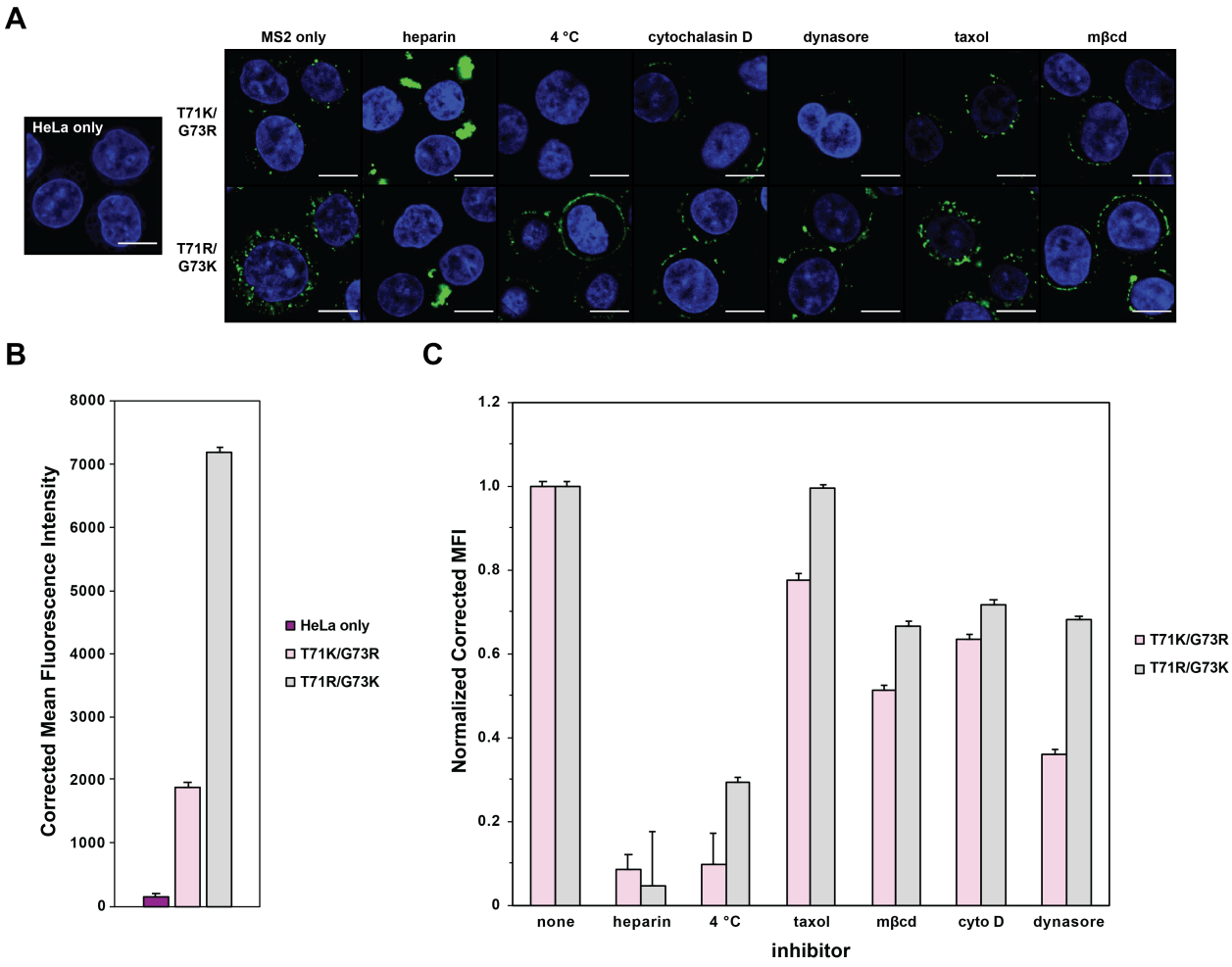


Figure 2.13: **(A)** Cellular uptake of MS2 T71K/G73R-fluorescein and MS2-T71R/G73K-fluorescein in the presence of endocytosis inhibitors assessed using confocal microscopy. Fixed cell images of HeLa cells treated with 5 µM MS2 T71K/G73R/N87C-fluorescein and the indicated endocytosis inhibitor. **(B)** Bar graphs showing corrected mean fluorescence intensity (MFI) of MS2-fluorescein internalization into HeLa cells. Error bars show the coefficient of variation (CV). Data shown are a concatenation of three biological replicates as measured by flow cytometry. **(C)** Bar graphs showing normalized cellular uptake of 5 µM MS2 T71K/G73R and MS2 T71R/G73K in the presence of endocytosis inhibitors. Data shown are a concatenation of three biological replicates as measured by flow cytometry. Error bars show the normalized coefficient of variation (CV).

Treatment	Cell Count	Median Fluorescence Intensity	Mean Fluorescence Intensity	Corrected MFI	Coefficient of Variation
HeLa only	18667	138	150	150	73.9
MS2 T71K/G73R only	6069	1481	1594	1881	75.4
T71K/G73R + heparin	5593	173	251	296	260
T71K/G73R + cyto D	9576	873	1058	1248	84.5
T71K/G73R + dynasore	8186	495	653	771	88.1
T71K/G73R + taxol	2163	1059	1265	1493	104
T71K/G73R + mβcd	27829	678	876	1034	101
T71K/G73R + 4 °C	53080	219	269	317	542
MS2 T71R/G73K only	49030	7568	7189	7189	71
T71R/G73K + heparin	51983	183	467	467	927
T71R/G73K + cyto D	27590	4974	5198	5198	87.8
T71R/G73K + dynasore	40303	4712	4928	4928	71.6
T71R/G73K + taxol	27968	7620	7150	7150	66.4
T71R/G73K + mβcd	29590	4301	4834	4834	85.9
T71R/G73K + 4 °C	57096	1845	2215	2215	81.6

Table 2.7: Mean flow cytometry fluorescence intensity values with coefficient of variation for MS2 T71K/G73R-fluorescein and MS2 T71R/G73K-fluorescein internalization into HeLa cells in the presence of endocytosis inhibitors.

MMAE was next measured by a dose-response assay in U-87 MG cells. Cells were treated for 72 h with up to 1000 nM MMAE conjugated to either wtMS2, MS2 T71K/G73R, or MS2 T71R/G73K. The calculated IC_{50} values for MMAE treatment with each MS2 variant were 85.30 nM, 1.48 nM, and 2.95 nM for wtMS2, MS2 T71K/G73R, and MS2 T71R/G73K, respectively (Figure 2.13). These data show that MMAE delivery with engineered variants results in up to a 57-fold increase in efficacy versus delivery of MMAE with wtMS2, and a treatment concentration of only 10 pM assembled capsids is needed to elicit this potent cytotoxic response. Additionally, the IC_{50} for MS2-MMAE treatment with MS2 variants with positively charged surface residues is comparable to that of MMAE alone and MMAE-ADCs, demonstrating that locally supercharged MS2 capsids can be an effective delivery vehicle for potent anticancer therapeutics [194]. It was perhaps unanticipated that both engineered capsids performed similarly in drug delivery, but there are several possible explanations, such as the different time and concentration scales for the fluorescently-labeled MS2 uptake experiments (1 h, 5 µM capsids) versus MMAE delivery (72 h, 0.5 nM-1 µM). We are in the process of confirming these differences further, but it remains true that both capsids have substantially better delivery performance in comparison to wtMS2.

2.4 Conclusion

Previous work has established fitness landscaping as a successful method for identifying MS2 CP variants with improved properties such as increased thermostability, acid sensitivity, and chemical modifiability [49, 50, 151]. Here, we capitalize on the nanoscale assembly of MS2-based VLPs to create locally supercharged variants with positively charged surface

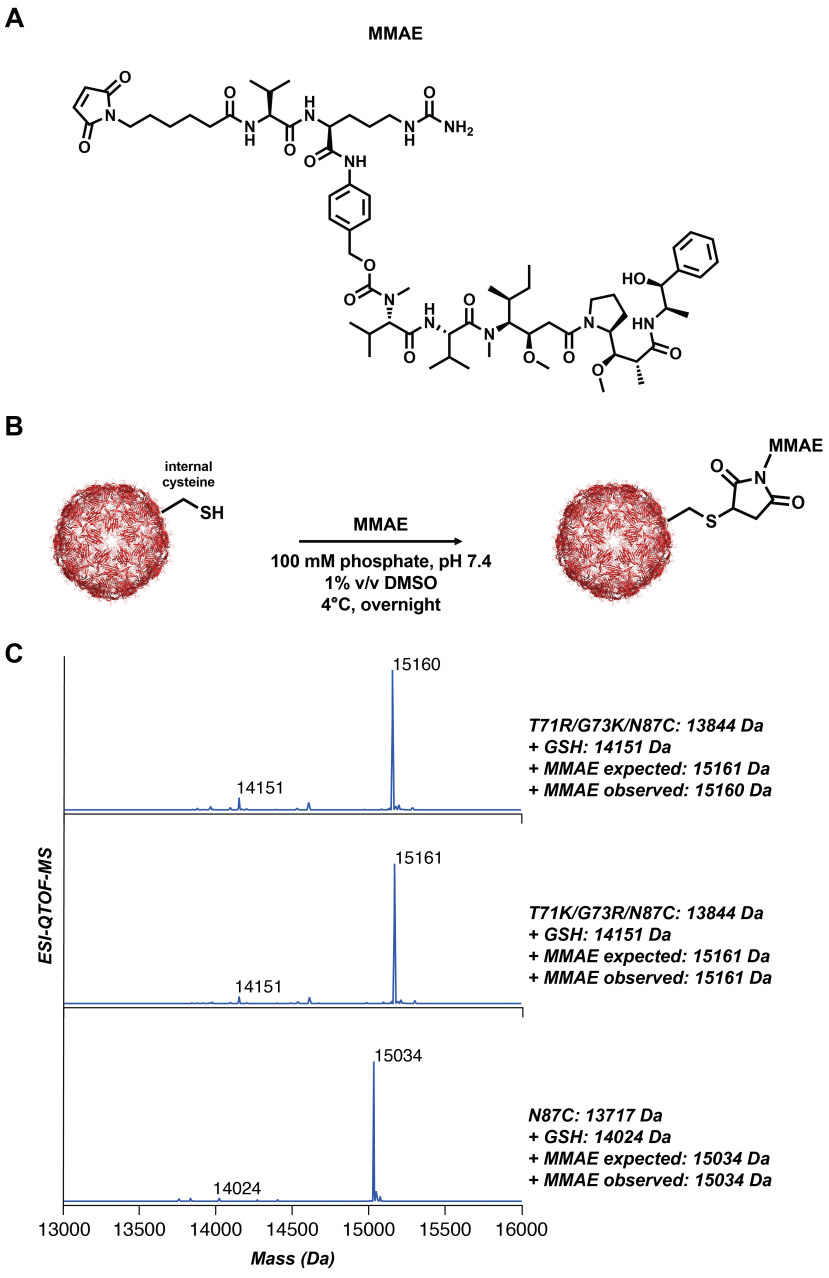


Figure 2.14: **(A)** Structure of maleimide-Val-Cit-PAB-MMAE (MMAE). **(B)** Reaction scheme describing maleimide-Val-Cit-PAB-MMAE coupling to the internal cysteine N87C of MS2 CP. **(C)** LC-MS analysis of MS2-MMAE conjugates. Each variant was modified 92-97% by maleimide-Val-Cit-PAB-MMAE (MMAE, +1317 Da), and small amounts of a glutathione (GSH, + 307 Da) addition product were observed.

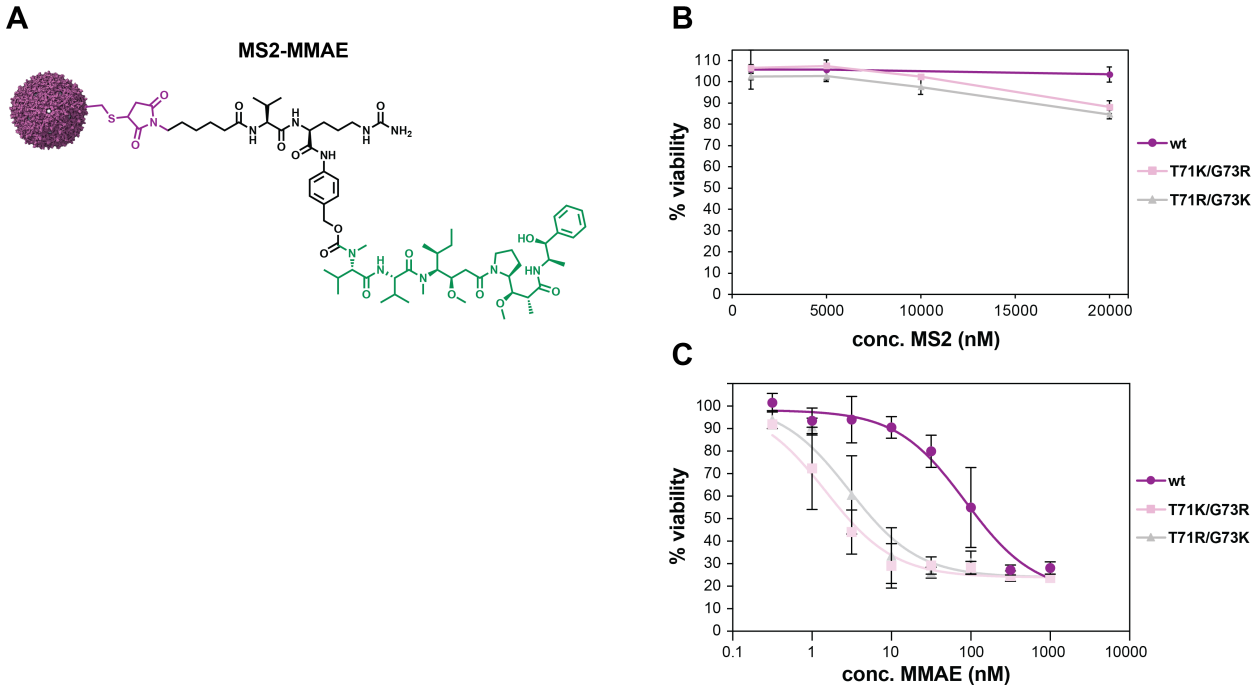


Figure 2.15: **(A)** Structure of MS2-MMAE conjugate. MS2 capsid with interior cysteine conjugated to maleimide handle (purple), Val-Cit linker and spacer (black), and MMAE (green). **(B)** MTS viability assay of 1, 5, 10, and 20 µM wtMS2 (purple circles), MS2 T71K/G73R (pink squares), or MS2 T71R/G73K (grey triangles) incubated with U-87 MG cells for 72 h. Plot shows average % viability of three biological replicates. Error bars represent one standard deviation. **(C)** MS2-MMAE dose response assay. Results are shown for an MTS assay of U-87 MG cells 72 h after treatment with 0.5-1000 nM MMAE. Plot shows average % viability of three biological replicates. Error bars show one standard deviation.

MS2 Variant	Unmodified Mass	+MMAE Mass (Expected)	+MMAE Mass (Observed)	+GSH Mass	%MMAE Modification
N87C	13717	15034	15034	14024	97
T71K/G73R/N87C	13844	15161	15161	14151	94
T71R/G73K/N87C	13844	15161	15160	14151	92

Table 2.8: Masses (Da) of products obtained from MS2 CP variant maleimide-Val-Cit-PAB-MMAE (MMAE) labeling reactions determined by QTOF-ESI-MS.

residues for increased mammalian cell uptake. Two key double mutants with positive charge concentrated at capsid pores were identified and found to exhibit greatly increased cellular penetration compared to wtMS2. Internalization of these variants was observed for multiple cell types and the capsids were found to have low cytotoxic and hemolytic activity. These features add to their promise as effective drug delivery vehicles. When conjugated to MMAE, a potent anticancer small molecule drug, MS2 T71K/G73R and MS2 T71R/G73K can deliver MMAE to glioblastoma cells and produce cytotoxic responses with low-nanomolar efficacies that are comparable to those of MMAE-ADCs. This demonstrates that MS2 variants with positively charged surface residues can be effective small molecule delivery vehicles. These results show that this design concept can be applied to drug delivery, and further studies could help overcome current limits in delivery technology by optimizing the encapsulation and delivery of other small molecule- and nucleic acid-based therapeutics. In current work we are evaluating the in vivo characteristics of these promising delivery vehicles, as well as their ability to transfer other cargo types, such as proteins and nucleic acids, into cancer cells.

2.5 Materials

General information

All reagents were obtained from commercial sources and used without further purification unless otherwise indicated. Milli-Q (MQ) H_2O was purified to a resistivity of 18.2 M Ω•cm (at 25 °C) using a MQ Gradients ultrapure water purification system from Millipore (Burlington, MA).

Plasmid design, protein expression and purification

DNA primers for Golden Gate Assembly were purchased from Integrated DNA Technologies (Coralville, IA). Phusion™ High-Fidelity DNA Polymerase, Phusion™ HF Buffer, deoxynucleotide (dNTP) solution mix, T4 DNA ligase, BsaI and DpnI were purchased from New England BioLabs (Ipswich, MA). Wizard® SV Gel and PCR Clean-Up System was purchased from Promega (Madison, WI). E. coli DH10B cells were purchased from the UC Berkeley MacroLab (Berkeley, CA). Zyppy™ plasmid miniprep kit was purchased from Zymo Research (Irvine, CA). DNA sequencing was performed by Sequetech. Corning® Costar® Spin-X® centrifuge tube filters, Amicon Ultra-0.5 mL 100 kDa MWCO filters, and 2x YT medium powder were purchased from Sigma Aldrich (St. Louis, MO). HiScreen Capto Core 700 column, Microspin™ G-25 columns, and Amersham NAP-5 columns were purchased from Cytiva Lifesciences (Marlborough, MA). Bio SEC-5 HPLC column was purchased from Agilent (Santa Clara, CA). NuPAGE™ 4 to 12%, Bis-Tris precast gels, NuPAGE™ MES SDS Running Buffer and Fluorescein-5-Maleimide were purchased from Thermo Fisher (Waltham, MA).

Cell culture and assays

HeLa, U-87 MG, Saos-2, and HEK293T cells were purchased from the UC Berkeley Cell Culture Facility. Dulbecco's modified eagle medium (DMEM, with and without Phenol Red), Dulbecco's phosphate-buffered saline (DPBS), TrypLE, Hoechst 33342 stain, Invitrogen™ CyQUANT™ LDH Cytotoxicity Assay kit, glutamine, and sodium pyruvate were purchased from Thermo Fisher (Waltham, MA). MTS Assay Cell Proliferation Kit was purchased from Abcam (Cambridge, UK). Fibronectin was purchased from MilliporeSigma (Burlington, MA). Heparin sodium was purchased from Neta Scientific (Hainesport, NJ). Cytochalasin D, dynasore hydrate, taxol, and methyl-β-cyclodextrin were purchased from Sigma Aldrich (St. Louis, MO).

Equipment

For plasmid and protein concentration quantification, a ND-1000 (NanoDrop) spectrophotometer was used. A Sorvall X Pro Series centrifuge was used for protein expression (Thermo Fisher). An AKTA start FPLC (Cytiva), with a HiScreen Capto Core 700 column was used for protein purification. A 1260 Infinity HPLC (Agilent) was used for MS2 assembly confirmation and a 6530 LC/QTOF (Agilent) mass spectrometer was used for characterization of MS2 variants. For cellular internalization, confocal microscopy, and fluorescence correlation spectroscopy, an Attune NxT Flow Cytometer (Thermo Fisher), Image Xpress Micro (Molecular Devices) and LSM 880 (Zeiss) were used. Dynamic light scattering was performed on a Zetasizer Nano ZS (Malvern Instruments). Absorption readings after MTS cell proliferation assays were performed on an Infinite 200 PRO plate reader (Tecan).

2.6 Methods

Safety note

No unexpected or unusually high safety hazards were encountered. MMAE is a highly toxic drug and should be handled with care.

Cloning procedure

EMPIRIC cloning was used to generate all MS2 variants [195]. Entry vector plasmids containing self-encoded removable fragments (SERF) flanked by inverted BsaI recognition sites were previously used to generate all single amino acid mutations of the MS2 coat protein. Two single-stranded DNA primers were purchased, resuspended, and diluted to 50 ng/µL for each MS2 CP variant. Overlap extension PCR with the corresponding primer completed the reverse strand, and the double-stranded DNA was purified by Wizard® SV Gel and PCR Clean-Up System, diluted to 1-5 ng/µL, and cloned into the corresponding entry vector using

Golden Gate cloning. Ligated plasmids were digested with DpnI to remove methylated template DNA and transformed into chemical competent DH10B *E. coli* cells. Cells were plated onto LB agar plates containing 20 µg/mL chloramphenicol and grown overnight at 37 °C. Individual colonies were picked and grown overnight in 2x YT media containing 20 µg/mL chloramphenicol at 37 °C, then plasmid DNA was isolated by Zyppy™ plasmid miniprep kit and sent for sequencing.

DNA primer names

Primer Number	Mutation Name
1	EV3 G73R F
2	EV3 G73R R
3	EV1 N12K F
4	EV1 R
5	EV1 Q6R F
6	EV1 T5H F
7	EV1 T15H F
8	EV1 T15H R
9	EV3 T71K F
10	EV3 T71K R
11	EV3 T71K G73R F
12	EV3 T71K G73R R
13	EV3 T71K V67R F
14	EV3 T71K V67R R
15	EV3 V67R F
16	EV3 V67R R
17	EV3 V67R G73R F
18	EV3 V67R G73R R
19	EV3 V67R T71K G73R F
20	EV3 V67R T71K G73R R
21	EV3 T71R F
22	EV3 T71R R
23	EV3 G73K F
24	EV3 G73K R
25	EV3 T71K G73K F
26	EV3 T71K G73K R
27	EV3 T71R G73R F
28	EV3 T71R G73R R
29	EV3 T71R G73K F
30	EV3 T71R G73K R

Table 2.9: Primer names for EMPIRIC cloning to generate MS2 variants.

DNA primer sequences

Number	Sequence
1	AGGTCTCACTCTGCGCAGAATCGCAAATACACCATCAAAGTCGAGGTGCCTAAAAGTGGCA
2	AGGTCTCACTACAGGAAGCTCTACACCACGAACAGTCTGGGTTGCCACTTTAGGCACCTC
3	AGGTCTCACATGGCTTCTAACTTTACTCAGTTCGTTCTCGTCGACAAGGGCGGAACTGGC
4	AGGTCTCACGTTAGCGAAGTTGCTTGGGGCGACAGTCACGTCGCCAGTTCCGCCATTGTC
5	AGGTCTCACATGGCTTCTAACTTTACTCGGTTCGTTCTCGTCGACAATGGCGGAACTGGC
6	AGGTCTCACATGGCTTCTAACTTTCATCAGTTCGTTCTCGTCGACAATGGCGGAACTGGC
7	AGGTCTCACATGGCTTCTAACTTTACTCAGTTCGTTCTCGTCGACAATGGCGGACATGGC
8	AGGTCTCACGTTAGCGAAGTTGCTTGGGGCGACAGTCACGTCGCCATGTCCGCCATTGTC
9	AGGTCTCACTCTGCGCAGAATCGCAAATACACCATCAAAGTCGAGGTGCCTAAAGTGGCA
10	AGGTCTCACTACAGGAAGCTCTACACCACCAACTTTCTGGGTTGCCACTTTAGGCACCTC
11	AGGTCTCACTCTGCGCAGAATCGCAAATACACCATCAAAGTCGAGGTGCCTAAAGTGGCA
12	AGGTCTCACTACAGGAAGCTCTACACCACGAACTTTCTGGGTTGCCACTTTAGGCACCTC
13	AGGTCTCACTCTGCGCAGAATCGCAAATACACCATCAAAGTCGAGGTGCCTAAACGGGCA
14	AGGTCTCACTACAGGAAGCTCTACACCACCAACTTTCTGGGTTGCCCGTTTAGGCACCTC
15	AGGTCTCACTCTGCGCAGAATCGCAAATACACCATCAAAGTCGAGGTGCCTAAACGGGCA
16	AGGTCTCACTACAGGAAGCTCTACACCACCAACAGTCTGGGTTGCCCGTTTAGGCACCTC
17	AGGTCTCACTCTGCGCAGAATCGCAAATACACCATCAAAGTCGAGGTGCCTAAACGGGCA
18	AGGTCTCACTACAGGAAGCTCTACACCACGAACAGTCTGGGTTGCCCGTTTAGGCACCTC
19	AGGTCTCACTCTGCGCAGAATCGCAAATACACCATCAAAGTCGAGGTGCCTAAACGGGCA
20	AGGTCTCACTACAGGAAGCTCTACACCACGAACTTTCTGGGTTGCCCGTTTAGGCACCTC
21	AGGTCTCACTCTGCGCAGAATCGCAAATACACCATCAAAGTCGAGGTGCCTAAAGTGGCA
22	AGGTCTCACTACAGGAAGCTCTACACCACCAACTCTCTGGGTTGCCACTTTAGGCACCTC
23	AGGTCTCACTCTGCGCAGAATCGCAAATACACCATCAAAGTCGAGGTGCCTAAAGTGGCA
24	AGGTCTCACTACAGGAAGCTCTACACCTTTAACAGTCTGGGTTGCCACTTTAGGCACCTC
25	AGGTCTCACTCTGCGCAGAATCGCAAATACACCATCAAAGTCGAGGTGCCTAAAGTGGCA
26	AGGTCTCACTACAGGAAGCTCTACACCTTTAACTTTCTGGGTTGCCACTTTAGGCACCTC
27	AGGTCTCACTCTGCGCAGAATCGCAAATACACCATCAAAGTCGAGGTGCCTAAAGTGGCA
28	AGGTCTCACTACAGGAAGCTCTACACCTCTAACTCTCTGGGTTGCCACTTTAGGCACCTC
29	AGGTCTCACTCTGCGCAGAATCGCAAATACACCATCAAAGTCGAGGTGCCTAAAGTGGCA
30	AGGTCTCACTACAGGAAGCTCTACACCTTTAACTCTCTGGGTTGCCACTTTAGGCACCTC

Table 2.10: Primer sequences for EMPIRIC cloning to generate MS2 variants.

Expression and purification of proteins

Overnight cultures of each MS2 variant were subcultured 1:200 into 1 L of 2x YT media containing 20 µg/mL chloramphenicol and grown to an OD_{600} of 0.4-0.6, then induced with 0.1% w/v arabinose. Proteins were expressed overnight at 37 °C, then cells were harvested by centrifugation and lysed by sonication. MS2 capsids were precipitated with one round of 50% ammonium sulfate (single positive charge mutants) or 20% PEG-6000 (double positive charge mutants). Large-scale expressions of well-assembled MS2 variants were purified via FPLC with a HiScreen Capto Core 700 column via isocratic flow with 10 mM phosphate buffer at pH 8.5 with 2 mM sodium azide as the equilibration, wash, and elution buffer, and 1 M NaOH in 30% isopropanol as the cleaning-in-place buffer.

Sequences of expressed proteins

MS2 wt
ASNFTQFVLVDNGGTGDVTVAPSNFANGVAEWISSNSRSQAYKVTCSVRQSSAQNR
KYTIKVEVPKVATQTVGGVELPVAAWRSYLNMELTIPIFATNSDCELIVKAMQGLL
KDGNPIPSAIAANSGIY
MS2 N87C
ASNFTQFVLVDNGGTGDVTVAPSNFANGVAEWISSNSRSQAYKVTCSVRQSSAQNR
KYTIKVEVPKVATQTVGGVELPVAAWRSYLCMELTIPIFATNSDCELIVKAMQGLL
KDGNPIPSAIAANSGIY
MS2 T5H/N87C
ASNFHQFVLVDNGGTGDVTVAPSNFANGVAEWISSNSRSQAYKVTCSVRQSSAQNR
KYTIKVEVPKVATQTVGGVELPVAAWRSYLCMELTIPIFATNSDCELIVKAMQGLL
KDGNPIPSAIAANSGIY
MS2 Q6R/N87C
ASNFTRFVLVDNGGTGDVTVAPSNFANGVAEWISSNSRSQAYKVTCSVRQSSAQNR
KYTIKVEVPKVATQTVGGVELPVAAWRSYLCMELTIPIFATNSDCELIVKAMQGLL
KDGNPIPSAIAANSGIY
MS2 N12K/N87C
ASNFTQFVLVDKGGTGDVTVAPSNFANGVAEWISSNSRSQAYKVTCSVRQSSAQNR
KYTIKVEVPKVATQTVGGVELPVAAWRSYLCMELTIPIFATNSDCELIVKAMQGLL
KDGNPIPSAIAANSGIY
MS2 T15H/N87C
ASNFTQFVLVDNGGHGDVTVAPSNFANGVAEWISSNSRSQAYKVTCSVRQSSAQNR
KYTIKVEVPKVATQTVGGVELPVAAWRSYLCMELTIPIFATNSDCELIVKAMQGLL
KDGNPIPSAIAANSGIY
MS2 V67R/N87C
ASNFTQFVLVDNGGTGDVTVAPSNFANGVAEWISSNSRSQAYKVTCSVRQSSAQNR
KYTIKVEVPKRATQTVGGVELPVAAWRSYLCMELTIPIFATNSDCELIVKAMQGLL
KDGNPIPSAIAANSGIY
MS2 T71K/N87C
ASNFTQFVLVDNGGTGDVTVAPSNFANGVAEWISSNSRSQAYKVTCSVRQSSAQNR
KYTIKVEVPKVATQKVGGVELPVAAWRSYLCMELTIPIFATNSDCELIVKAMQGLL
KDGNPIPSAIAANSGIY
MS2 G73R/N87C
ASNFTQFVLVDNGGTGDVTVAPSNFANGVAEWISSNSRSQAYKVTCSVRQSSAQNR
KYTIKVEVPKVATQTVRGVELPVAAWRSYLCMELTIPIFATNSDCELIVKAMQGLL
KDGNPIPSAIAANSGIY
MS2 V67R/T71K/N87C
ASNFTQFVLVDNGGTGDVTVAPSNFANGVAEWISSNSRSQAYKVTCSVRQSSAQNR
KYTIKVEVPKRATQKVGGVELPVAAWRSYLCMELTIPIFATNSDCELIVKAMQGLL
KDGNPIPSAIAANSGIY

MS2 V67R/G73R/N87C
ASNFTQFVLVDNGGTGDVTVAPSNFANGVAEWISSNSRSQAYKVTCSVRQSSAQNR
KYTIKVEVPKRATQTVRGVELPVAAWRSYLCMELTIPIFATNSDCELIVKAMQGLL
KDGNPIPSAIAANSGIY
MS2 T71K/G73R/N87C
ASNFTQFVLVDNGGTGDVTVAPSNFANGVAEWISSNSRSQAYKVTCSVRQSSAQNR
KYTIKVEVPKVATQKVRGVELPVAAWRSYLCMELTIPIFATNSDCELIVKAMQGLL
KDGNPIPSAIAANSGIY
MS2 V67R/T71K/G73R/N87C
ASNFTQFVLVDNGGTGDVTVAPSNFANGVAEWISSNSRSQAYKVTCSVRQSSAQNR
KYTIKVEVPKRATQKVRGVELPVAAWRSYLCMELTIPIFATNSDCELIVKAMQGLL
KDGNPIPSAIAANSGIY
MS2 T71R/N87C
ASNFTQFVLVDNGGTGDVTVAPSNFANGVAEWISSNSRSQAYKVTCSVRQSSAQNR
KYTIKVEVPKVATQRVGGVELPVAAWRSYLCMELTIPIFATNSDCELIVKAMQGLL
KDGNPIPSAIAANSGIY
MS2 G73K/N87C
ASNFTQFVLVDNGGTGDVTVAPSNFANGVAEWISSNSRSQAYKVTCSVRQSSAQNR
KYTIKVEVPKVATQTVKGVELPVAAWRSYLCMELTIPIFATNSDCELIVKAMQGLL
KDGNPIPSAIAANSGIY
MS2 T71R/G73R/N87C
ASNFTQFVLVDNGGTGDVTVAPSNFANGVAEWISSNSRSQAYKVTCSVRQSSAQNR
KYTIKVEVPKVATQRVRGVELPVAAWRSYLCMELTIPIFATNSDCELIVKAMQGLL
KDGNPIPSAIAANSGIY
MS2 T71K/G73K/N87C
ASNFTQFVLVDNGGTGDVTVAPSNFANGVAEWISSNSRSQAYKVTCSVRQSSAQNR
KYTIKVEVPKVATQKVKGVELPVAAWRSYLCMELTIPIFATNSDCELIVKAMQGLL
KDGNPIPSAIAANSGIY
MS2 T71R/G73K/N87C
ASNFTQFVLVDNGGTGDVTVAPSNFANGVAEWISSNSRSQAYKVTCSVRQSSAQNR
KYTIKVEVPKVATQRVKGVELPVAAWRSYLCMELTIPIFATNSDCELIVKAMQGLL
KDGNPIPSAIAANSGIY

Determination of assembly state

The assembly state of each MS2 variant was characterized via HPLC size exclusion chromatography with an Agilent bioSEC-5 column (5 µm, 2000 Å, 7.8x300 mm) with isocratic flow of 10 mM phosphate buffer at pH 7.2 with 2 mM sodium azide. Coelution of A_{260} and A_{280} peaks from 5-8 min are indicative of assembled capsids, while a peak at 10 min corresponds to the elution of unassembled MS2 dimers.

Mass spectrometry

Modified and unmodified MS2 CP variants were analyzed with an Agilent 1260 series liquid chromatograph connected in-line with an Agilent 6530 LC/QTOF mass spectrometer with an electrospray ionization source. The expected mass of each MS2 CP variant was confirmed via QTOF-ESI-MS (Figure 2.3).

Dye modification

All MS2 CP variants containing the N87C mutation (final concentration 10 µM) were mixed with 5 equivalents of either fluorescein-5-maleimide (stock solution 5 mM in DMSO, 50 µM final concentration) in 10 mM phosphate buffer, pH 7.2. The solution was incubated on a rotator at room temperature for 1 h or at 4 °C overnight. Excess dye was removed by three rounds of washes through Amicon Ultra-0.5 mL 100 kDa MWCO filters and two rounds of filtration through Micro-spin™ G-25 columns. Modification of MS2 CP variants was verified via QTOF-ESI-MS and SDS-PAGE (Figures 2.4-2.5). Each MS2 CP variant was modified to 70-90% by monomer with dye, corresponding to 126-162 fluorophores per assembled capsid (Table 2.2). The concentration of each MS2-fluorophore conjugate was normalized to 5 µM for subsequent internalization assays.

Synthesis of MMAE-conjugated MS2 capsids

Samples of each MS2 construct were prepared at 20 µM and combined with 10 equiv. of a stock solution of maleimide-Val-Cit-PAB-MMAE (Broadpharm) in 100 mM phosphate buffer (1% v/v DMSO) pH 7.4, and incubated overnight at 4°C. Excess MMAE was removed via 7 cycles of spin filtration through a 100 kDa MWCO filter (Amicon) and product was analyzed by QTOF-ESI-MS.

Hemolysis assay

A hemolysis assay was performed to measure potential damage to red blood cells by quantifying the release of iron-containing hemoglobin into plasma after incubation with different MS2 CP variants [196]. A Hemoglobin Assay Kit was used according to Sigma Aldrich's instructions to quantify the release of heme from human whole blood after incubation with different MS2 CP variants. Briefly, this assay uses the Triton®/NaOH method in which hemoglobin is converted to a colored product that can be measured by absorbance at 400 nm. Single donor human whole blood containing anti-coagulant was obtained from VWR and stored at 4 °C for up to 48 h. A 1 mL aliquot of blood was centrifuged for 15 min at 800 x *g*. The supernatant was collected and used to determine the amount of plasma-free hemoglobin. Standard curves of whole blood and plasma were prepared to determine the optimal concentration of blood for total blood hemoglobin and plasma blood hemoglobin measurements, respectively. The remaining whole blood was spun down for 10 m at 500 x

g and resuspended in 1x PBS (Ca^{2+}/Mg^{2+}-free) to remove any anticoagulant. This wash step was repeated twice, and the final pellet was diluted in 1x PBS (Ca^{2+}/Mg^{2+}-free) to adjust total hemoglobin concentration to 10 mg/mL. Tubes were prepared with 100 µL of the diluted whole blood, 800 µL Ca^{2+}/Mg^{2+}-free PBS, and 100 µL of MS2 variant stocks to give final treatment concentrations of 0, 0.1, 1, 5, 10, and 20 µM MS2 in a total volume of 1 mL. For comparison with another delivery agent, tubes were also prepared with 100 µL of the diluted whole blood, 800 µL Ca^{2+}/Mg^{2+}-free PBS, and 100 µL of Lipofectamine™ 2000 stocks to give final treatment concentrations of 0.003, 0.006, 0.013, 0.025, and 0.050 mg/mL Lipofectamine™ 2000 in a total volume of 1 mL. The Lipofectamine treatment concentrations were chosen to correspond to the suggested reagent concentration range according to the Thermo Fisher user protocol. A maximum lysis treatment was also prepared with 100 µL diluted whole blood, 800 µL Ca^{2+}/Mg^{2+}-free PBS, and 100 µL of 10x CyQUANT™ Cell Lysis Buffer. The tubes were placed in a 37 °C water bath for 3 h and mixed gently every 30 min. The samples were then centrifuged for 15 min at 800 x *g*. The supernatant was collected, and hemoglobin concentration was measured according to the kit instructions and percent hemolysis was calculated according to the following equation:

$$\% \text{ hemolysis} = \frac{A400_{sample} - A400_{blank}}{A400_{maximum}} * 100 \tag{2.1}$$

LDH cytotoxicity assay

A CyQUANT™ LDH Cytotoxicity Assay Kit was used according to Thermo Fisher's instructions to quantify possible cytotoxicity mediated by different MS2 CP variants. Briefly, lactate dehydrogenase (LDH) is released into cell culture media by damage to the plasma membrane. Extracellular LDH can be measured by an enzymatic reaction where LDH catalyzes the conversion of lactate to pyruvate via NAD^+ reduction to NADH coupled to a colorimetric readout at 490 nm. The optimum HeLa and U-87 MG cell numbers for the LDH assay were determined by plating two sets of serial dilutions of 0-10,000 cells/100µL media in a 96-well plate. After overnight incubation, 10 µL of sterile water was added to each well of one cell dilution series for the Spontaneous LDH Release Control and 10 µL 10x Lysis Buffer was added to the other cell dilution series for the Maximum LDH Release Control and incubated at 37 °C with 5% CO_2 for 45 min. LDH activity was measured according to the kit instructions and the linear range of the assay for HeLa and U-87 MG cells was determined (Figure 2.10). The optimal number of cells (4,000/well) were plated with 100 µL media in triplicate wells a 96-well plate and incubated overnight at 37 °C with 5% CO_2. A combination of 10 µL of sterile water, 10 µL Lysis Buffer, and 10 µL of 1, 5, 10, or 20 µM MS2 were each added to one set of triplicate wells. The resulting samples were incubated at 37 °C with 5% CO_2 for 45 min. LDH activity was measured according to the kit instructions and the percent cytotoxicity for each MS2 treatment concentration was calculated using the following formula:

$$\% \text{ cytotoxicity} = \frac{A490_{sample} - A490_{spont.}}{A490_{max} - A490_{spont.}} \tag{2.2}$$

MTS cell viability assay

An MTS Assay Kit (ab197010) was used according to Abcam's instructions to quantify cell viability after treatment with different MS2 CP variants. Briefly, an MTS tetrazolium compound is reduced by viable mammalian cells to generate a colored formazan dye that can be measured by absorbance at 490 nm. HeLa and U-87 MG cells were plated into a 96-well plate at a concentration of 5,000 cells per well in 100 µL DMEM + FBS and incubated overnight at 37 °C with 5% CO_2. The next day, media was aspirated and replaced with 100 µL of either 0, 1, 5, 10, 20, or 40 µM MS2 diluted in DMEM + FBS and incubated for 24, 48, or 72 h at 37 °C with 5% CO_2. Then, the treatment media was aspirated and 100 µL DMEM + 20% MTS reagent was added to each well and incubated for 1 h at 37 °C with 5% CO_2 before measuring the absorbance at 490 nm. Cell viability was calculated as an absorbance percentage over the untreated control:

$$\% \text{ viability} = 100 * \frac{A490 \; treated \; cells}{A490 \; control \; cells} \tag{2.3}$$

MS2-MMAE MTS cell viability assay

U-87 MG cells were plated in a 96-well plate at 4,000 cells/well and allowed to adhere overnight. Cells were then incubated for 72 h at 37 °C with 80 µL DMEM + 10% FBS and 20 µL MS2-MMAE or vehicle control at appropriate concentrations in DPBS. Media were then aspirated and replaced with 200 µL pre-warmed DMEM without phenol red or FBS along with 20 µL Abcam MTS Cell Proliferation Assay solution. Samples were then incubated in the dark for 1 h and immediately analyzed for optical density at 490 nm. Cell viability was calculated as an absorbance percentage over the untreated control:

$$\% \text{ viability} = 100 * \frac{A490 \; treated \; cells}{A490 \; control \; cells} \tag{2.4}$$

Mammalian cell culture

HeLa, Saos-2, HEK293T, and U-87 MG cells were cultured in DMEM supplemented with 10% fetal bovine serum (FBS), 4.5 g/L glucose, 4 mM L-glutamine, and 1 mM sodium pyruvate. All cell cultures were maintained at 37 °C in a humidified atmosphere with 5% CO_2.

Epifluorescence microscopy

25,000 HeLa cells were plated in each well of a 96-well plate and incubated overnight at 37 °C with 5% CO_2. Cells were washed three times with DPBS and treated with 5 µM MS2-fluorescein in DPBS with 1% FBS for 1 h at 37 °C with 5% CO_2. After incubation, cells were washed three times with 20 U/mL heparin in DPBS to remove positively charged surface-bound species. Cells were fixed with 2% paraformaldehyde and 0.1 µg/mL DAPI and kept at 4 °C until imaging. Cells were imaged on an Image Xpress Micro fluorescent microscope.

Flow cytometry

200,000 HeLa cells were plated in each well of a 24-well plate and incubated overnight at 37 °C with 5% CO_2. Cells were washed three times with DPBS and treated with 5 µM MS2-fluorescein in DPBS with 1% FBS for 1 h at 37 °C with 5% CO_2. After incubation, cells were washed three times with 20 U/mL heparin in DPBS to remove positively charged surface-bound species. Cells were lifted with trypsin, quenched with FBS-containing DMEM and pelleted at 200 g for 3 min. Cells were washed twice with DPBS and resuspended in 1 mL DPBS. Cells were pelleted at 200 g for 3 min and resuspended in 1 mL 2% paraformaldehyde with 0.1 µg/mL DAPI and kept at 4 °C until flow cytometry. Flow cytometry was completed using an Attune NxT flow cytometer. At least 10,000 cells were analyzed for each sample. Data were analyzed using FlowJo and the mean fluorescence values with coefficient of variation were reported (Table 2.3). Fluorescence intensity values were corrected according to the % fluorescein-maleimide modification of each MS2 CP variant (Table 2.3).

Flow cytometry for multiple cell types screen

HeLa, Saos-2, HEK293T, and U-87 MG cells were plated at 60% confluence in each well of a 12-well plate and incubated overnight 37 °C with 5% CO_2. Cells were washed three times with DPBS and treated with 5 µM MS2-fluorescein in DPBS with 1% FBS for 1 h at 37 °C with 5% CO_2. Cells were lifted with trypsin, quenched with FBS-containing DMEM and pelleted at 200 g for 3 min. Cells were washed twice with DPBS and resuspended in 1 mL DPBS. Cells were pelleted at 200 g for 3 min and resuspended in 1 mL 2% paraformaldehyde with 0.1 µg/mL DAPI and kept at 4 °C until flow cytometry. Flow cytometry was completed using an Attune NxT flow cytometer. At least 10,000 cells were analyzed for each sample. Data were analyzed using FlowJo and the mean fluorescence values with coefficient of variation were reported (Table 2.4).

Endocytosis inhibitor screen

50,000 cells/well were plated in fibronectin-coated 8-well Nunc™ LabTek™ I Chambered Coverglass slides and 200,000 cells/well were plated in 24-well plates and incubated over-

night at 37 °C with 5% CO_2. Cells were washed three times with DPBS and treated with either 10 U/mL heparin, 5 µM cytochalasin D, 80 µM dynasore, 20 µM taxol, or 5 mM methyl-β-cyclodextrin in DPBS with 1% FBS for 30 min at 37 °C with 5% CO_2. Separate plates of cells were incubated with DPBS with 1% FBS at 4 °C for 30 min. Cells were washed with DPBS and treated with 5 µM MS2-fluorescein in DPBS with 1% FBS for 1 h at 37 °C with 5% CO_2 and either 10 U/mL heparin, 5 µM cytochalasin D, 80 µM dynasore, 20 µM taxol, or 5 mM methyl-β-cyclodextrin. Separate plates of cells were incubated with 5µM MS2-fluorescein in DPBS with 1% FBS at 4 °C for 1 h. After incubation, cells were washed three times with 20 U/mL heparin in DPBS to remove positively charged surface-bound species. Cells in the 8-well microscopy slides were fixed with 2% paraformaldehyde and 0.1 µg/mL DAPI and kept at 4 °C until imaging. Cells were imaged on a Zeiss LSM 880 confocal microscope. Cells in the 24-well plates were lifted with trypsin, quenched with FBS-containing DMEM and pelleted at 200 g for 3 min. Cells were washed twice with DPBS and resuspended in 1 mL 2% paraformaldehyde with 0.1 µg/mL DAPI and kept at 4 °C until flow cytometry. Flow cytometry was completed using an Attune NxT flow cytometer. At least 10,000 cells were analyzed for each sample. Data were analyzed using FlowJo and the median fluorescence values with coefficient of variation were reported (Table 2.7).

Molecular mechanics calculations

An assembly of 12 wtMS2 coat protein dimers (i.e. 24 MS2 monomers in total) was generated around the 3-fold axis of symmetry (PDB ID: 2MS2). An assembly of 10 wtMS2 dimers (20 monomer proteins in total) surrounding the 5-fold axis of symmetry was prepared in the same manner. The PyMOL mutagenesis wizard tool was used to create all MS2 CP variants. The structures were imported into Schrödinger's Maestro suite (version 2021-2) and the structures were preprocessed with Maestro's protein preparation wizard. Hydrogen bonds were assigned with the H-bond optimization tool at a PROPKA pH of 7. Then, a restrained minimization of the structure using the OPLS4 forcefield was performed. MacroModel was used to run a Large-scale Low Mode conformational search of the minimized structures. All residues within 10 Å of the mutations were allowed to move freely. All residues between 10 Å and 20 Å of the mutations were restrained with a force constant of 200 kJ/mol. All atoms beyond these subshells were frozen in place. Sampling used 1000 maximum steps with 100 steps per 100 rotatable bond. The top five output structures for each variant were compared to confirm similar conformations for the mutated residues.

Isoelectric point and pK_a calculations

The sequence-based isoelectric points of wt MS2, MS2 T71K/G73R, and MS2 T71R/G73K were calculated using the Expasy Compute pI/MW tool and the Isoelectric Point Calculator 2.0 tool (Table 2.5) [197, 198]. Structure-based isoelectric points of wt MS2, MS2 T71K/G73R, and MS2 T71R/G73K were calculated from the output structures of the described Macro-Model molecular mechanics simulations. The protein titration curve tool in

Mutation	5-fold conformation	6-fold conformation
T71K	capsid exterior	capsid exterior
G73R	capsid exterior	capsid interior
T71R	capsid exterior	capsid exterior
G73K	capsid exterior	capsid interior
T71K/G73R	T71K: capsid exterior, G73R: capsid exterior	T71K: capsid exterior, G73R: capsid interior
T71R/G73K	T71R: capsid exterior, G73K: capsid exterior	T71R: capsid exterior, G73K: capsid interior
T71R/G73R	T71R: capsid exterior, G73R: capsid exterior	T71R: capsid exterior, G73R: capsid interior
T71K/G73K	T71K: capsid exterior, G73K: capsid exterior	T71K: capsid exterior, G73K: capsid interior

Table 2.11: Conformations of cationic amino acids at positions 71 and 73 of MS2 CP.

Maestro was used to determine the isoelectric point of the 10mer and 12mer structures of each variant and the PROPKA pK_as of each residue at positions 71 and 73 (Table 2.6, Figure 2.9) [180].

Dynamic light scattering (DLS) size measurements

MS2 samples were prepared by diluting to 50 µM in 10 mM sodium phosphate, pH 7.2, and passing through a 0.2 µM centrifugal filter. The filtered samples were added to a DLS cuvette and 25 °C was used for room temperature analysis. Size measurements were taken in triplicate sets of 13 runs each. The diameter and standard deviation for each MS2 CP variant was calculated from an average of the %Volume mean from each run.

DLS temperature-dependent size measurements

MS2 samples were prepared by diluting to 50 µM in 10 mM sodium phosphate, pH 7.2, and passing through a 0.2 µM centrifugal filter. The filtered samples were added to a DLS cuvette and measurements were taken with increasing temperature from 25 to 75 °C at 5 °C intervals. The diameter and standard deviation for each MS2 CP variant was calculated from an average of the %Volume mean from each run.

DLS zeta potential measurements

MS2 samples were prepared by diluting to 50 µM in 10 mM sodium phosphate, pH 7.2, and passing through a 0.2 µM centrifugal filter. The filtered samples were added to a Malvern DTS1070 Folded Capillary Cell and 25 °C was used for room temperature analysis. Zeta potential measurements were taken in triplicate sets of 100 runs each. The zeta potential average and standard deviation for each MS2 CP variant was reported in mV.

2.7 Acknowledgements

This work was supported by the Panattoni Family Fund. Computational studies in this work were completed with support from the UC Berkeley MGCF and NIH S10OD023532. We are grateful to M. West, manager at the QB3 CTAF, for microscopy and flow cytometry training, and D. Schichnes at the UC Berkeley BIF for confocal microscopy training.

Chapter 3

Exploring the effects of intersubunit interface mutations on virus-like particle structure and stability

3.1 Abstract

Virus-like particles (VLPs) from bacteriophage MS2 provide a platform to study protein self-assembly and create engineered systems for drug delivery. Here, we aim to understand the impact of intersubunit interface mutations on the local and global structure and function of MS2-based VLPs. In previous work, our lab identified locally supercharged double mutants [T71K/G73R] that concentrate positive charge at capsid pores, enhancing uptake into mammalian cells. To study the effects of particle size on cellular internalization, we combined these double mutants with a single point mutation [S37P] that was previously reported to switch particle geometry from $T = 3$ to $T = 1$ icosahedral symmetry. These new variants retained their enhanced cellular uptake activity and were able to deliver small-molecule drugs with efficacy levels similar to our first-generation capsids. Surprisingly, these engineered triple mutants exhibit increased thermostability and unexpected geometry, producing $T = 3$ particles instead of the anticipated $T = 1$ assemblies. Transmission electron microscopy revealed various capsid assembly states, including wild-type ($T = 3$), $T = 1$, and rod-like particles, that could be accessed using different combinations of these point mutations. Molecular dynamics experiments recapitulated the structural rationale in silico for the single point mutation [S37P] forming a $T = 1$ virus-like particle and showed that this assembly state was not favored when combined with mutations that favor rod-like architectures. Through this work, we were able to investigate how interdimer interface dynamics influence VLP size and morphology and how these properties affect particle function in applications such as drug delivery.[1]

[1]Portions of this chapter are reprinted with permission from Pistono, P. E.; Xu, J.; Huang, P.; Fetzer, J.L.; Francis, M. B. Exploring the Effects of Intersubunit Interface Mutations on Virus-Like Particle Structure

3.2 Introduction

Understanding the fundamental governing interactions present in protein self-assembly is important because many biological functions are performed by proteins in the form of supramolecular complexes. Here, we discuss the engineering of a virus-like particle (VLP) to produce hollow protein shells with varying sizes, stabilities, and biological functions. VLPs are useful nanoparticles for the study of self-assembly and for the encapsulation and delivery of bioactive molecules, often enhancing their activity. VLPs are promising materials for use in drug delivery that (1) can be produced inexpensively by recombinant expression, (2) are homogenous in size, and (3) are easily degraded in the body [155, 156]. Self-assembling protein materials can be genetically engineered and chemically modified with new functionalities using site-selective bioconjugation reactions [50, 79, 199–201]. The functional organizations of many virus-like particles are in the form of icosahedra whose assembly geometries are governed by genetic economy and quasi-equivalence. Thus, a viral genome favors symmetric architectures with reduced coding cost, and many copies of a single protein monomer can adopt locally equivalent positions in a capsid; this allows viruses with larger sizes to form from increased numbers of building blocks [3, 4].

Several studies have found that VLP mutations can alter these assembly states, yielding particles with distinct or mixed assembly geometries. For example, Qβ VLPs possess natural variation in assembly geometry, ranging from prolate to $T = 4$ particles are made along with infectious $T = 3$ virions [39]. It has also been shown that MS2 VLPs can naturally form a mix of $T = 3$ and $T = 4$ structures, but many of these alternative assembly states are non-infectious in phage form because they do not possess the standard maturation protein incorporation site [40]. The sizes and shapes of various icosahedral VLPs can also be disrupted via loop insertion mutations, resulting in diverse forms of particles, including rod-like structures [41, 202, 203].

MS2 is a well-studied bacteriophage that assembles into 27 nm, $T = 3$ icosahedral particles made up of 180 identical monomers, which are folded into asymmetric A/B dimers and symmetric C/C dimers [164]. This conformational change occurs upon binding of genetic material to the dimer interior and allows for the formation of a $T = 3$ capsid with 5-fold, 3-fold (quasi 6-fold), and 2-fold assembly interfaces. Coincidence with the 3-fold axes are hexameric interfaces with alternating sets of A/B and C/C dimers, while the 5-fold axes are made up of five sets of A/B dimers. MS2 can be recombinantly expressed and deep mutational scanning techniques have been developed to characterize how individual amino acid mutations affect its assembly properties [151]. Studies have identified capsid variants with high assembly competency, thermostability, acid-sensitivity, chemical modifiability, cell permeability, and mutations that alter particle size [49–53, 151].

In our recent study, we used the nanoscale assembly of MS2-based VLPs to create locally supercharged variants, thus enhancing their uptake into mammalian cells [152]. Two key double mutants were identified that concentrated positive charge at capsid pores. The low

and Stability. *Submitted manuscript* 2024.

cytotoxic and low hemolytic activity of these variants, as well as their ability to internalize into multiple cell types, add to their promise as potential drug delivery vehicles. While these capsids were found to be stable in initial experiments, we noted that losses in stability over long-term storage periods occurred.

Work in the Tullman-Ercek lab previously identified MS2 S37P as a size-reducing mutation that mediates a switch in particle geometry from the native $T = 3$ capsid to a smaller, 17 nm $T = 1$ capsid comprising 60 symmetrically identical monomers (Figure 3.1) [52]. From structural data, they hypothesized that hydrogen bonding interactions between N36 and N98 were more favored in the MS2 S37P capsid, favoring stability at the 5-fold interface and therefore creating a smaller particle (Figure 3.1). Further work to identify self-assembly rules for shifting MS2 particle size showed that the identity of both residues 36 and 37 were important for miniMS2 formation, and this design rule was applied to create smaller particles in MS2 homolog Qβ [54].

MS2 S37P (herein referred to as 'miniMS2') could serve as a valuable tool to study the effects of particle size on cellular uptake. Moreover, we reasoned that the S37P mutation could be used to determine if the previously identified uptake-enhancing mutations at positions 71 and 73 would work for particles of difference sizes. We observed that there is a delicate balance that governs particle assembly when combining mutations that favor stability at the 5-fold versus 6-fold assembly interfaces. Here we report the discovery that certain mutations at the FG loop disrupt $T = 3$ icosahedron assembly and result in the formation of rod-like structures that are presumed to be comprised exclusively of 6-fold assembly interfaces. When combined with the 5-fold-favoring S37P mutation, we see a shift in particle assembly state back to $T = 3$, but do not observe the anticipated $T = 1$ particles. We additionally found that these combined mutations were exceptionally effective at delivering charged cargo into mammalian cells. Moreover, the combination of these mutations resulted in particles with highly increased thermostability compared to the original locally supercharged double mutants.

3.3 Results and Discussion

Intersubunit interface mutations control MS2 particle structure and stability in unanticipated ways

In order to explore the effect of quaternary structure on the cellular uptake and stability properties of MS2 VLPs, we generated locally supercharged MS2 variants with all possible combinations of arginine and lysine at CP positions 71 and 73, with fixed S37P and N87C backbone point mutations. The specific mutants that were evaluated are listed in Figure 3.3. The MS2[S37P] mutation was expected to shift the MS2 VLP assembly from a 27 nm, $T = 3$ icosahedron with 180 monomers to a 17 nm, $T = 1$ icosahedron with 60 monomers, with an interior cysteine [N87C] for bioconjugation [52]. All nine MS2[S37P/N87C] variants were expressed and the assembly state of each variant was assessed via size exclusion

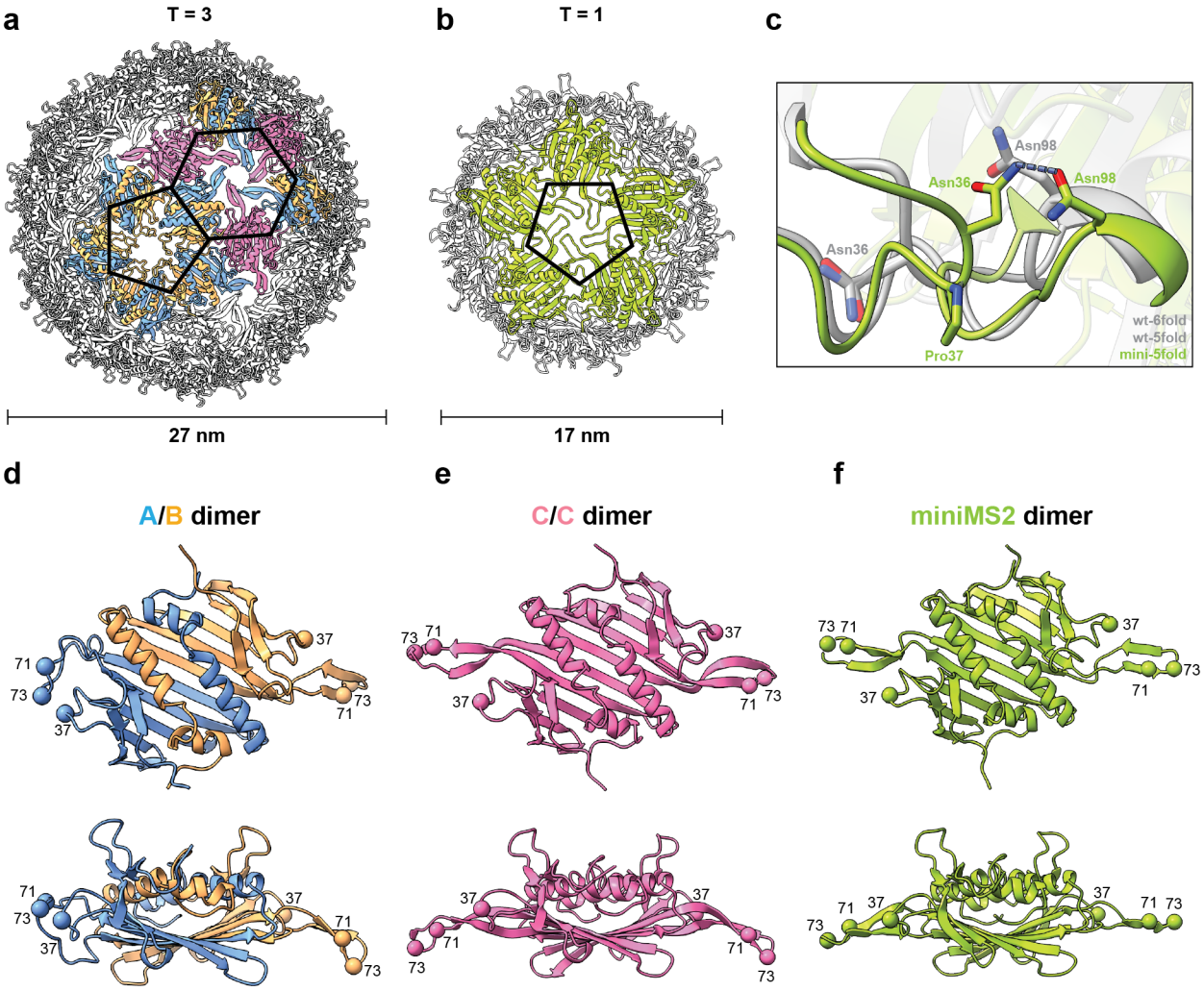


Figure 3.1: **(A)** Structure of wild-type MS2 capsid (PDB ID: 2MS2), shown, with A/B dimers (blue & yellow) and C/C dimers (pink) labeled. Five sets of A/B dimers assemble at the 5-fold interface (black pentagon), and three sets of A/B dimers alternating with three sets of C/C dimers assemble at the 6-fold interface (black hexagon). **(B)** Structure of the MS2[S37P], or "miniMS2" capsid (PDB ID: 4ZOR) shown, with dimers labeled in green. Five sets of dimers assemble at the 5-fold interface (black pentagon). **(C)** Interdimer interface interactions between residues Asn36 and Asn98 at the MS2 assembly interfaces are shown. The miniMS2 structure (green) is overlaid on the wtMS2 structures (grey). A key H-bonding interaction between the Asn36 side chain nitrogen and the Asn98 side chain oxygen at the miniMS2 interdimer interface is drawn as a blue dashed line. **(D)**, **(E)**, **(F)** Top and side views of the wtMS2 A/B dimer (blue & yellow), wtMS2 C/C dimer (pink), and miniMS2 dimer (green), respectively, with residues 37, 71, & 73 labeled as spheres.

chromatography (Figure 3.3). All MS2[S37P/N87C] variants produced assembled capsids, and the elution times of MS2[S37P/N87C] variants with single mutations at position 71 corresponded to the expected 17 nm, $T = 1$ miniMS2 capsids.

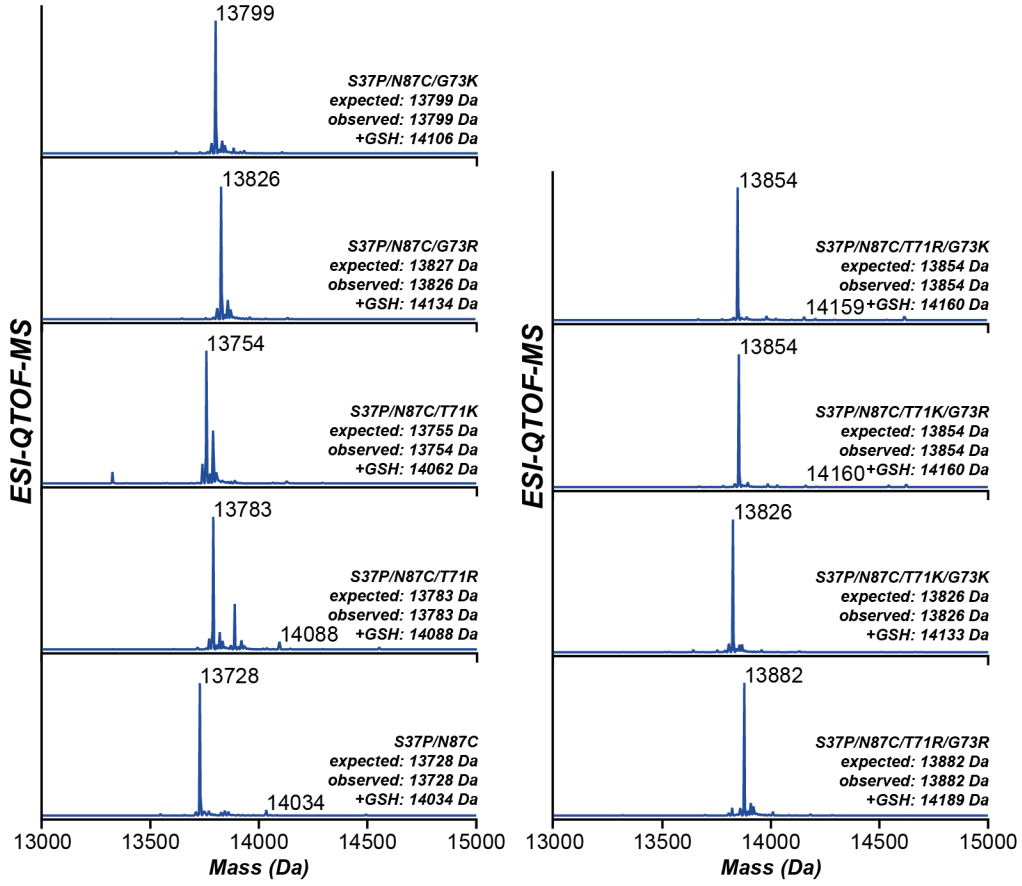


Figure 3.2: LC-QTOF-MS analysis of S37P/N87C MS2 CP variants.

In contrast, the elution times of MS2[S37P/N87C] variants with single mutations at position 73 or double mutations at position 71 and 73 corresponded to 27 nm, $T = 3$ capsids. These unexpected results were further confirmed via transmission electron microscopy (TEM). Images of each MS2 [S37P/N87C] CP mutant showed uniformly-sized VLP populations, while TEM images of each MS2[N87C] mutant revealed the presence of extended rod-like structures with varying lengths and uniform 23.36 ± 2.56 nm diameters in addition to spherical $T = 3$ capsids in MS2[N87C] (Figure 3.4). This was observed for all four samples with mutations at both position 71 and position 73. Upon further analysis, we found that the presence of rod-like structures were not present in TEM images of freshly purified samples that were filtered and frozen before TEM grid preparation and imaging. However, rod-like structures were seen in images of freshly expressed, unfiltered *E. coli* cell lysate and in freshly purified, unfiltered MS2[N87C] double mutant capsids that were maintained at 4

°C over a period of several days. Thus, the best 71K/73R and 71R/73K capsid mutants for cell uptake, which were identified in our previous studies, exhibited an assembly instability that can be rescued by the addition of the S37P mutation while maintaining the overall capsid size.

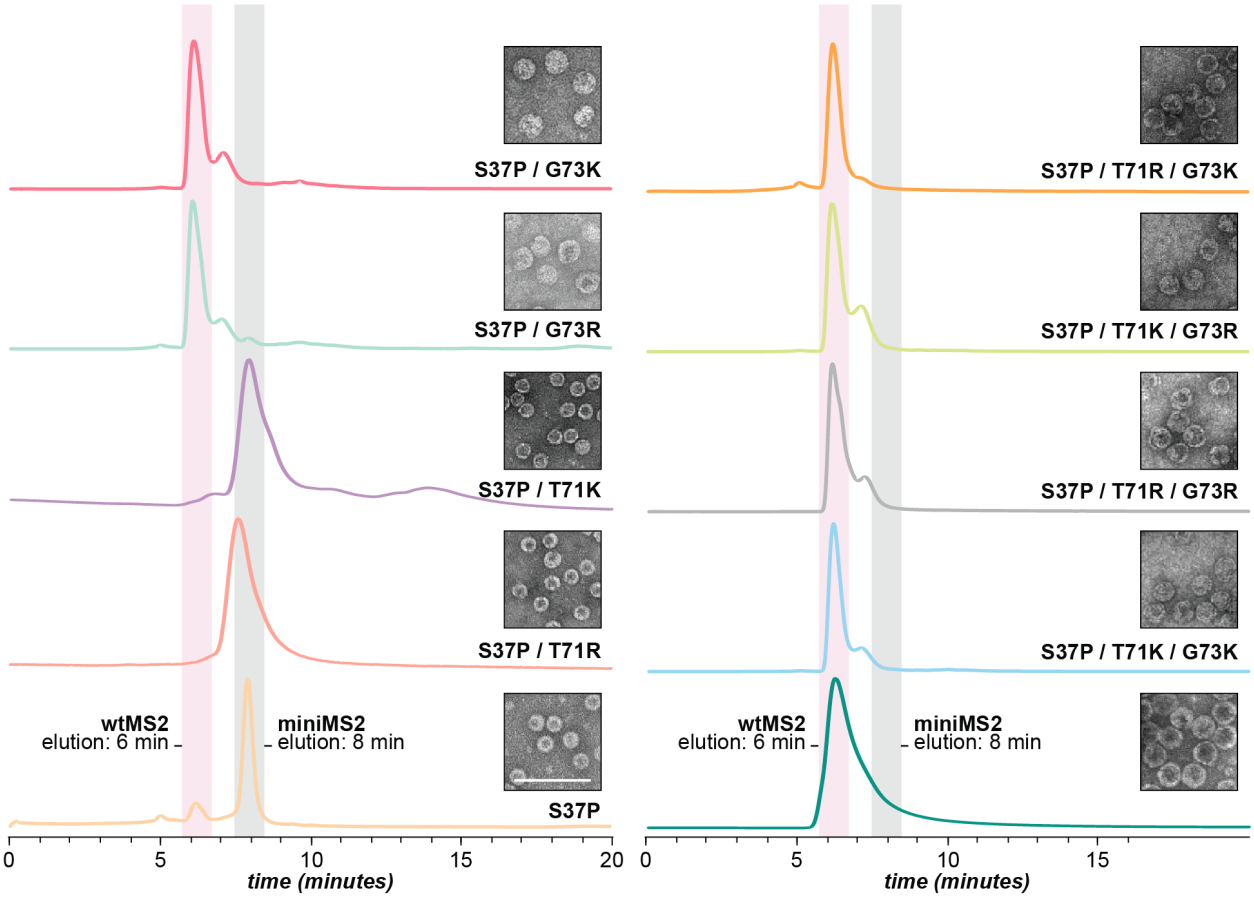


Figure 3.3: HPLC SEC tryptophan fluorescence chromatograms of MS2 CP variants. Highlighted in pink is the expected elution time of assembled $T = 3$ capsids (6 min) and highlighted in grey is the expected elution time of assembled $T = 1$ capsids (8 min). All S37P variants also contain the N87C mutation. Shown as an inset on the right side of each chromatogram is a representative transmission electron microscopy (TEM) image of each MS2 CP variant. The scale bar on the S37P image measures 100 nm.

We assign the rod-like structures to a non-length-controlled propagation of the 6-fold assembly interface. The presence of a mixed population of rod-like structures and $T = 3$ spheres in the MS2[N87C] double mutant samples suggests that the [T71K/G73R] mutation may destabilize interdimer interactions at the 5-fold assembly interface and/or produce favorable interactions at the 6-fold assembly interface. Disruption of assembly interface interactions through mutations such as loop insertions has been shown to produce mixed rod-like and spherical particles in Qβ VLPs via substitution of residues 76 to 81 in the FG loop [202].

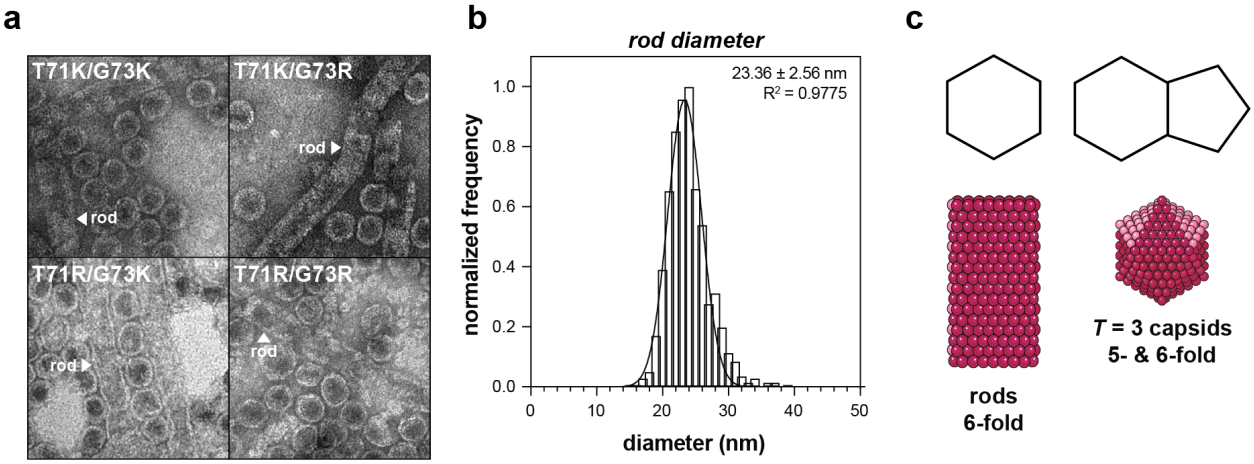


Figure 3.4: **(A)** TEM images of each MS2[N87C] double mutant showing a mixed population of rods and $T = 3$ particles. **(B)** The normalized frequency distribution of the measured MS2 rod diameters, reported as mean diameter ± one standard deviation. The data were fitted to a Gaussian distribution and the R^2 value is reported. **(C)** Diagrams showing the assembly geometries of a rod-shaped particle (left) made of only 6-fold assembly interfaces, and a $T = 3$ capsid (right) made of 5- & 6-fold assembly interfaces.

Although the assembly of Qβ differs from that of MS2 by the presence of four disulfide bonds between residues 74 and 80, residues 76 to 81 in Qβ are analogous to residues 71 to 76 of MS2, where the FG loops converge at the 5-fold and 6-fold interfaces. The assembly of mixed rod-like and spherical particles has also been shown when reassembling mixtures of coat protein dimers *in vitro* from different RNA phages such as MS2, fr, and GA [204].

Thermal shift assay results also provide evidence that the [N87C] double mutants are less stable than their [S37P/N87C] counterparts. The melting point (T_m) of wtMS2 has been reported to be 66 °C. While MS2[S37P] has a similar stability, melting point assays also reported a second T_m of 77 °C, indicating a two-stage melting curve for miniMS2 capsids [52, 177]. We assign the lower T_m to capsid disassembly and the higher T_m to monomer unfolding. Using a Sypro Orange thermal shift assay, we measured the T_m of MS2[N87C] and MS2[S37P/N87C] as well as each variant with single and double mutations at positions 71 and 73 (Figure 3.6, Figure 3.17). The T_m trend for each MS2[N87C] double mutant matched our previously reported results in a dynamic light scattering (DLS)-based thermal shift assay, with T_m values ranging from 42 °C to 49 °C. This indicates that the addition of the cationic residues reduces stability compared to wtMS2. This aligns more closely with the hypothesis that the cationic residues destabilize the 5-fold axes relative to wtMS2.

The T_m values for each MS2[S37P/N87C] double mutant ranged from 53 °C to 59 °C, indicating particles with increased thermal stability compared to their [N87C] counterparts. For the MS2[S37P/N87C] single mutants, the measured T_m values ranged from 53 °C to 61 °C, with three of the four variants possessing a curve with a second T_m from 74 °C to 76 °C. These data confirm that the S37P mutation compensates for the loss in assembly

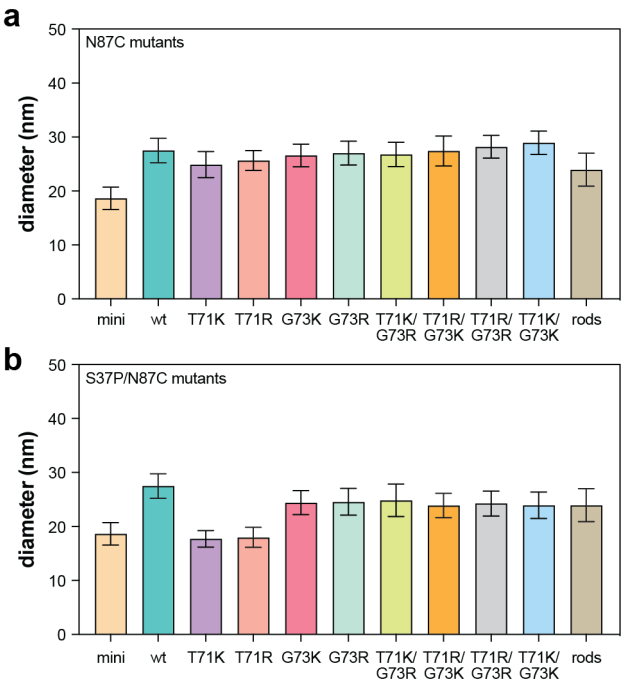


Figure 3.5: **(A)** Bar graphs showing mean diameter of MS2[N87C] variants as measured via TEM images. Scale bars show one standard deviation. **(B)** Bar graphs showing mean diameter of MS2[S37P/N87C] variants as measured via TEM images. Scale bars show one standard deviation.

MS2 Variant	Mean Diameter (nm)	Standard Deviation (nm)	No. Particles Measured	Gaussian Fit R^2
N87C	27.51	2.26	985	0.9969
S37P/N87C	18.37	1.70	1446	0.9900
S37P/T71R	17.70	1.29	1386	0.9956
S37P/T71K	17.66	1.30	1911	0.9970
S37P/G73R	24.49	2.35	1075	0.9911
S37P/G73K	24.33	2.11	1036	0.9956
T71R	25.59	1.78	1417	0.9955
T71K	25.17	2.22	1224	0.9863
G73R	26.92	2.10	1018	0.9972
G73K	26.50	2.03	1028	0.9925
S37P/T71K/G73R	24.78	2.69	1370	0.9854
S37P/T71R/G73K	23.82	2.06	1091	0.9930
S37P/T71R/G73R	24.16	2.15	1025	0.9955
S37P/T71K/G73K	23.83	2.30	1209	0.9935
T71K/G73R	26.67	2.20	1908	0.9964
T71R/G73K	27.20	2.61	1569	0.9882
T71R/G73R	28.05	1.94	2344	0.9957
T71K/G73K	28.63	1.99	987	0.9881
rods	23.36	2.56	904	0.9775

Table 3.1: Mean diameters of MS2 variants as measured via TEM images. All listed MS2 variants also have the N87C mutation.

stability caused by the cationic mutations discussed above. They also suggest that the original observation that [S37P] MS2 forms $T = 1$ capsids may be due to ability of the mutation to increase the stability of the 5-fold interfaces, making them the sole pattern that occurs in these capsids.

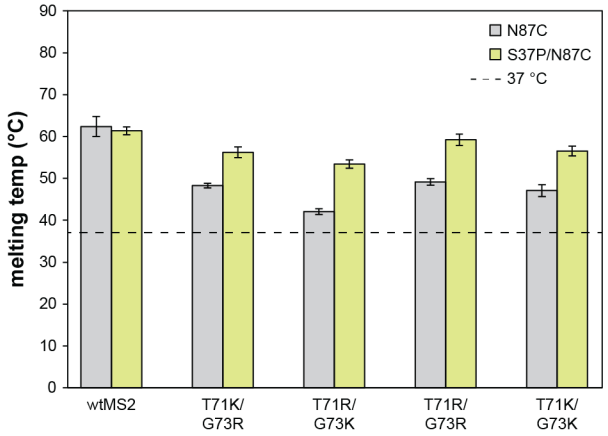


Figure 3.6: (A) Bar graphs showing the mean melting temperature (T_m) of each MS2 variant in degrees Celsius (°C). Error bars shown one standard deviation. The measurements for the [N87C] and [S37P/N87C] versions of each MS2 variant are shown in grey and green, respectively. Physiologically relevant temperature (37 °C) is marked as a dashed line.

MS2 Variant	T_m1 (°C)	T_m1 sd (°C)	T_m2 (°C)	T_m2 sd (°C)
N87C	62.37	2.40	-	-
T71K/G73R/N87C	48.27	0.59	-	-
T71R/G73K/N87C	42.08	0.67	-	-
T71R/G73R/N87C	49.13	0.76	-	-
T71K/G73K/N87C	47.07	1.40	-	-
S37P/T71K/N87C	60.75	2.89	76.00	4.55
S37P/T71R/N87C	61.22	2.77	74.00	0.00
S37P/G73K/N87C	53.29	1.12	75.26	4.02
S37P/G73R/N87C	58.58	2.05	-	-
S37P/T71K/G73K/N87C	56.54	1.15	-	-
S37P/T71K/G73R/N87C	56.25	1.29	-	-
S37P/T71R/G73K/N87C	53.45	0.98	-	-
S37P/T71R/G73R/N87C	59.22	1.39	-	-
S37P/N87C	61.38	0.96	77.15	1.70

Table 3.2: Melting points (T_m) of MS2 variants measured via Sypro Orange thermal shift assay.

Molecular dynamics simulations provide insight into particle interface interactions

To identify the possible structural and conformational changes that yield MS2[S37P/N87C] capsids with unexpected $T = 3$ architectures, a series of MS2 capsid variants was modeled *in silico*. MS2 variants with different combinations of mutations (wt, S37P, T71K/G73R, and S37P/T71K/G7R), were introduced into three geometrically and conformationally distinct starting structures based on wtMS2 coat protein dimers (CP2) at the 6-fold assembly interface (2MS2-6CP2, starting from PDB ID: 2MS2) and 10 sets of wtMS2 CP dimers assembled at the 5-fold interface (10CP2, also from PDB ID: 2MS2) (Figure 3.7). The same set of mutations was also introduced into 10 sets of coat protein dimers of miniMS2 assembled at the 5-fold interface (4ZOR-10CP2, from PDB ID: 4ZOR) (Figure 3.7). As noted in Figure 3.7, miniMS2 lacks 6-fold interfaces.

Previous structural studies of $T = 1$ miniMS2 capsids revealed a key decrease in the interdimer angles due to differences in hydrogen bonding at the dimer-dimer interface [52]. A switch to the *cis*-amide conformation of Pro37 alters the configuration of neighboring residues, creating a new hydrogen-bonding interaction between the side-chain nitrogen of Asn36 and the side-chain oxygen of Asn98. This decreases the interdimer contact angle, leading to greater local curvature and ultimately a smaller capsid size [52].

Through molecular dynamics simulations, we were able to recapitulate these differences in hydrogen bonding. By comparing hydrogen bonding contacts between Asn36 and Asn98 over each 100 ns trajectory, we observed substantial differences in the numbers and types of contacts for input structures with different mutations. Trajectories with the miniMS2 (10CP2-4ZOR) input structure had high (>49%) N98side:N36side H-bonding occupancy. In contrast, trajectories with the wtMS2 5-fold input structure (10CP2-2MS2) displayed no N98side:N36side interactions; instead, these structures exhibited a low to moderate (4 to 10%) N98backbone:N36side occupancy that was also present in the miniMS2 simulations (6%) (Figure 3.8). Lower amounts of H-bonding contacts between N98side:N36side were observed in trajectories with the 6-fold input structure (6CP2-2MS2) versus trajectories with the 5-fold input structure (10CP2-2MS2) when comparing the same sets of mutations (Figure 3.9). These *in silico* data support the previously reported structural hypothesis that a new hydrogen-bonding interaction between the side chains of N36 and N98 plays a major role in decreasing the interdimer contact angle, favoring a smaller, $T = 1$ capsid assembly [52]. We also measured the difference in the N98side:N36side when comparing 10CP2 input structures with *cis* versus *trans* proline at position 37 (Figure 3.9). Trajectories with *cis* proline all had high % occupancy (47-50%), while trajectories with *trans* proline all had low or zero % occupancy (0-6%), suggesting that the conformation of proline at position 37 is an important factor in the stability of the 5-fold assembly interface (Figure 3.9).

The interdimer contact angles were also measured over the course of each trajectory. The centers of mass of the neighboring residues 36 and 98 were calculated and a vector was drawn to represent the axis between the residues in each neighboring dimer. Then, the angle between the two vectors over each trajectory was calculated and plotted. Similar to

the H-bonding occupancy results, comparing the angles measured in 10CP2 structures with *cis* versus *trans* proline at position 37 resulted in a notable difference. Trajectories with *cis* proline at position 37 all had lower dimer interface angles (6°), while trajectories with *trans* proline all had higher dimer interface angles (12° to 14°) (Figure 3.9). Assuming that Pro37 in a $T = 1$ icosahedron occupies a *cis* conformation, while Pro37 in a $T = 3$ icosahedron occupies a trans conformation, then these data align with the hypothesis that the interdimer angle in a $T = 1$ icosahedral structure will be smaller than the same angle measured in a $T = 3$ icosahedral structure.

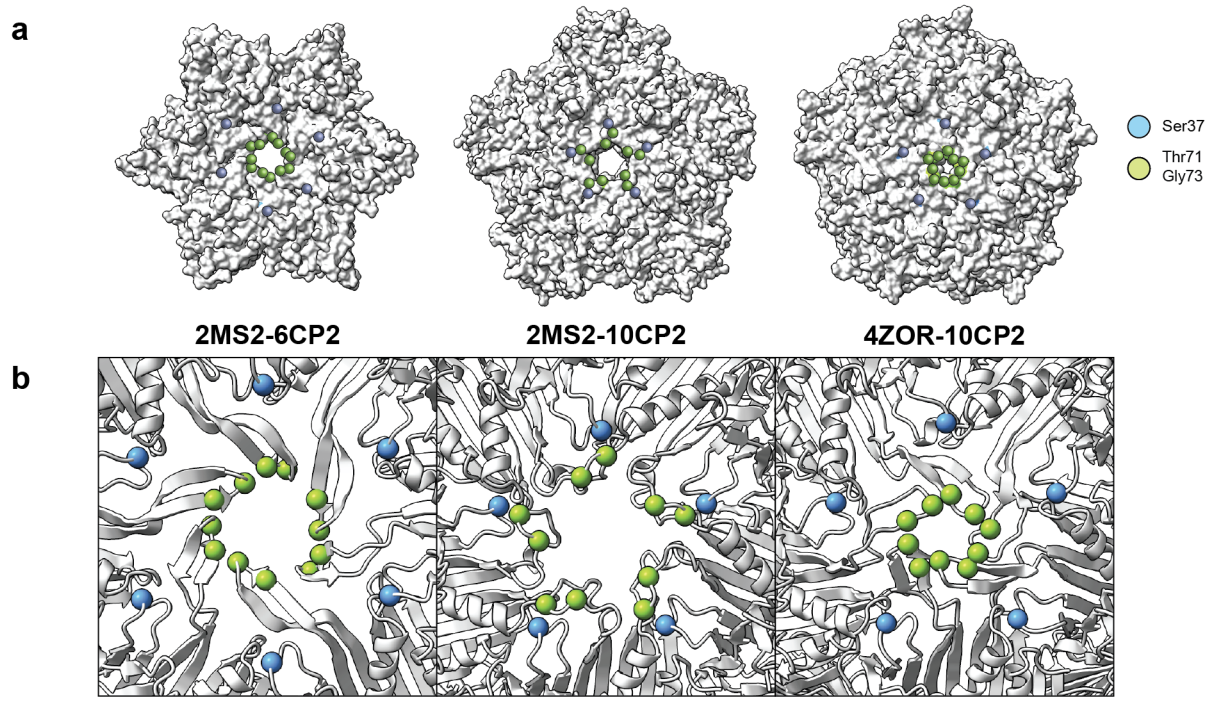


Figure 3.7: **(A)** Input structures for molecular dynamics simulations represent the minimal assembly intermediates at the 5-fold and 6-fold inter-faces for wtMS2 and miniMS2. Structures are labeled with their PDB ID (wtMS2; 2MS2, miniMS2; 4ZOR) and assembly state (6CP2; 6 coat protein dimers, 10CP2; 10 coat protein dimers). Ser37 (blue) and Thr71/Gly73 (green) are labeled with spheres. **(B)** A closer view of the assembly interface for each input structure.

Locally supercharged S37P mutants retain increased cellular uptake properties

To assess the ability of locally supercharged MS2[S37P/N87C] variants to retain their increased cellular uptake properties, purified capsids were labelled by conjugation of Lissamine rhodamine B maleimide to the interior Cys87 residues on each mutant. Capsid concentrations were normalized to 5 µM, and U-251 MG glioblastoma cells were treated with labelled

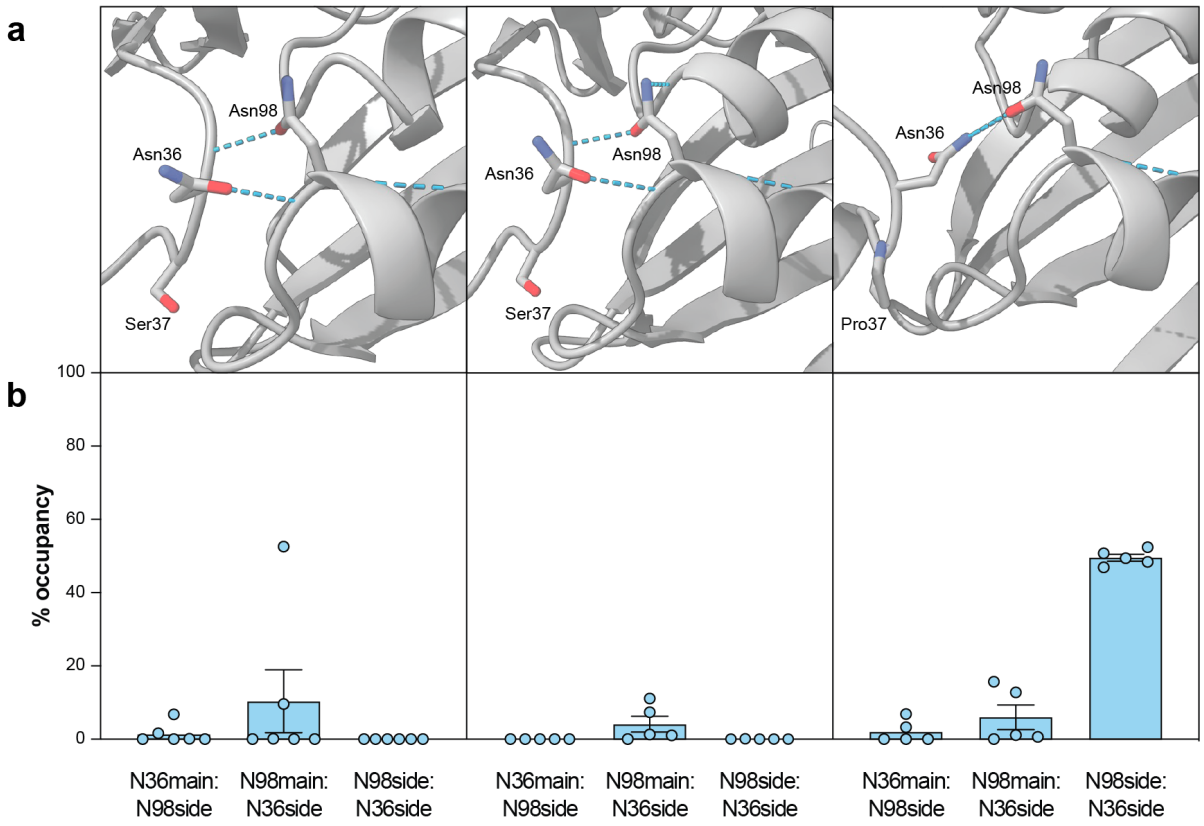


Figure 3.8: **(A)** The key hydrogen bonding interactions between Asn36 and Asn98 at each assembly interface, with the h-bonds labeled by light blue dashed lines. **(B)** H-bonding interactions were measured over the course of a 100ns trajectory. Bar graphs show the mean % H-bonding occupancy between Asn36 and Asn98 and error bars show one standard deviation. H-bonding interactions between the Asn36 backbone and Asn98 side chain (N36main:N98side), Asn98 backbone and Asn36 side chain (N98main:N36side), and Asn98 side chain and Asn36 side chain (N98side:N36side) are shown left to right. Each replicate measurement is shown as a blue circle on its respective graph.

capsids for 1 h before flow cytometry analysis. The internalization results measured by mean rhodamine fluorescence matched the patterns seen in similar experiments using locally supercharged MS2[N87C] variants. Specifically, MS2 capsids with single cationic mutations at positions 71 and 73 showed no or very low cellular uptake, while all combinations of double Arg and Lys mutants at positions 71 and 73 show greatly increased fluorescence when compared to both untreated and MS2[S37P]-treated cells (Figure 3.12). In this experiment, the best-performing variant, MS2[S37P/T71K/G73R/N87C], showed a mean fluorescence intensity that was 55-fold higher than cells treated with MS2[S37P].

These cellular internalization studies indicated that locally supercharged MS2[S37P-/N87C] capsids performed just as well as our previously-reported MS2[N87C] capsids with analogous mutations, with the added advantage of having single, thermally stable $T = 3$ assembly states. It is unclear how the formation of MS2 rod-like structures affects cellular

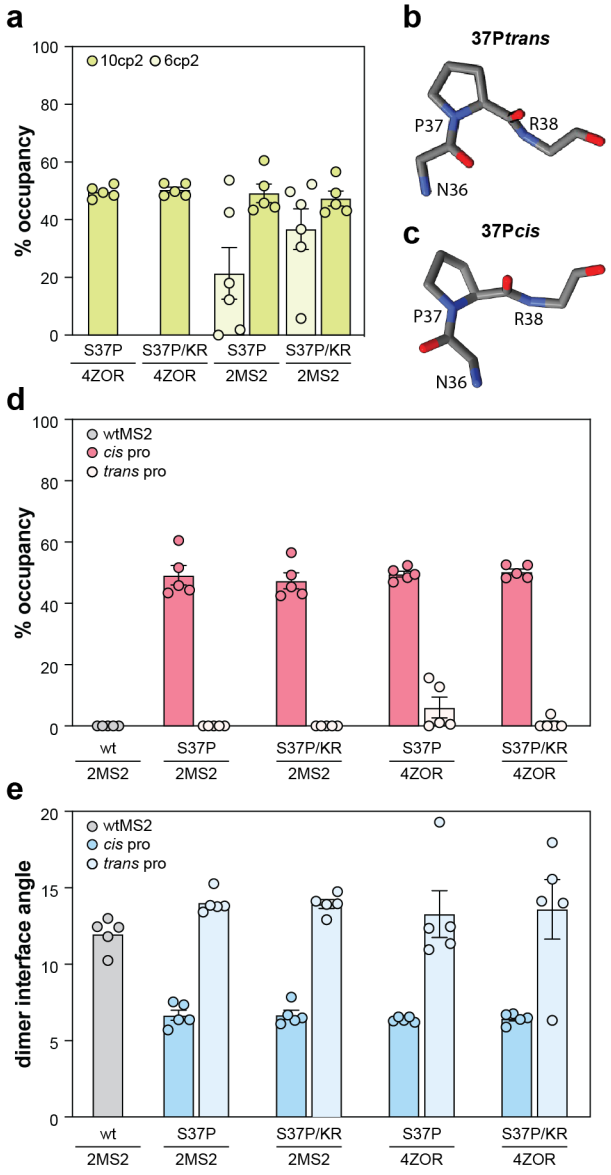


Figure 3.9: **(A)** Bar graph showing the mean % H-bonding occupancy of N98side:N36side interactions in different MS2 input structures. Error bars show SEM. 6CP2 (light green) and 10CP2 (green) measurements are shown when applicable. Structures of residues 36-38 showing *trans* **(B)** and *cis* **(C)** proline at position 37. **(D)** Bar graph showing the mean % H-bonding occupancy of N98side:N36side interactions in different MS2 10CP2 input structures. *Cis* proline (pink) and *trans* proline (light pink) are shown. **(E)** Bar graph showing the mean dimer interface angle between N36 and N98 in different MS2 10CP2 input structures. *Cis* proline (blue) and *trans* proline (light blue) are shown.

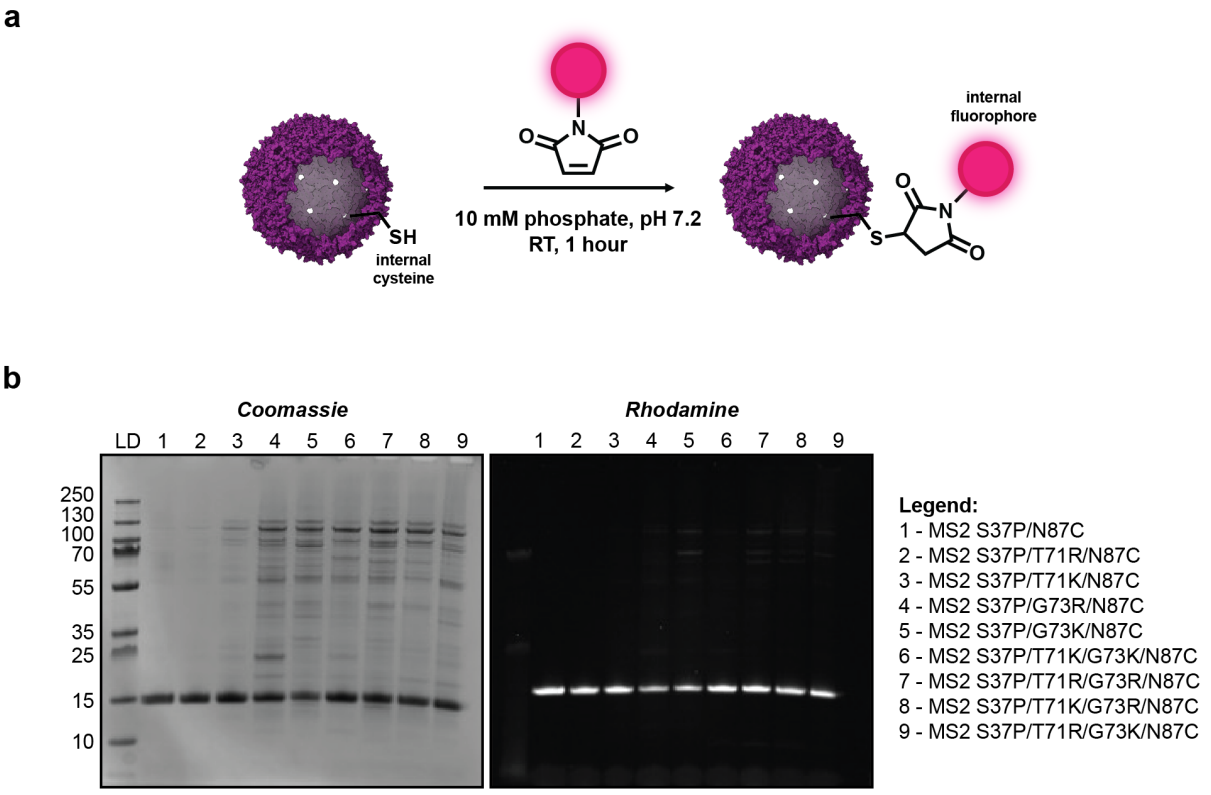


Figure 3.10: **(A)** Reaction scheme describing Lissamine rhodamine B maleimide coupling to the internal cysteine N87C of each MS2 CP variant. **(B)** SDS-PAGE analysis of S37P/N87C MS2 CP variant conjugation to Lissamine rhodamine B maleimide. Each conjugate was normalized to 5 µM after fluorophore coupling and 15 µL was analyzed via SDS-PAGE.

MS2 Variant	Unmodified Mass	+Rho Mass (Expected)	+Rho Mass (Observed)	+GSH Mass	%Rho Modification
S37P/N87C	13728	14409	14408	14035	71
S37P/T71R/N87C	13783	14464	14464	14090	77
S37P/T71K/N87C	13755	14436	14436	14062	79
S37P/G73R/N87C	13827	14508	14508	14134	71
S37P/G73K/N87C	13799	14480	14480	14106	70
S37P/T71R/G73R/N87C	13882	14563	14563	14189	53
S37P/T71K/G73K/N87C	13826	14507	14507	14133	71
S37P/T71K/G73R/N87C	13854	14535	14535	14161	78
S37P/T71K/G73K/N87C	13854	14535	14535	14161	79

Table 3.3: Expected and observed masses of S37P/N87C MS2 CP variants.

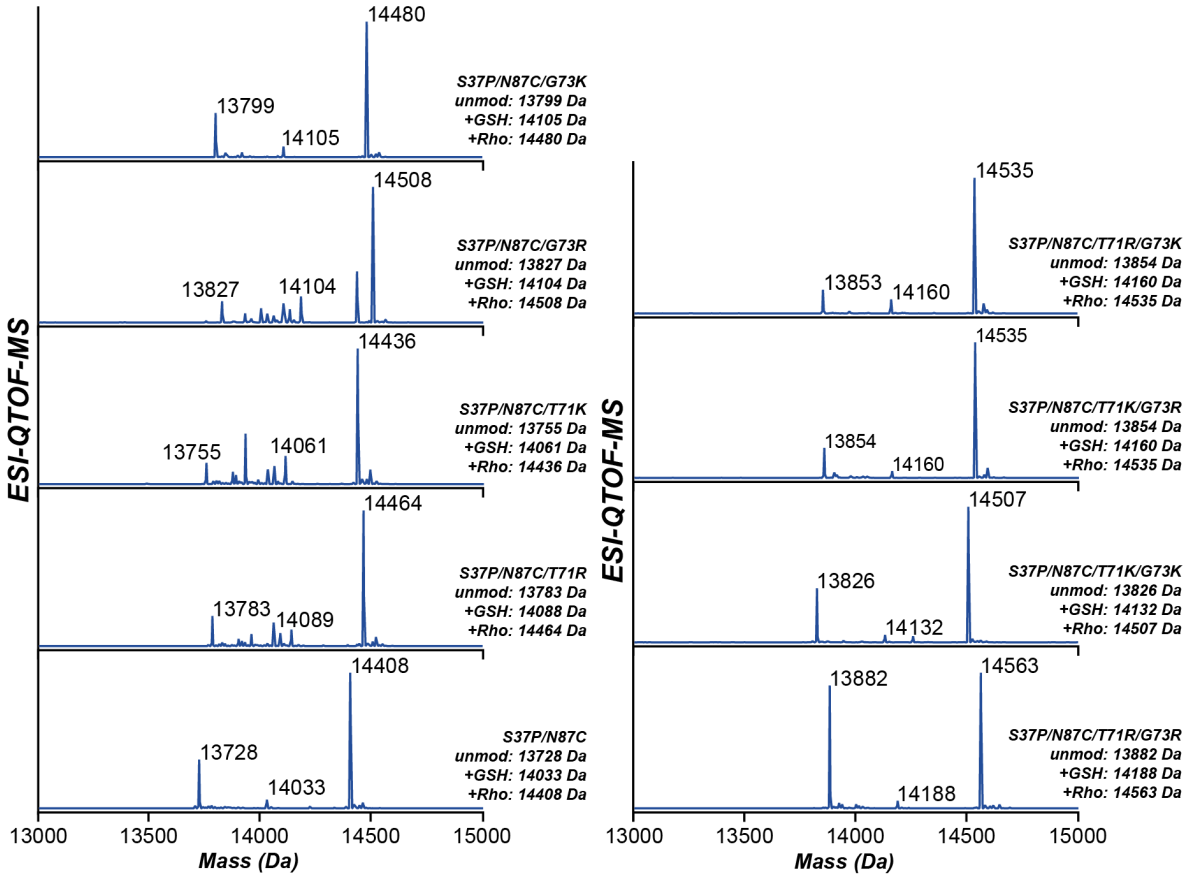


Figure 3.11: LC-QTOF-MS analysis of Lissamine rhodamine B maleimide conjugation to S37P/N87C MS2 CP variants. Each variant was modified 53%-79% by Lissamine rhodamine B maleimide (Rho, +682 Da), and small amounts of glutathione addition product were observed (GSH, + 307 Da).

internalization and if these rods are taken up into mammalian cells along with the $T = 3$ icosahedral particles. Unfortunately we have not yet been able to create $T = 1$ miniMS2 capsids that retain the same combinations of cellular uptake-enhancing mutations and study the effects of particle size on internalization. Previous work by other groups has explored the shape and size dependence of viral uptake using tobacco mosaic virus (TMV) and cowpea chlorotic mottle virus (CCMV). Some studies have suggested that materials with high aspect ratios (rod-like and filamentous structures) are internalized by cells differently than materials with low aspect ratios (spheres); however, these studies did not look into the difference of differently-sized particles with the same aspect ratio (e.g. $T = 3$ versus $T = 1$ particles) [205–208].

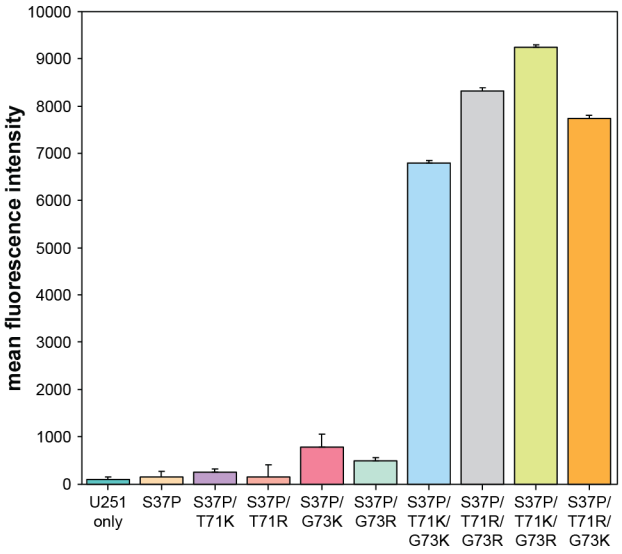


Figure 3.12: Bar graphs showing corrected mean fluorescence intensity of MS2-Lissamine rhodamine B internalization into U-251 MG cells. Error bars show the coefficient of variation. Data shown are a concatenation of three biological replicates as measured by flow cytometry.

Treatment	Cell Count	Mean Fluorescence Intensity	Median Fluorescence Intensity	Coefficient of Variation	Corrected Mean Fluorescence Intensity
U-251 MG only	25256	97.7	93.9	47.4	97.7
S37P	26067	154	138	109	171
S37P/T71R	25769	149	134	257	149
S37P/T71K	21181	249	230	66.9	255
S37P/G73R	29131	487	450	66	549
S37P/G73K	29511	789	710	265	877
S37P/T71K/G73K	26154	6788	6177	58.4	7552
S37P/T71R/G73R	25802	8316	7341	64	12395
S37P/T71R/G73K	29949	7744	6838	66.1	7744
S37P/T71K/G73R	29935	9238	8044	64.8	9356

Table 3.4: Mean flow cytometry fluorescence intensity values with coefficient of variation for MS2-Rho internalization into U-251 MG cells.

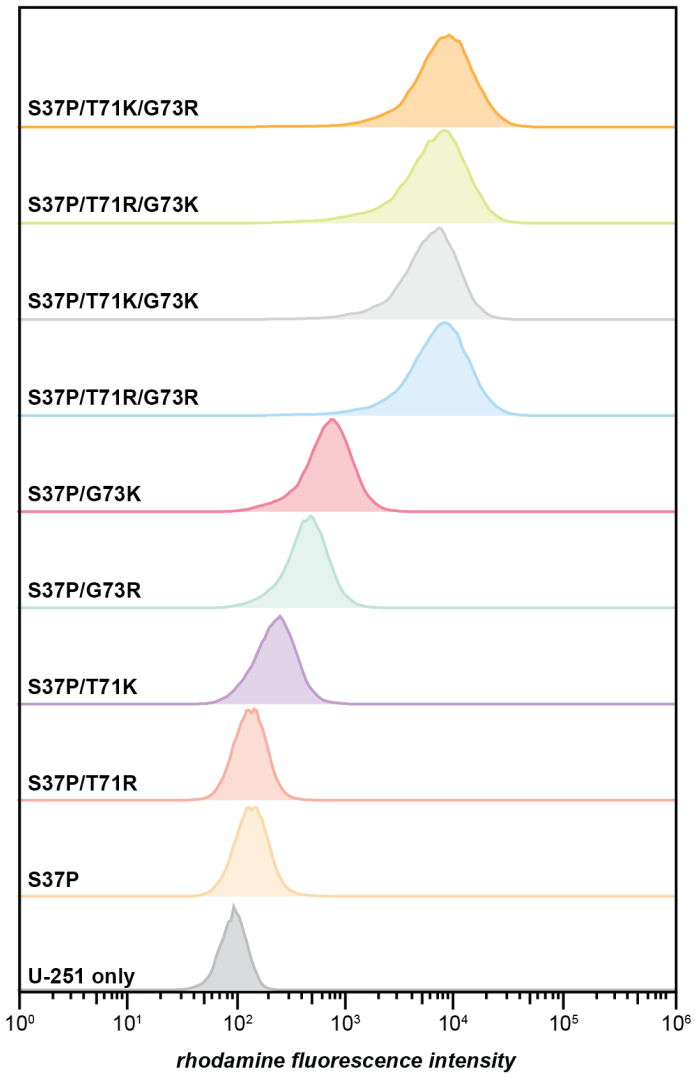


Figure 3.13: Histograms showing uptake of MS2-Rho into U-251 MG cells as measured by flow cytometry.

Comparing the intracellular delivery of small-molecule therapeutics

We next compared the delivery efficacy of a small molecule drug conjugated to the interior of locally supercharged MS2 (T71K/G73R) versus the stabilized mutant possessing S37P (S37P/T71K/G73R). Monomethyl auristatin E (MMAE) and monomethyl auristatin F (MMAF) are powerful anticancer drugs that block the polymerization of tubulin and inhibit cell division. These drugs are generally used in conjugates with monoclonal antibodies (mAbs) to create antibody-drug conjugates (ADCs) with targeted cytotoxicity. THIOMABs with engineered cysteines have been developed for the conjugation of cysteine-reactive drug molecules, such as maleimides, to antibodies [190]. An enzyme-cleavable dipeptide Val-Cit linker is used to allow for cleavage and release of the free drug by the cathepsin B lysosomal protease upon cell entry (Figure 3.16) [191–193]. MMAE and MMAF have similar potencies but different membrane permeabilities due to the presence of a negatively charged carboxylic acid group on MMAF. Therefore, we hypothesized that the delivery of MMAF would be improved by conjugation to the interior of MS2, given its ability to load up to 180 drug copies per capsid and shield its negative charge from the anionic mammalian cell exterior. Maleimide-Val-Cit-PAB-MMAF was conjugated to the interior cysteine of wtMS2, miniMS2, and all combinations of MS2 T71K/G73R and T71R/G73K with and without the stabilizing S37P mutation. Each MS2 CP variant was modified to 86-93% by monomer with MMAF or about 154-168 molecules per capsid (Figure 3.15, Table 3.5).

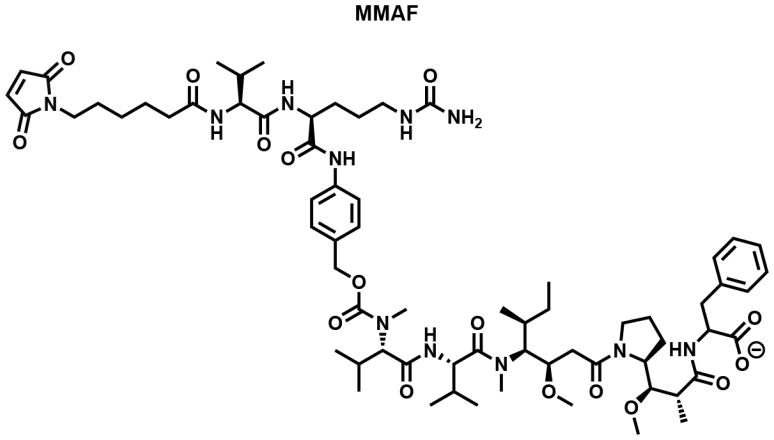


Figure 3.14: Structure of maleimide-Val-Cit-PAB-MMAF (MMAF).

The efficacy of MS2-MMAF was measured by a dose-response assay in U-251 MG cells. Cells were treated for 72 h with up to 1000 nM MMAF conjugated to each of six MS2 variants. The calculated IC_{50} values for MMAF treatment with each MS2 variant are shown in Figure 3.16. These data show that MMAF delivery with locally supercharged variants result in a drastic increase in efficacy versus delivery of MMAF with wtMS2 or miniMS2, and up to 328-fold increase in efficacy versus delivery of free MMAF. Although no significant difference in efficacy was observed when comparing MS2 variants with versus without the

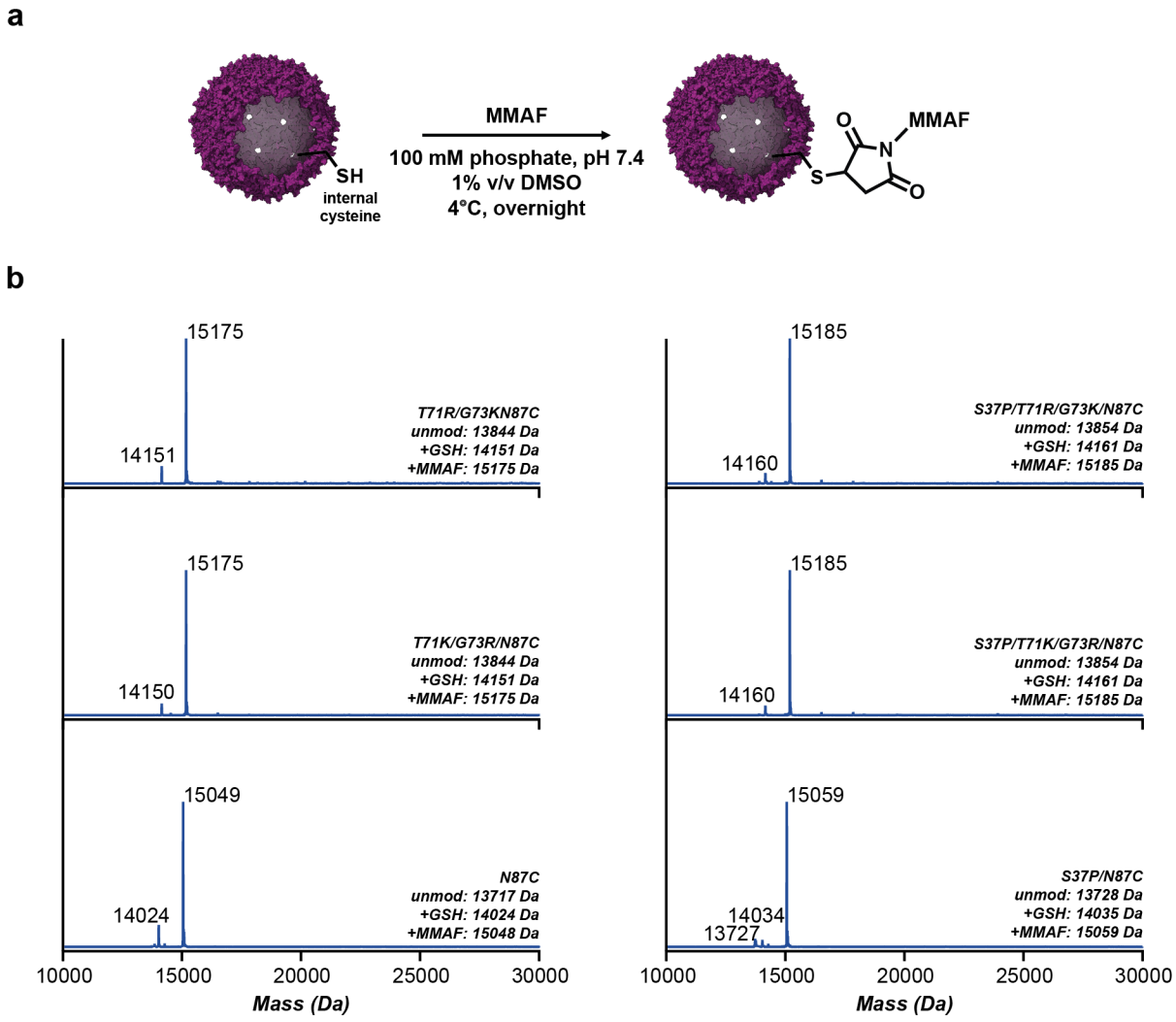


Figure 3.15: **(A)** Reaction scheme describing maleimide-Val-Cit-PAB-MMAD coupling to the internal cysteine N87C of MS2 CP. **(B)** LC-MS analysis of MS2-MMAE conjugates. Each variant was modified 86%-93% by MMAF (+1332 Da), and small amounts of glutathione (GSH, +307 Da) addition product were observed.

MS2 Variant	Unmodified Mass	+MMAF Mass (Expected)	+MMAF Mass (Observed)	+GSH Mass	%MMAF Modification
N87C	13717	15048	15049	14024	86
T71K/G73R/N87C	13844	15175	15175	14151	93
T71R/G73K/N87C	13844	15175	15175	14151	89
S37P/N87C	13728	15059	15059	14036	86
S37P/T71K/G73R/N87C	13854	15185	15185	14161	93
S37P/T71R/G73K/N87C	13854	15185	15185	14161	90

Table 3.5: Masses (Da) of products obtained from MS2 CP variant maleimide-Val-Cit-PAB-MMAF (MMAF) labeling reactions determined by QTOF-ESI-MS.

stabilizing S37P mutation, these capsids are still a valuable addition to the MS2 drug delivery arsenal due to their structural homogeneity and ease of storage.

3.4 Conclusion

Previous work has established that VLP assembly states can be modified via simple point mutations, providing a platform for the creation of particles with fine-tuned sizes, stabilities, and other properties. By using a combination of experimental techniques and molecular dynamics simulations, this work explores how specific mutations at the intersubunit interfaces of MS2 impact the local and global structure and function of these capsids. Notably, we reveal that placing cationic mutations at critical interface residues can induce unexpected changes in particle geometry, leading to the formation of rod-like structures alongside capsids with expected assembly states. When combined with the 5-fold-favoring S37P mutation, we observe VLPs with an unexpected $T = 3$ assembly state, improved thermostability, and retained enhancement of cellular uptake properties. Molecular dynamics experiments further explain these findings, providing structural insights at the atomistic level into the importance of intradimer hydrogen bonding interactions on global capsid structure and assembly. Additionally, we demonstrate the efficacy of these engineered VLPs in delivering the anionic small-molecule drug MMAF, achieving up to 300-fold increases in potency over the free drug. This showcases the potential of these engineered capsids for biomedical applications. Moreover, these results highlight the importance of understanding the sequence-structure relationship of self-assembling, protein-based materials such as VLPs in order to improve their potential for applications such as drug delivery.

3.5 Materials

General information

All materials were acquired from commercial sources and used without further purification unless otherwise indicated. Milli-Q (MQ) H_2O was purified to a resistivity of 18.2 Ω•cm (at

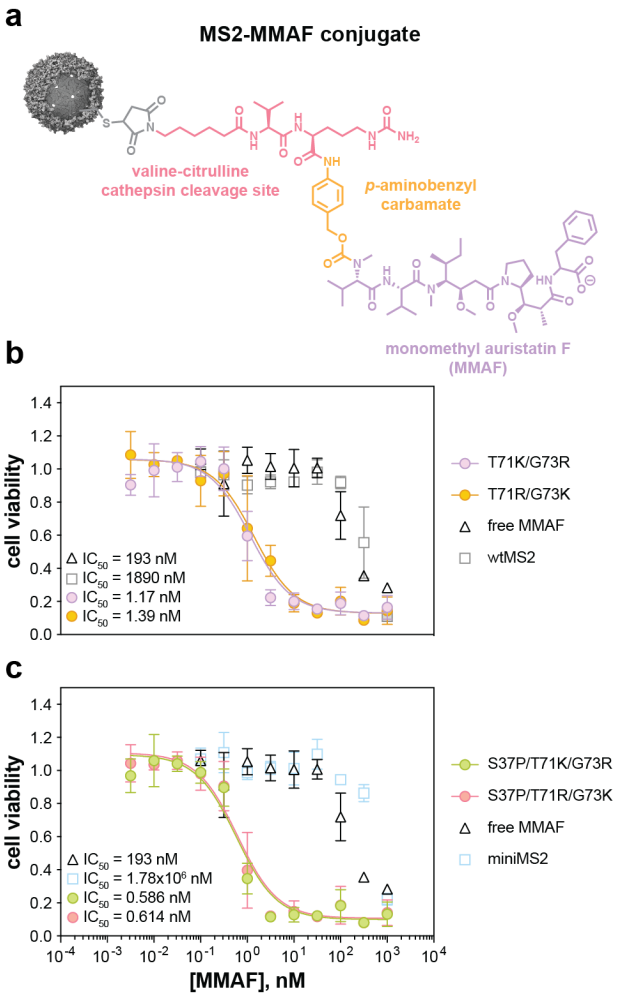


Figure 3.16: **(A)** Structure of the MS2-MMAF conjugate. MS2 capsid with an interior cysteine conjugated to maleimide handle (grey), Val-Cit linker (pink), *p*-aminobenzyl carbamate linker (orange), and MMAF (purple). **(B)**, **(C)** MS2-MMAF dose response assays for MS2[N87C] variants and MS2[S37P/N87C] variants, respectively. Results are shown for an MTS assay of U-251 MG cells 72 h after treatment with 0.003-1000 nM MMAF. Plot shows mean % cell viability of three biological replicates. Error bars shown one standard deviation.

25 °C) using a MQ Gradients ultrapure water purification system from Millipore (Burlington, MA).

Plasmid design, protein expression and purification

DNA primers for QuikChange mutagenesis were purchased from Integrated DNA Technologies (Coralville, IA). QuikChange Lightning site-directed mutagenesis kit was purchased from Agilent (Santa Clara, CA). Wizard® SV Gel and PCR Clean-Up System was purchased from Promega (Madison, WI). *E. coli* DH10B cells were purchased from the UC Berkeley MacroLab (Berkeley, CA). Zyppy™ plasmid miniprep kit was purchased from Zymo Research (Irvine, CA). DNA sequencing was performed by Sequetech. Corning® Costar® Spin-X® centrifuge tube filters, Amicon Ultra-0.5 mL 100 kDa MWCO filters, and 2x YT medium powder were purchased from Sigma Aldrich (St. Louis, MO). HiScreen Capto Core 700 column, Microspin™ G-25 columns, and Amersham NAP-5 columns were purchased from Cytiva Lifesciences (Marlborough, MA). Bio SEC-5 HPLC column was purchased from Agilent (Santa Clara, CA). NuPAGE™ 4 to 12%, Bis-Tris precast gels, NuPAGE™ MES SDS Running Buffer was purchased from Thermo Fisher (Waltham, MA). Lissamine rhodamine B C2 maleimide was purchased from Tenova Pharmaceuticals (San Diego, CA).

Cell culture and assays

U251-MG cells were obtained from the UCSF Brain Tumor center. Dulbecco's modified eagle medium (DMEM, with Phenol Red), Dulbecco's phosphate-buffered saline (DPBS), TrypLE, Hoechst 33342 stain, glutamine, and sodium pyruvate were purchased from Thermo Fisher (Waltham, MA). MTS Assay Cell Proliferation Kit was purchased from Abcam (Cambridge, UK) Invitrogen SYPRO protein gel stain was purchased from Fisher Scientific (Hampton, NH).

Equipment

For plasmid and protein concentration quantification, a ND-1000 (NanoDrop) spectrophotometer was used. A Sorvall X Pro Series centrifuge was used for protein expression (Thermo Fisher). An AKTA Go FPLC (Cytiva), with a HiScreen Capto Core 700 column was used for protein purification. A 1260 Infinity HPLC (Agilent) was used for MS2 assembly confirmation and a 6530 LC/QTOF (Agilent) mass spectrometer was used for characterization of MS2 variants. For cellular internalization, an Attune NxT Flow Cytometer (Thermo Fisher) was used. A BioRad CFX Connect Real-Time PCR Detection System was used for thermal shift assays. Transmission electron microscopy (TEM) was performed on a Tecnai 12 Transmission Electron Microscope equipped with a 2k x 2k CCD camera. Absorption readings after MTS cell proliferation assays were performed on an Infinite 200 PRO plate reader (Tecan).

3.6 Methods

Safety note

No unexpected or unusually high safety hazards were encountered. Uranyl acetate staining must be performed with proper radioactive materials training.

Cloning procedure

MS2 variants with mutations at positions 71 and 73 were previously generated with EMPIRIC cloning [152, 195]. Two single-stranded DNA primers were purchased, resuspended, and diluted to 5 µM for S37P site-directed mutagenesis. Site-directed mutagenesis was performed according to the protocols defined in the QuikChange Lightning Instruction Manual. Mutant strand synthesis was performed and methylated template DNA was digested with DpnI. Amplification products were transformed into chemically competent *E. coli* DH10B cells. Cells were plated onto LB agar plates containing 32 µg/mL chloramphenicol and grown overnight at 37 °C. Individual colonies were picked and grown overnight in 2xYT media containing 32 µg/mL chloramphenicol at 37 °C, then plasmid DNA was isolated by Zyppy™ plasmid miniprep kit and sent for sequencing with pBAD forward and pBAD reverse sequencing primers.

DNA primer sequences

Number	Sequence
EV3 S37P N87C QC F	CGTTCGTACTTATGCATGGAACTAACCCCAATTTTCGCTACG
EV3 S37P N87C QC R	CGTAGCGAAAATTGGAATGGTTAGTTCCATGCATAAGTACGAACG

Table 3.6: Primer sequences for QuickChange to generate MS2 S37P variants.

Expression and purification of proteins

Overnight cultures of each MS2 variant were subcultured 1:200 into 1 L of 2xYT media containing 32 µg/mL chloramphenicol and grown to an OD_{600} of 0.4-0.6, then induced with 0.1% w/v arabinose. Proteins were expressed overnight at 37 °C with 220 rpm shaking, then cells were harvested by centrifugation and lysed by sonication. MS2 capsids were precipitated with two rounds of 50% saturated ammonium sulfate. Large-scale expressions of well-assembled MS2 variants were purified via FPLC on two HiScreen Capto Core 700 columns connected in series via isocratic flow with 10 mM phosphate buffer at pH 7.4 with 2 mM sodium azide as the equilibration, wash, and elution buffer, and 1 M NaOH in 30% isopropanol as the cleaning-in-place buffer. Some MS2 variants with cationic mutations were purified via affinity chromatography with a 5 mL HiTrap Heparin HP affinity column with

10 mM phosphate buffer at pH 7.4 with 2 mM sodium azide as the equilibration and wash buffer, and 2 M NaCl as the elution buffer.

Sequences of expressed proteins

MS2 wt
ASNFTQFVLVDNGGTGDVTVAPSNFANGVAEWISSNSRSQAYKVTCSVRQSSAQNR
KYTIKVEVPKVATQTVGGVELPVAAWRSYLNMELTIPIFATNSDCELIVKAMQGLL
KDGNPIPSAIAANSGIY
MS2 N87C
ASNFTQFVLVDNGGTGDVTVAPSNFANGVAEWISSNSRSQAYKVTCSVRQSSAQNR
KYTIKVEVPKVATQTVGGVELPVAAWRSYLCMELTIPIFATNSDCELIVKAMQGLL
KDGNPIPSAIAANSGIY
MS2 S37P/N87C
ASNFTQFVLVDNGGTGDVTVAPSNFANGVAEWISSNPRSQAYKVTCSVRQSSAQNR
KYTIKVEVPKVATQTVGGVELPVAAWRSYLCMELTIPIFATNSDCELIVKAMQGLL
KDGNPIPSAIAANSGIY
MS2 S37P/T71R/N87C
ASNFTQFVLVDNGGTGDVTVAPSNFANGVAEWISSNPRSQAYKVTCSVRQSSAQNR
KYTIKVEVPKVATQRVGGVELPVAAWRSYLCMELTIPIFATNSDCELIVKAMQGLL
KDGNPIPSAIAANSGIY
MS2 S37P/T71K/N87C
ASNFTQFVLVDNGGTGDVTVAPSNFANGVAEWISSNPRSQAYKVTCSVRQSSAQNR
KYTIKVEVPKVATQKVGGVELPVAAWRSYLCMELTIPIFATNSDCELIVKAMQGLL
KDGNPIPSAIAANSGIY
MS2 S37P/G73R/N87C
ASNFTQFVLVDNGGTGDVTVAPSNFANGVAEWISSNPRSQAYKVTCSVRQSSAQNR
KYTIKVEVPKVATQTVRGVELPVAAWRSYLCMELTIPIFATNSDCELIVKAMQGLL
KDGNPIPSAIAANSGIY
MS2 S37P/G73K/N87C
ASNFTQFVLVDNGGTGDVTVAPSNFANGVAEWISSNPRSQAYKVTCSVRQSSAQNR
KYTIKVEVPKVATQTVKGVELPVAAWRSYLCMELTIPIFATNSDCELIVKAMQGLL
KDGNPIPSAIAANSGIY
MS2 S37P/T71R/G73R/N87C
ASNFTQFVLVDNGGTGDVTVAPSNFANGVAEWISSNPRSQAYKVTCSVRQSSAQNR
KYTIKVEVPKVATQRVRGVELPVAAWRSYLCMELTIPIFATNSDCELIVKAMQGLL
KDGNPIPSAIAANSGIY
MS2 S37P/T71K/G73K/N87C
ASNFTQFVLVDNGGTGDVTVAPSNFANGVAEWISSNPRSQAYKVTCSVRQSSAQNR
KYTIKVEVPKVATQKVKGVELPVAAWRSYLCMELTIPIFATNSDCELIVKAMQGLL
KDGNPIPSAIAANSGIY
MS2 S37P/T71K/G73R/N87C

ASNFTQFVLVDNGGTGDVTVAPSNFANGVAEWISSNPRSQAYKVTCSVRQSSAQNR
KYTIKVEVPKVATQKVRGVELPVAAWRSYLCMELTIPIFATNSDCELIVKAMQGLL
KDGNPIPSAIAANSGIY
MS2 S37P/T71R/G73K/N87C
ASNFTQFVLVDNGGTGDVTVAPSNFANGVAEWISSNPRSQAYKVTCSVRQSSAQNR
KYTIKVEVPKVATQRVKGVELPVAAWRSYLCMELTIPIFATNSDCELIVKAMQGLL
KDGNPIPSAIAANSGIY

Determination of assembly state

The assembly state of each MS2 variant was characterized via HPLC size exclusion chromatography with an Agilent bioSEC-5 column (5 µm, 2000 Å, 7.8x300 mm) with isocratic flow of 10 mM phosphate buffer at pH 7.4 with 2 mM sodium azide. Coelution of A_{260} and A_{280} peaks at 6 min are indicative of $T = 3$ assembled capsids and at 8 min for $T = 1$ assembled capsids, while a peak at 10 min corresponds to the elution of unassembled MS2 dimers.

Mass spectrometry

Modified and unmodified MS2 CP variants were analyzed with an Agilent 1260 series liquid chromatograph connected in-line with an Agilent 6530 LC/QTOF mass spectrometer with an electrospray ionization source. The expected mass of each MS2 CP variant was confirmed via QTOF-ESI-MS (Figure 3.2, Table 3.3).

Dye modification

All MS2 CP variants containing the N87C mutation (final concentration 10 µM) were mixed with 5 equivalents of Lissamine rhodamine B C2 maleimide (stock solution 5 mM in DMSO, 50 µM final concentration) in 10 mM phosphate buffer, pH 7.2. The solution was incubated on a rotator at room temperature for 1 h or at 4 °C overnight. Excess dye was removed by three rounds of washes through Amicon Ultra-0.5 mL 100 kDa MWCO filters and two rounds of filtration through Microspin™ G-25 columns. Modification of MS2 CP variants was verified via QTOF-ESI-MS and SDS-PAGE. The concentration of each MS2-fluorophore conjugate (MS2-Rho) was normalized to 5 µM for subsequent internalization assays (Figure 3.2-3.10).

Synthesis of MMAF-conjugated MS2 capsids

Samples of each MS2 construct were prepared at 20 µM and combined with 10 equivalents of a stock solution of maleimide-Val-Cit-PAB-MMAF (Broadpharm) in 100 mM phosphate buffer (1% v/v DMSO) pH 7.4, and incubated overnight at 4 °C. Excess MMAF was removed via 7 cycles of spin filtration through a 100 kDa MWCO filter (Amicon) and product was analyzed by QTOF-ESI-MS (Figure 3.15, Table 3.5).

MTS cell viability assay

An MTS Assay Kit (ab197010) was used according to Abcam's instructions to quantify cell viability after treatment with different MS2 CP variants. Briefly, an MTS tetrazolium compound is reduced by viable mammalian cells to generate a colored formazan dye that can be measured by absorbance at 490 nm. U-251 MG cells were plated into a 96-well plate at a concentration of 5,000 cells per well in 100 µL DMEM + FBS and incubated overnight at 37 °C with 5% CO_2. The next day, media was aspirated and replaced with 100 µL of either 0, 1, 5, 10, 20, or 40 µM MS2 diluted in DMEM + FBS and incubated for 24, 48, or 72 h at 37 °C with 5% CO_2. Then, the treatment media was aspirated and 100 µL DMEM + 20% MTS reagent was added to each well and incubated for 1 h at 37 °C with 5% CO_2 before measuring the absorbance at 490 nm. Cell viability was calculated as an absorbance percentage over the untreated control (Equation 3.1).

$$\% \text{ viability} = 100 * \frac{A490 \; treated \; cells}{A490 \; control \; cells} \tag{3.1}$$

MS2-MMAE MTS cell viability assay

U-251 MG cells were plated in a 96-well plate at 4,000 cells/well and allowed to adhere overnight. Cells were then incubated for 72 h at 37 °C with 80 µL DMEM + 10% FBS and 20 µL MS2-MMAE or vehicle control at appropriate concentrations in DPBS. Media were then aspirated and replaced with 200 µL pre-warmed DMEM without phenol red or FBS along with 20 µL Abcam MTS Cell Proliferation Assay solution. Samples were then incubated in the dark for 1 h and immediately analyzed for optical density at 490 nm. Cell viability was calculated as an absorbance percentage over the untreated control (Equation 3.1).

Mammalian cell culture

U-251 MG cells were cultured in DMEM supplemented with 10% fetal bovine serum (FBS), 4.5 g/L glucose, 4 mM L-glutamine, and 1 mM sodium pyruvate. All cell cultures were maintained at 37 °C in a humidified atmosphere with 5% CO_2.

Flow cytometry

A suspension of 80,000 U-251 MG cells were plated in each well of a 24-well plate and incubated overnight at 37 °C with 5% CO_2. Cells were washed three times with DPBS and treated with 5 µM MS2-Rho in DPBS with 1% FBS for 1 h at 37 °C with 5% CO_2. After incubation, cells were washed twice with DPBS. Cells were lifted with trypsin, quenched with FBS-containing DMEM and pelleted at 200 x g for 3 min. Cells were washed twice with DPBS and resuspended in 1 mL of DPBS. Cells were pelleted at 200 x g for 3 min

and resuspended in 1 mL 2% paraformaldehyde with 0.1 µg/mL Hoechst 33342 and kept at 4 °C until flow cytometry analysis. Flow cytometry was completed using an Attune NxT flow cytometer. At least 10,000 cells were analyzed for each sample. Data were analyzed using FlowJo and the mean fluorescence values with coefficient of variation were reported (Figure 3.13, Table 3.4). Fluorescence intensity values were corrected according to the % Rho modification of each MS2 CP variant.

Generation of S37P MS2 structural models

A $T = 1$ model of S37P MS2 containing all amino acid residues was generated based on the crystal structure of S37P MS2 (PDB ID: 4ZOR) [52]. The missing loop regions of this structure were added using the Homology Modeling tool in Maestro (version 22.2) using 4ZOR as a template. Copies of the resulting homology model were then position aligned with five pentameric monomers of 4ZOR using the Align tool in PyMOL (version 3.0.0). The resulting pentamers were converted into the full 60-mer using the Multiscale Models tool in UCSF Chimera (version 1.17.3). Segments of this capsid comprising 20 monomers surrounding the 5-fold symmetry axes were then used in molecular dynamics simulations. A $T = 3$ model of S37P MS2 containing all amino acid residues was generated based on the crystal structure of wtMS2 (PDB ID: 2MS2) [209]. Initial structure preparation was conducted using Schrodinger Maestro suite (version 2022-2). Subsequent MS2 variants used in simulations were created using the Mutate tool in Maestro, then performing a short minimization with an OPLS4 force field to relax the structure around the mutation sites.

Molecular dynamics simulations

Molecular dynamics simulations were carried out using Desmond in the Maestro 2022-2 environment. Starting structures were obtained from the structural models described above. The System Builder tool was used to generate an orthorhombic simulation box with 10 Å boundaries on all sides. The simulation box was filled with water molecules using the TIP4PEW water model [210]. NaCl ions were added to achieve system neutrality and to reach a salt concentration of 0.15 M. Following equilibration, 100 ns production runs were completed using the OPLS4 force field [211]. Trajectories were prepared for analysis with VMD (version 1.9.4a55) [212]. Data analysis was carried out with VMD and in-house code using the MDAnalysis Python package [213, 214]. All trajectories showed minimal changes in RMSD values over the simulation times (Figures 3.35, 3.36, 3.37, 3.38, 3.39, 3.40, 3.41, 3.42, 3.43). Hydrogen bond occupancy over each trajectory was measured using the Hydrogen Bonds Analysis extension in VMD with a donor:acceptor distance cutoff of 3.0 Å and an angle cutoff of 20°. Hydrogen bond occupancy was calculated as the percentage of time during which H-bonding criteria are met over the course of the trajectory. The script for interdimer contact angle calculations can be found on GitHub (https://github.com/ppistono).

Thermal shift assay

SYPRO orange thermal shift assays were conducted in triplicate in 96-well plates using a BioRad CFX Connect RT-PCR instrument. Temperatures were increased by 1 °C increments from 25 °C to 95 °C. During this process, the SYPRO orange dye binds to MS2 dimers as capsid disassembly and protein denaturation occurs. MS2 variants were tested for individual optimal assay conditions using 5, 10, 15, or 20 µM MS2 (by monomer concentration with 1x to 8x SYPRO orange dye). The best conditions for data collection were found to be 10 µM MS2 and 6x dye after assay optimization. For melting point determination, a Boltzmann sigmoidal model fit was employed using Prism-9, where T_m can be calculated as V_{50} (Equation 3.2) [215]. For all MS2 mutants, melt curve derivatives were analyzed using the Peakdetect module in Python. The Tm values are reported as mean and standard deviation of each set of replicates. Two melting points, T_m1 and T_m2, were observed in some datasets, suggesting that certain mutants exhibit cooperative melting profiles (Figure 3.17, Table 3.2).

$$Y = \text{Bottom} + \frac{\text{Top} - \text{Bottom}}{1 + e^{(\frac{V_{50} - X}{\text{Slope}})}} \tag{3.2}$$

Transmission electron microscopy sample preparation

MS2 CP samples were spun down at 15k rpm for 15 min at 4 °C to remove aggregates. Dilute (1 mg/mL) MS2 samples were then concentrated and washed three times with 1x PBS through 0.5 mL Amicon Ultra 100 kDa MWCO filters at 15k rpm for 3 min at 4 °C. Washed samples were diluted back to a concentration of 1 mg/mL in 1x PBS and spun down at 15k rpm for 15 min at 4 °C. Finally, samples were filtered through a 0.2 µm spin filter at 15k rpm for 30 sec.

Uranyl acetate negative staining

A 1% uranyl acetate staining solution was spun down at 5000 rpm for 10 min to remove aggregates. Carbon-coated copper grids were glow discharged and 6 µL of MS2 samples were pipetted onto the grid, incubated for 2 min, then washed 3 times with MQ H_2O. Excess liquid was removed from each grid with filter paper. Grids were then stained with 6 µL of 1% uranyl acetate, incubated for 1 min, and excess stain removed with filter paper.

Transmission electron microscopy

TEM images were acquired on a Tecnai 12 Transmission Electron Microscope. Images were acquired at 30,000x and 49,000x magnification and particle size was measured using the Set Scale and Measure tools in Fiji (Figures 3.18, 3.19, 3.20, 3.21, 3.22, 3.23, 3.24, 3.25, 3.26, 3.27, 3.28, 3.29, 3.30, 3.31, 3.32, 3.33, 3.34).

3.7 Supplementary Figures

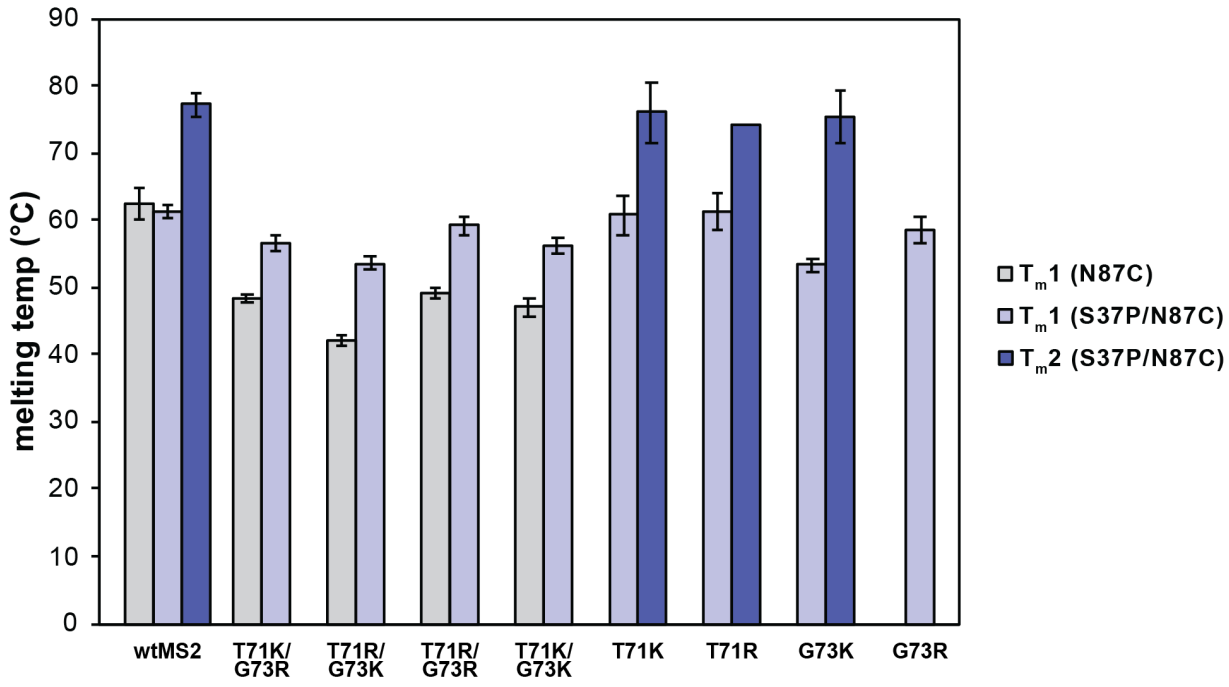


Figure 3.17: Bar graph showing average melting temp (T_m, °C) values for MS2 variants in a Sypro Orange thermal shift assay. Error bars show one standard deviation.

3.8 Acknowledgements

This work was supported by the Panattoni Family Fund and NSF 2044011. Computational studies in this work were completed with support from the UC Berkeley MGCF and NIH S10OD023532. We are grateful to M. West, manager at the QB3 CTAF, for qPCR and flow cytometry training, and R. Zalpuri at the UC Berkeley EML for negative staining and transmission electron microscopy training.

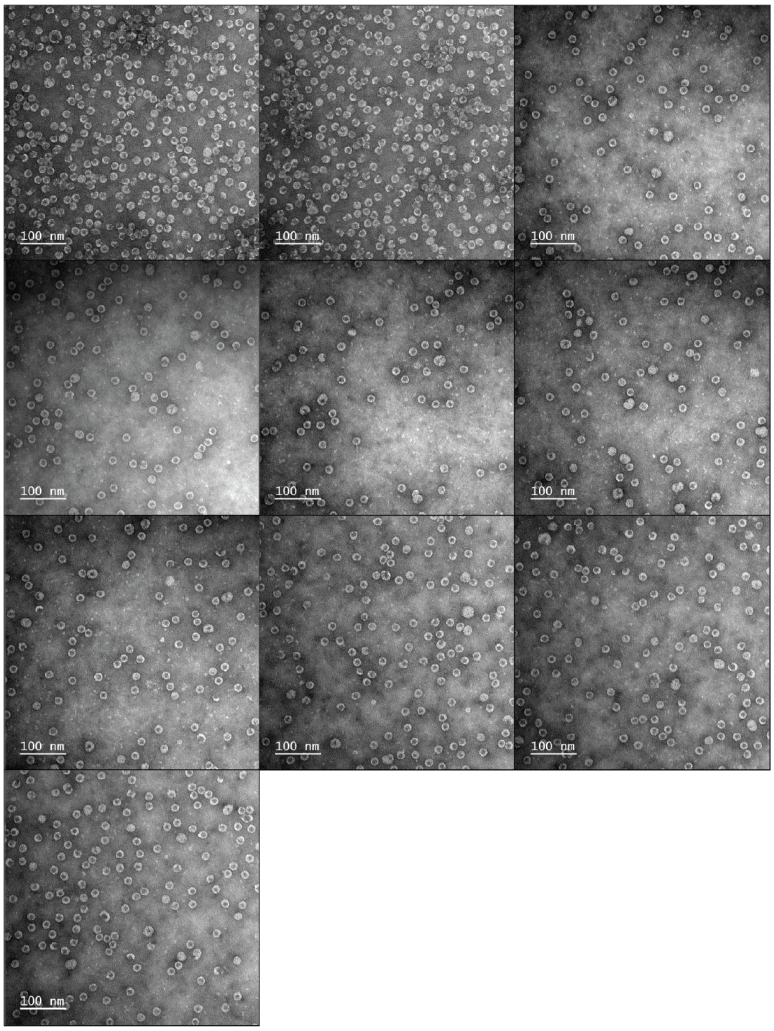


Figure 3.18: Transmission electron microscopy (TEM) images of MS2 S37P/T71R/N87C capsids.

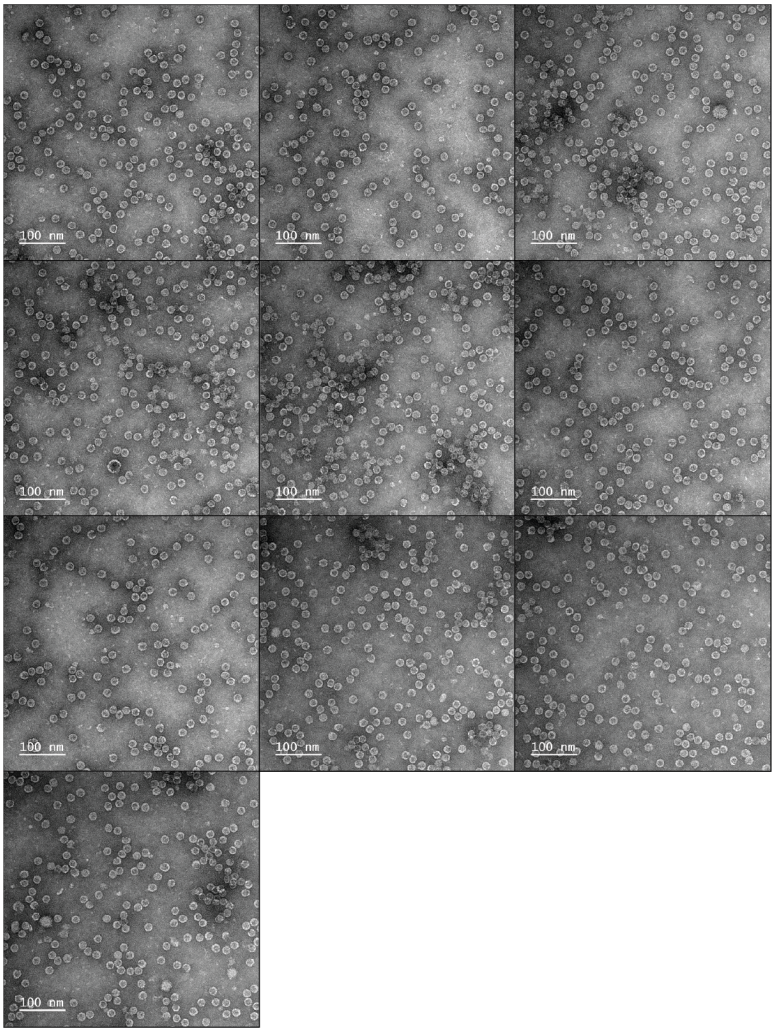


Figure 3.19: Transmission electron microscopy (TEM) images of MS2 S37P/T71K/N87C capsids.

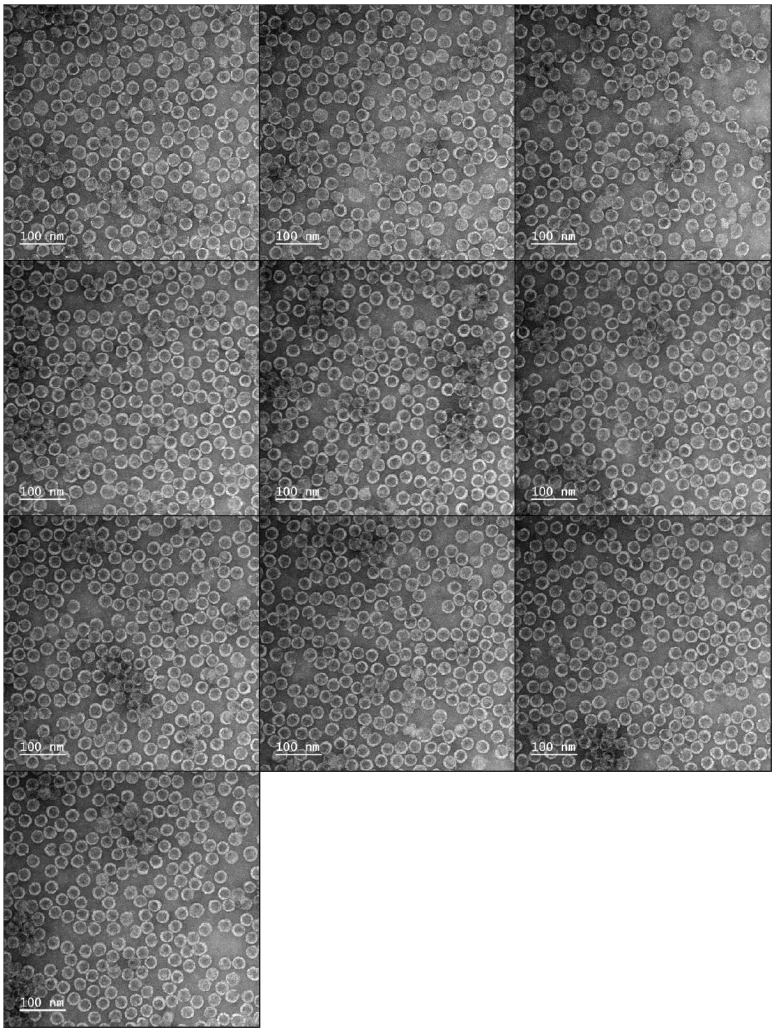


Figure 3.20: Transmission electron microscopy (TEM) images of MS2 T71R/G73R/N87C capsids.

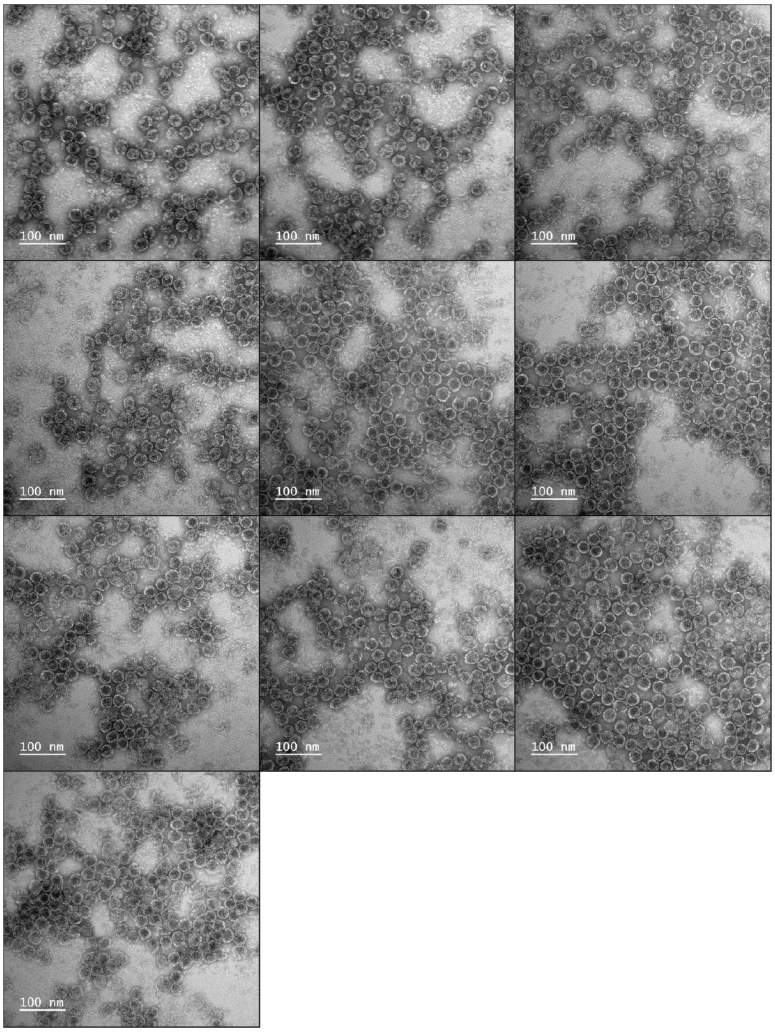


Figure 3.21: Transmission electron microscopy (TEM) images of MS2 T71R/G73K/N87C capsids.

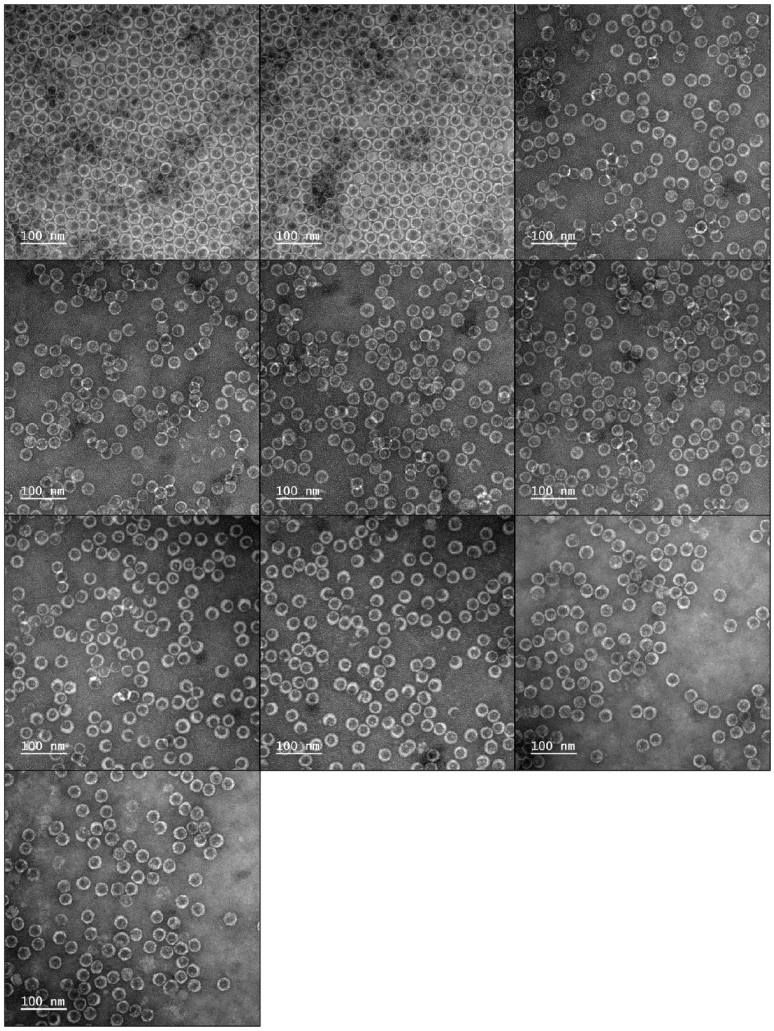


Figure 3.22: Transmission electron microscopy (TEM) images of MS2 T71K/G73R/N87C capsids.

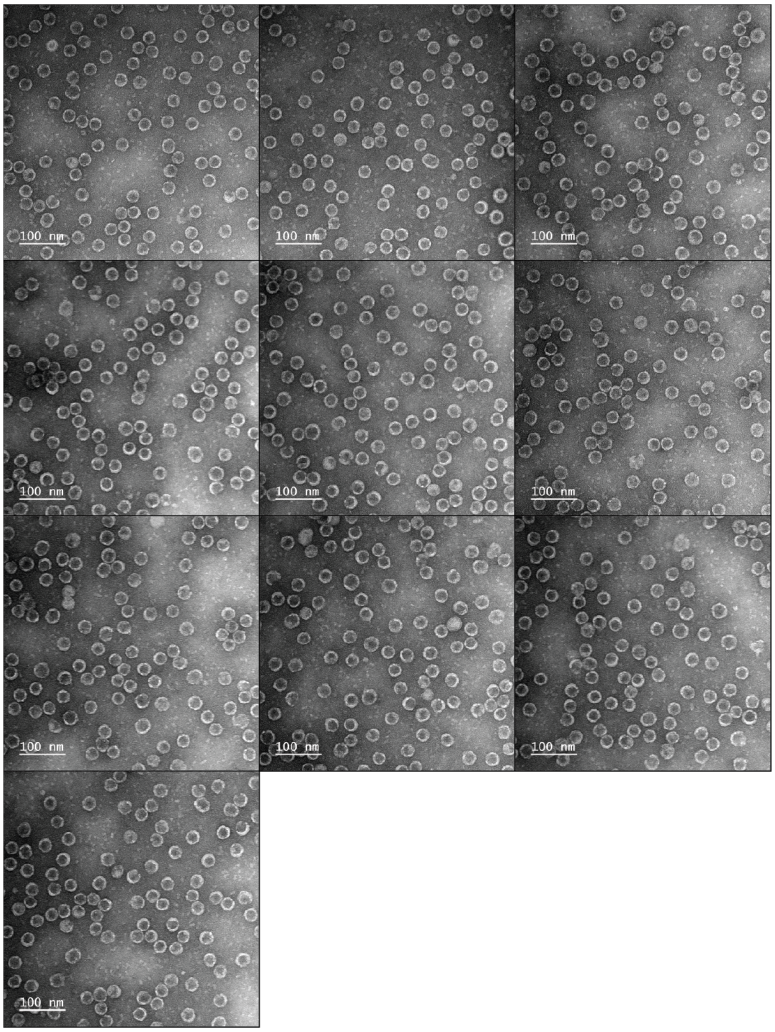


Figure 3.23: Transmission electron microscopy (TEM) images of MS2 T71K/G73K/N87C capsids.

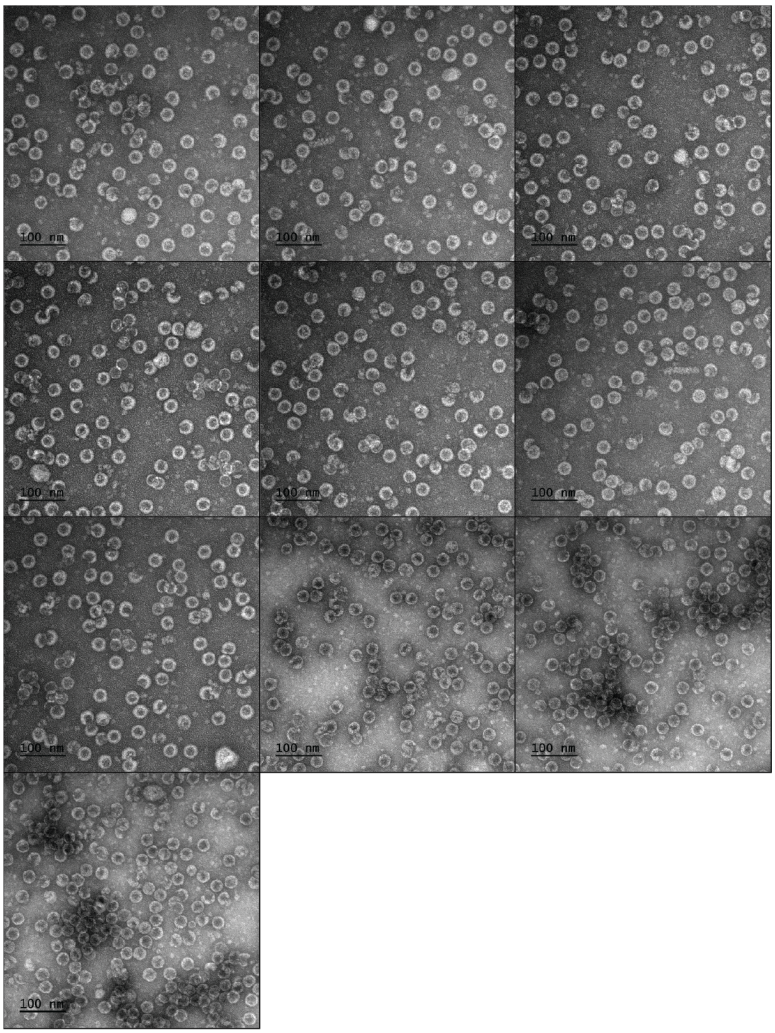


Figure 3.24: Transmission electron microscopy (TEM) images of MS2 N87C capsids.

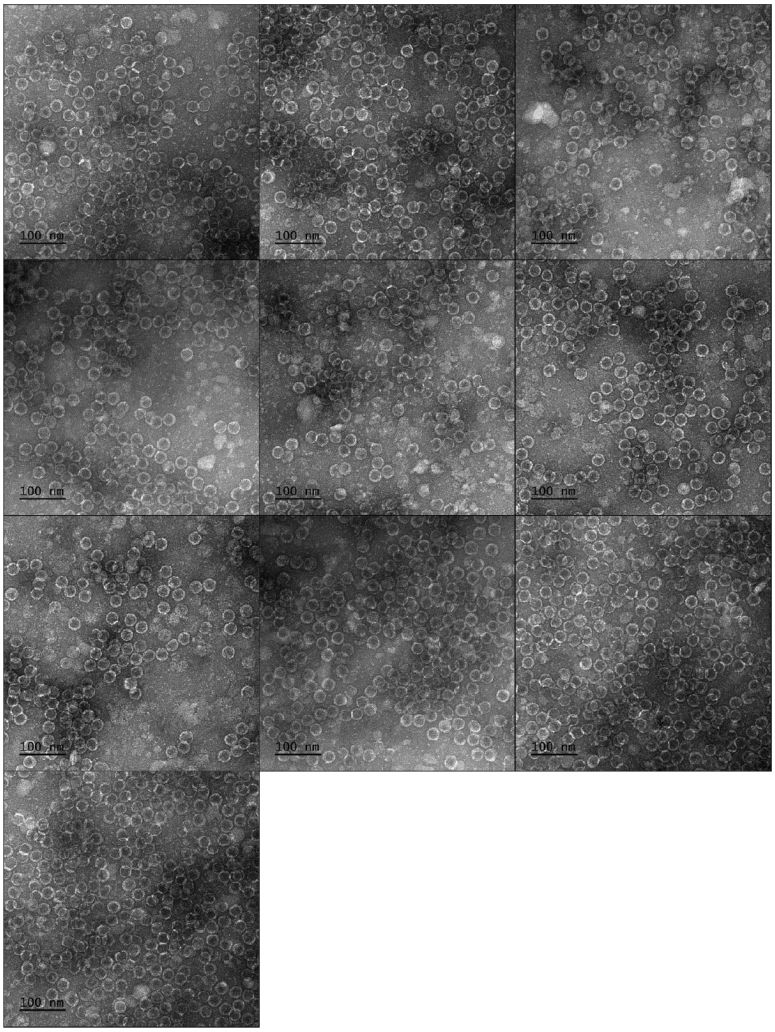


Figure 3.25: Transmission electron microscopy (TEM) images of MS2 T71R/N87C capsids.

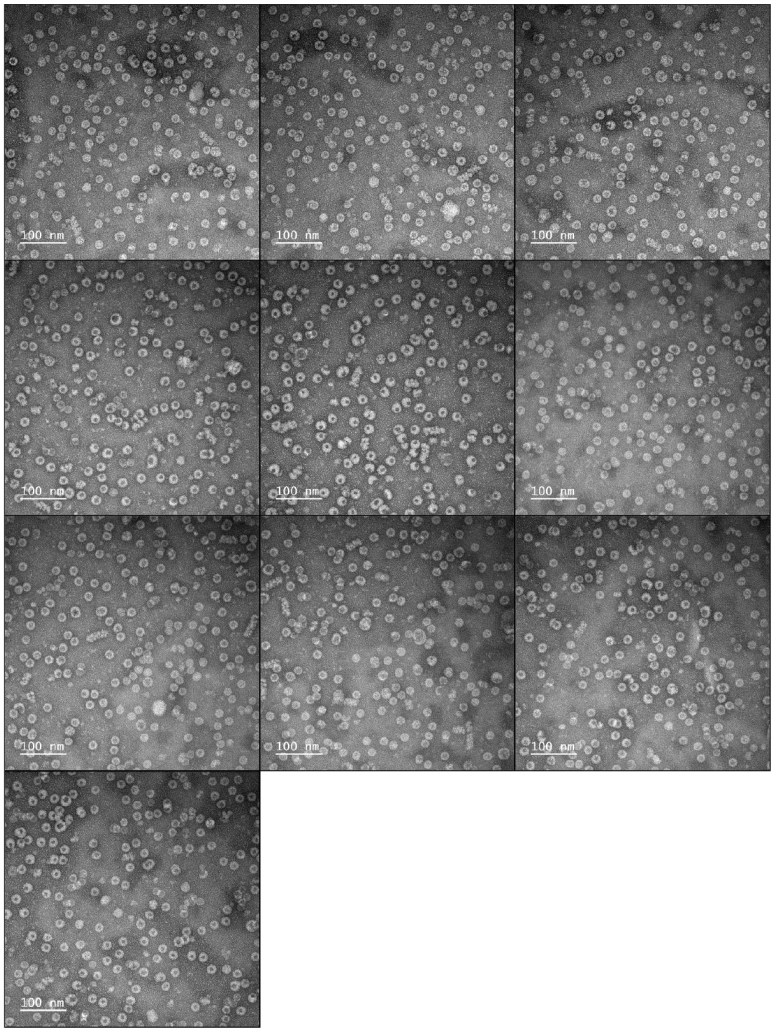


Figure 3.26: Transmission electron microscopy (TEM) images of MS2 S37P/N87C capsids.

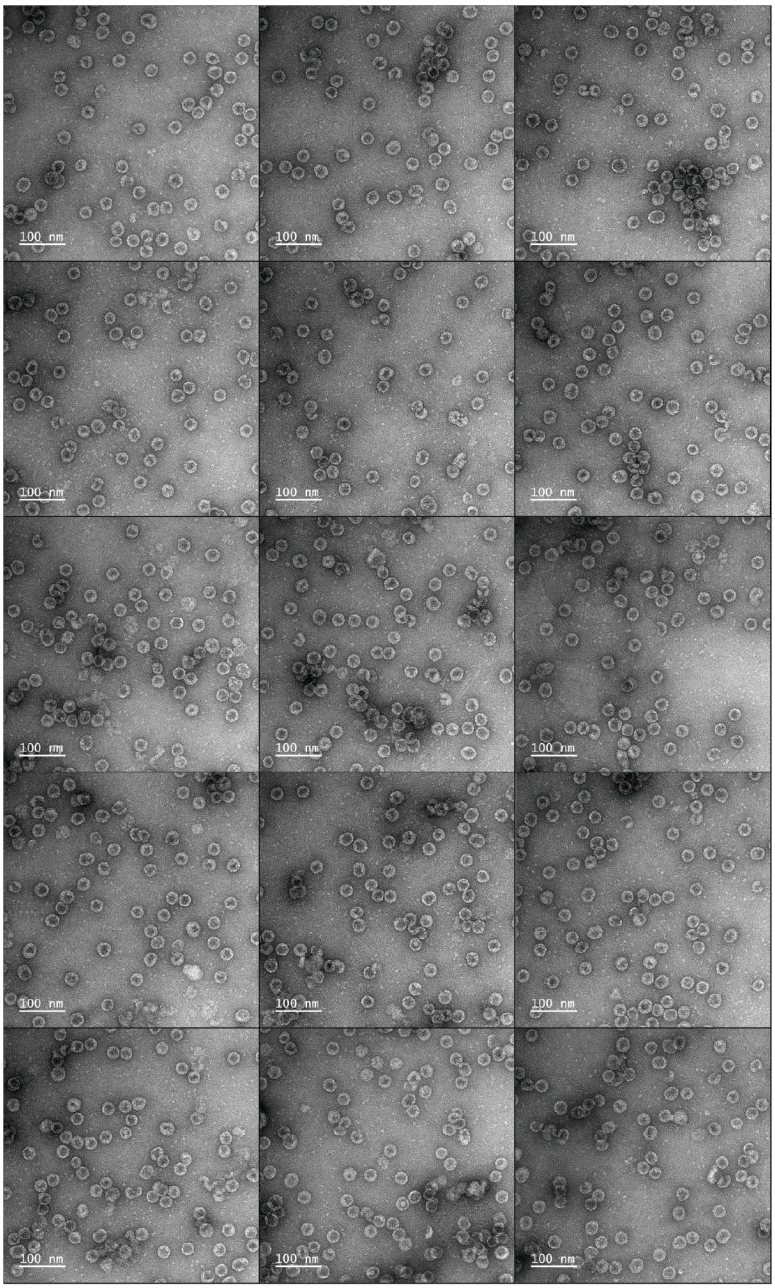


Figure 3.27: Transmission electron microscopy (TEM) images of MS2 G73R/N87C capsids.

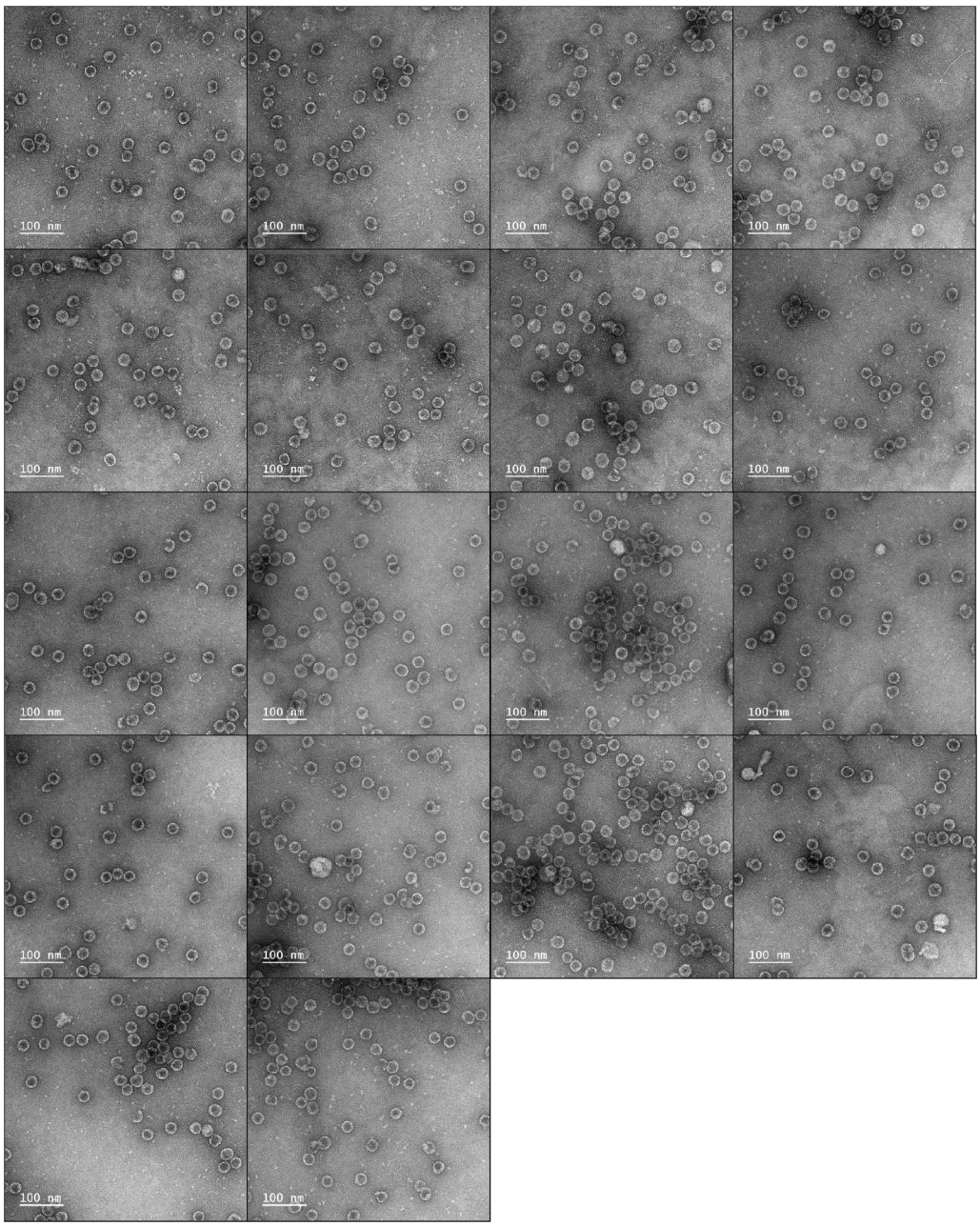


Figure 3.28: Transmission electron microscopy (TEM) images of MS2 G73K/N87C capsids.

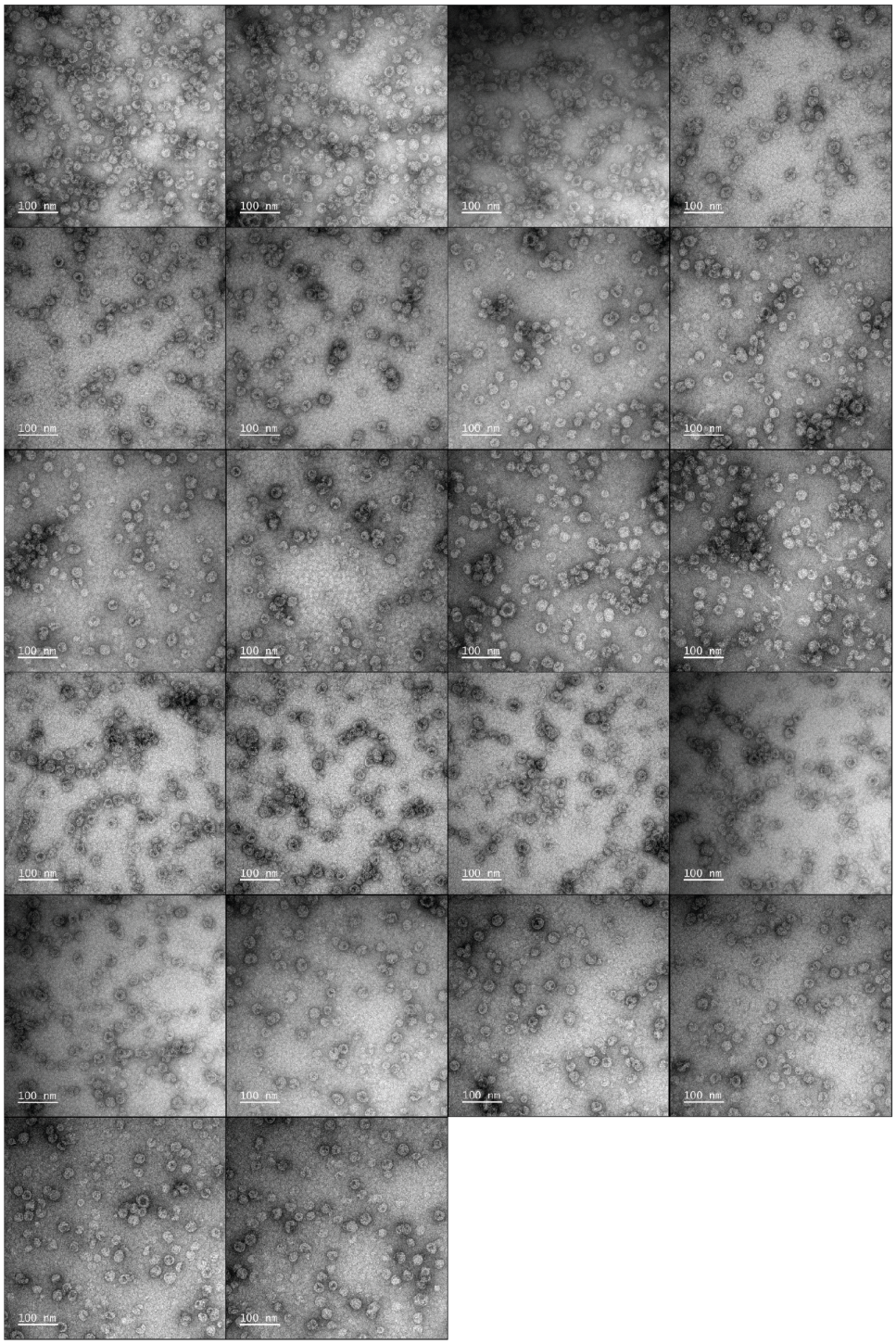


Figure 3.29: Transmission electron microscopy (TEM) images of S37P/T71K/G73R/N87C capsids.

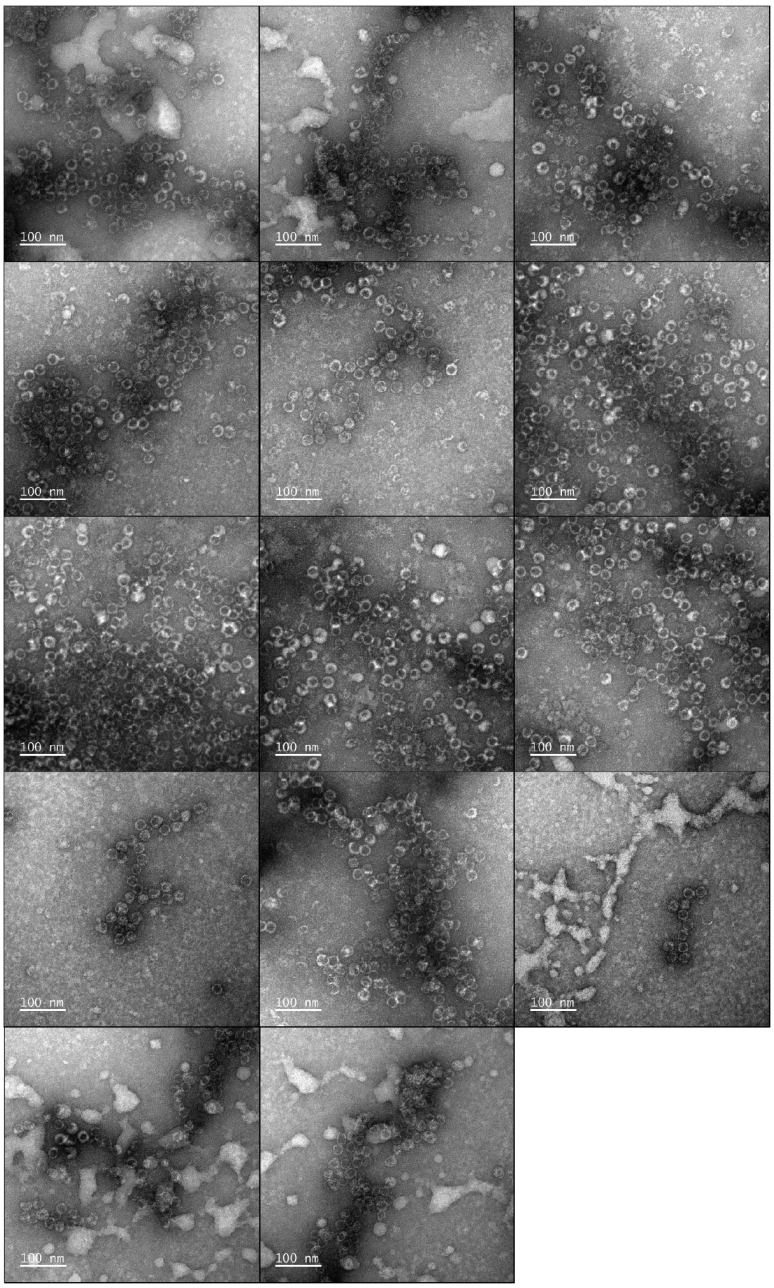


Figure 3.30: Transmission electron microscopy (TEM) images of S37P/T71R/G73K/N87C capsids.

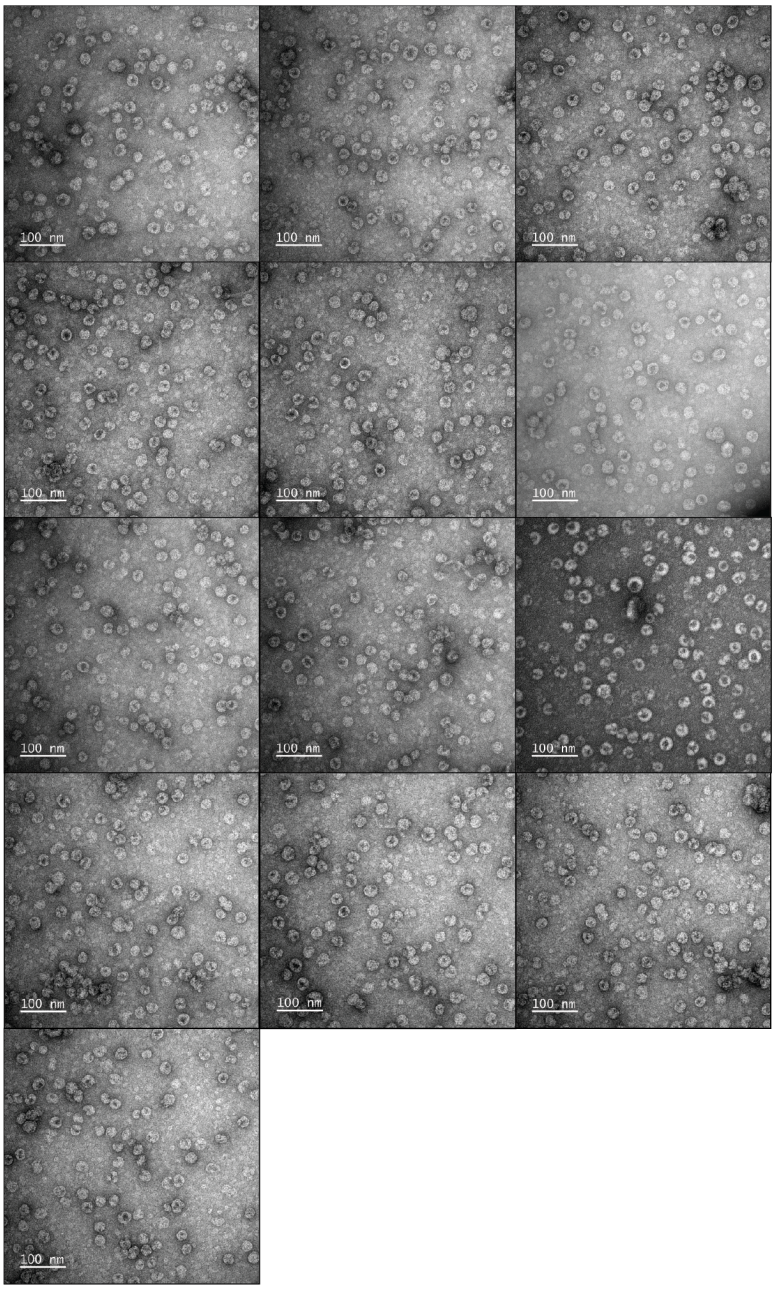


Figure 3.31: Transmission electron microscopy (TEM) images of S37P/G73R/N87C capsids.

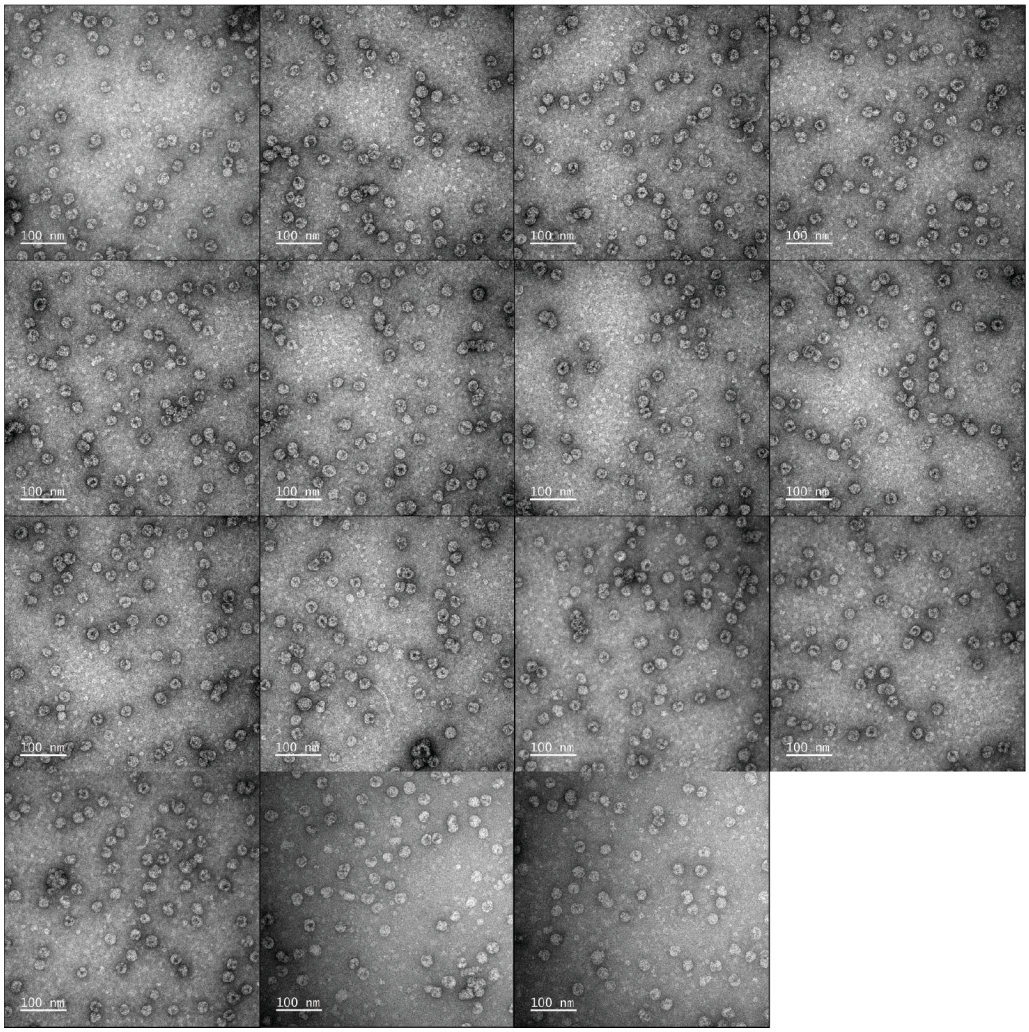


Figure 3.32: Transmission electron microscopy (TEM) images of S37P/G73K/N87C capsids.

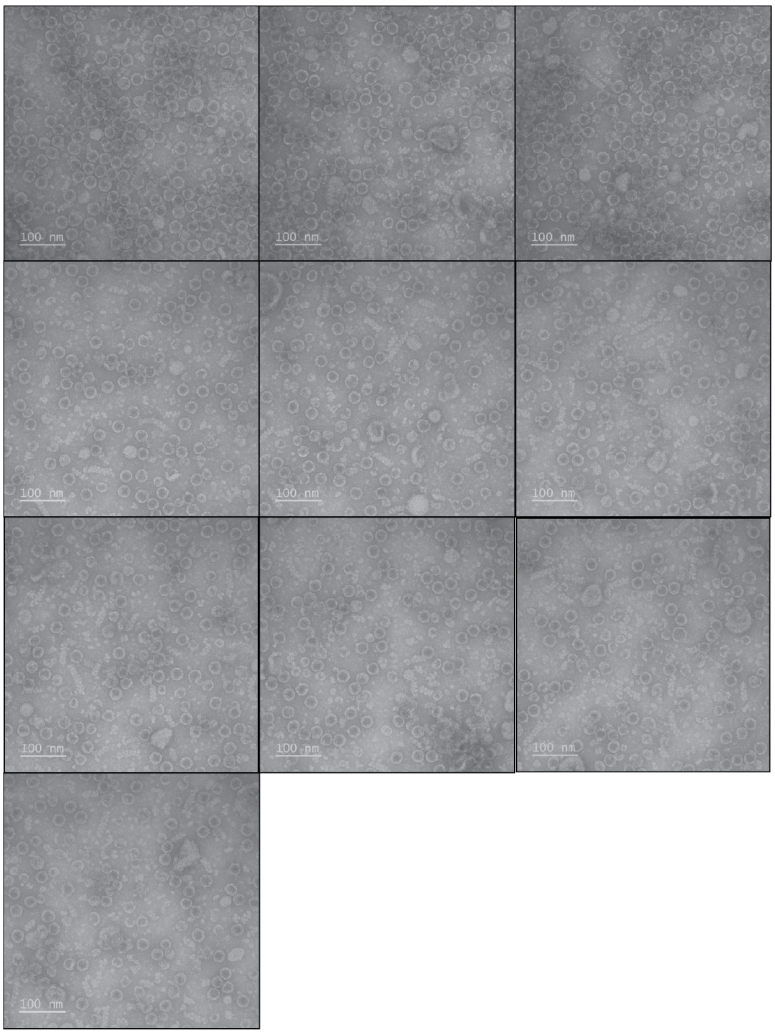


Figure 3.33: Transmission electron microscopy (TEM) images of T71K/N87C capsids.

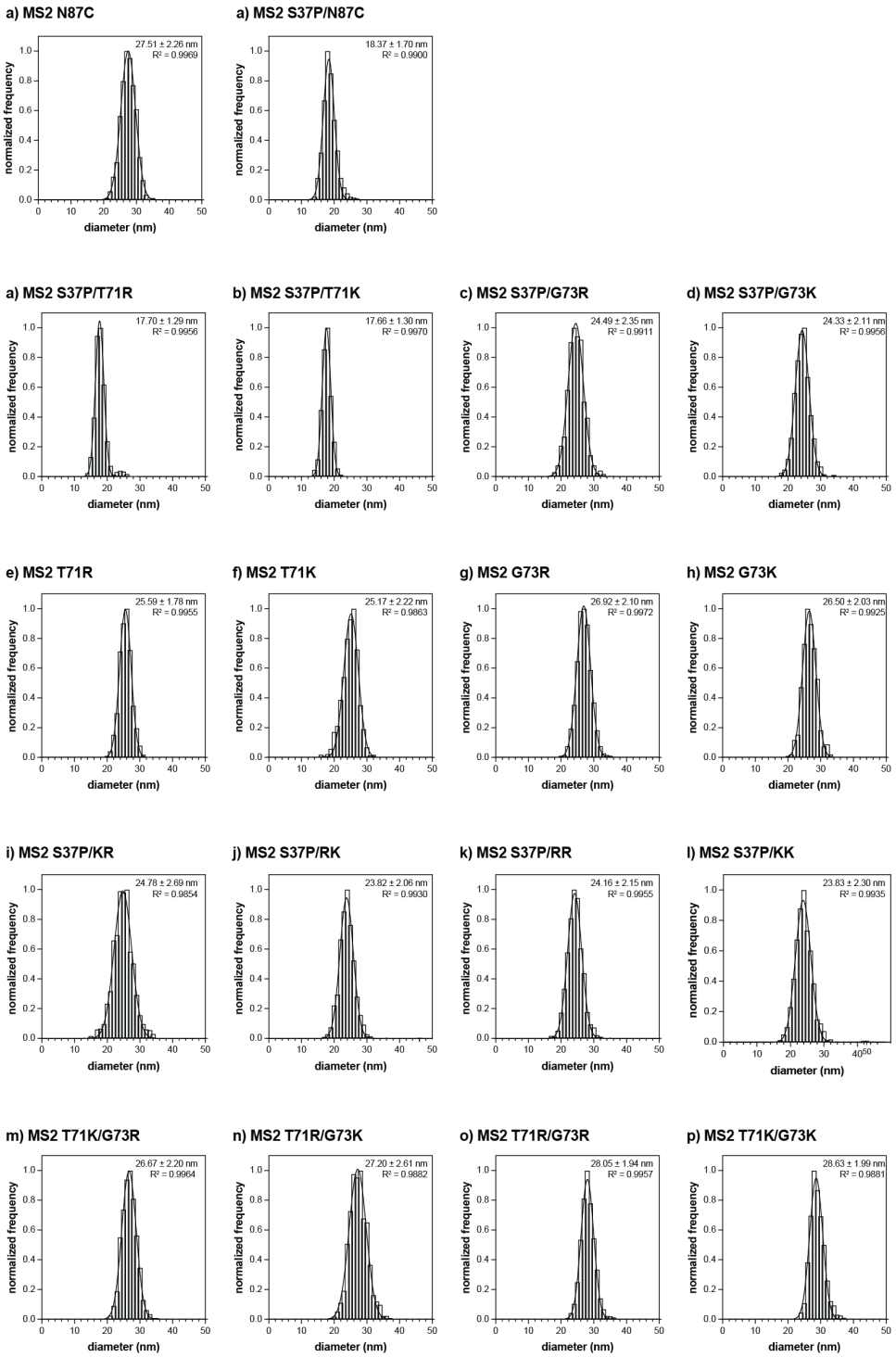


Figure 3.34: Normalized frequency distributions of MS2 variant capsid diameters as measured via transmission electron microscopy. The mean diameter, standard deviation and R^2 values are reported.

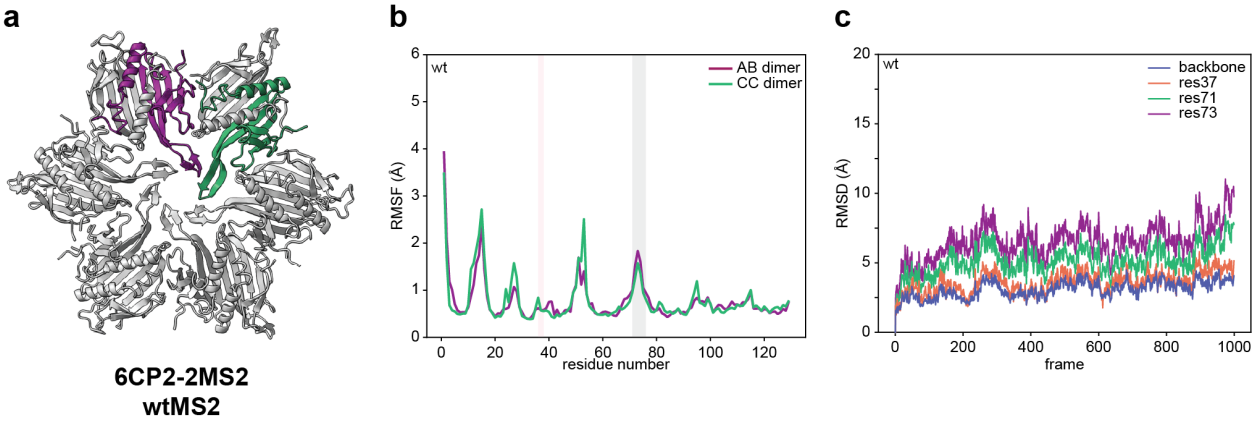


Figure 3.35: (A) wtMS2 6CP2-2MS2 input structure for molecular dynamics simulations. Inner facing AB dimer monomer (purple) and inner facing CC dimer monomer (green) are highlighted. **(B)** Graph showing root mean square fluctuation (RMSF) over the course of the trajectory. Residues 36-38 (pink) and 71-76 (grey) are highlighted. **(C)** Graph showing root mean square deviation (RMSD) over the course of the trajectory.

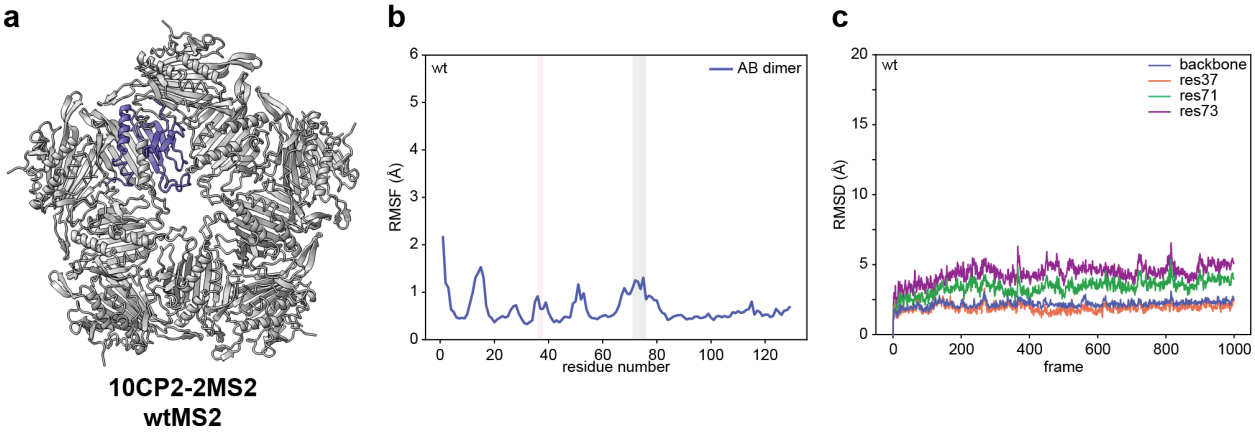


Figure 3.36: (A) wtMS2 10CP2-2MS2 input structure for molecular dynamics simulations. Inner facing AB dimer monomer (blue) is highlighted. **(B)** Graph showing root mean square fluctuation (RMSF) over the course of the trajectory. Residues 36-38 (pink) and 71-76 (grey) are highlighted. **(C)** Graph showing root mean square deviation (RMSD) over the course of the trajectory.

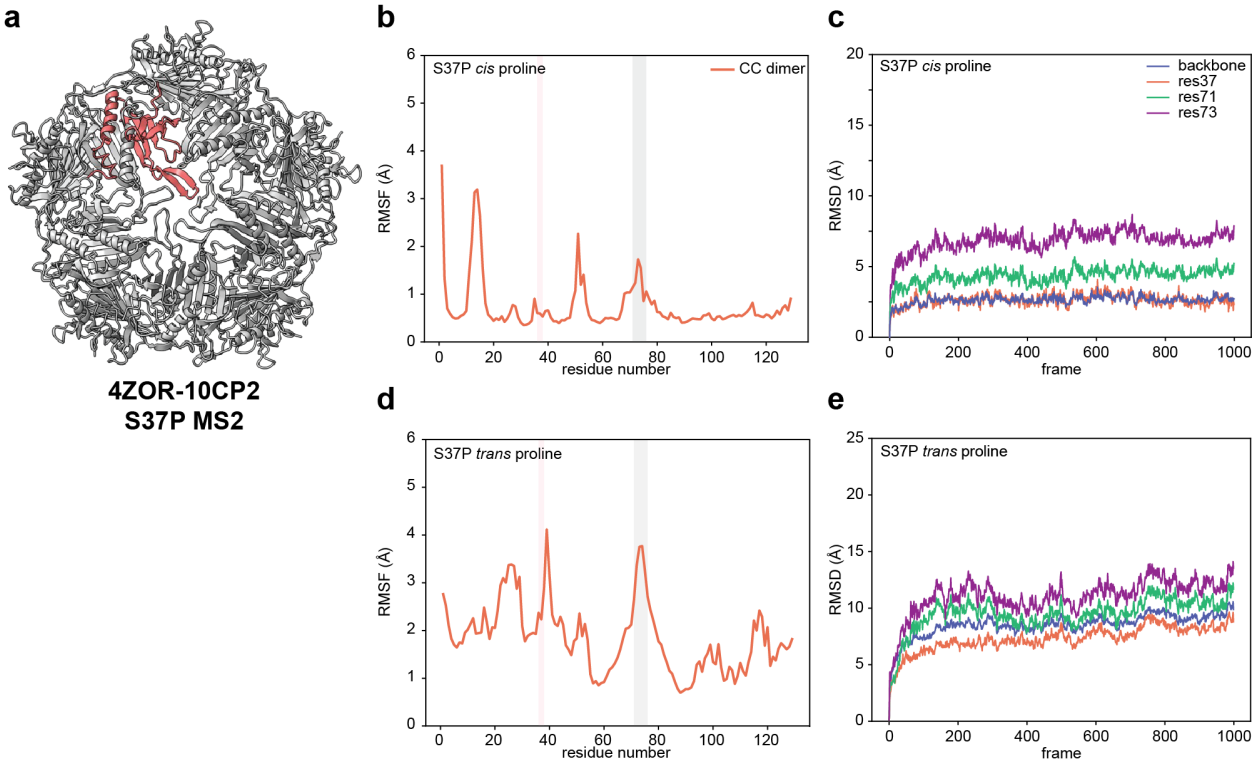


Figure 3.37: **(A)** S37P MS2 10CP2-4ZOR input structure for molecular dynamics simulations. Inner facing dimer monomer (orange) is highlighted. Graphs showing root mean square fluctuation (RMSF) over the course of the trajectory for *cis* **(B)** and *trans* **(D)** proline input structures. Residues 36-38 (pink) and 71-76 (grey) are highlighted. Graphs showing root mean square deviation (RMSD) over the course of the trajectory for *cis* **(C)** and *trans* **(E)** proline input structures.

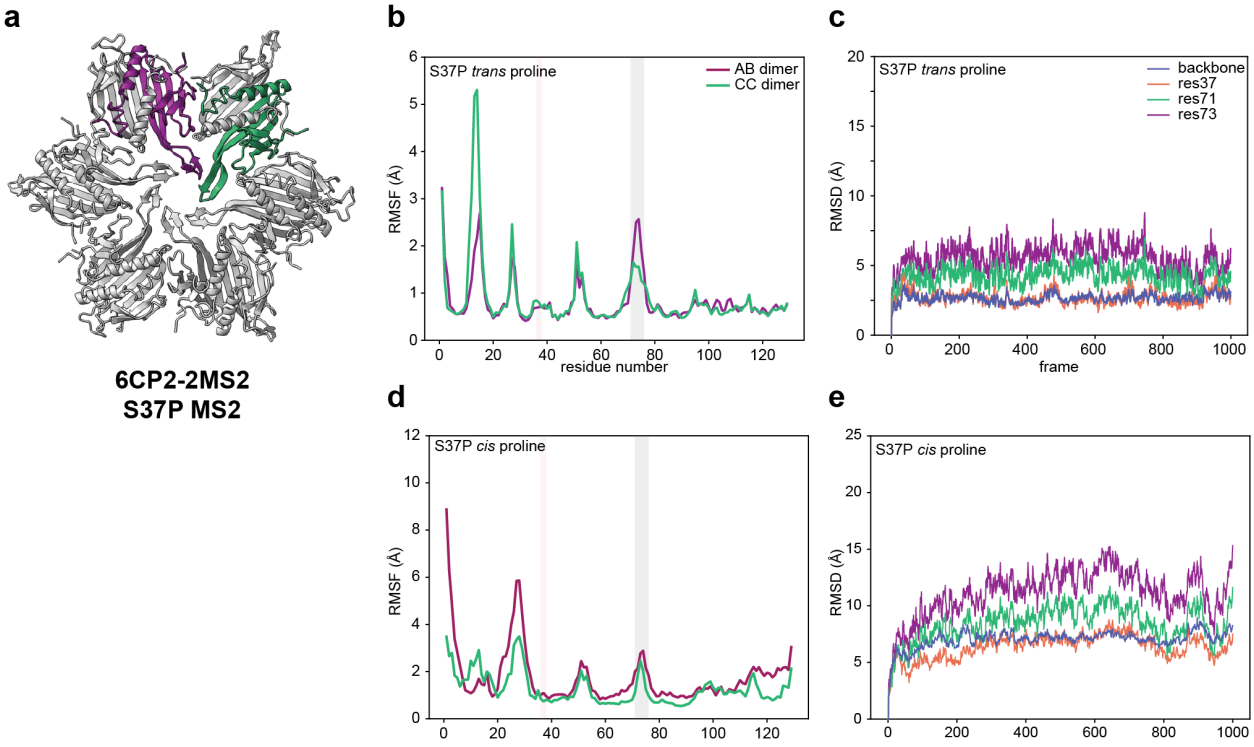


Figure 3.38: (A) S37P MS2 6CP2-2MS2 input structure for molecular dynamics simulations. Inner facing AB dimer monomer (purple) and inner facing CC dimer monomer (green) are highlighted. Graphs showing root mean square fluctuation (RMSF) over the course of the trajectory for *trans* **(B)** and *cis* **(D)** proline input structures. Residues 36-38 (pink) and 71-76 (grey) are highlighted. Graphs showing root mean square deviation (RMSD) over the course of the trajectory for *trans* **(C)** and *cis* **(E)** proline input structures.

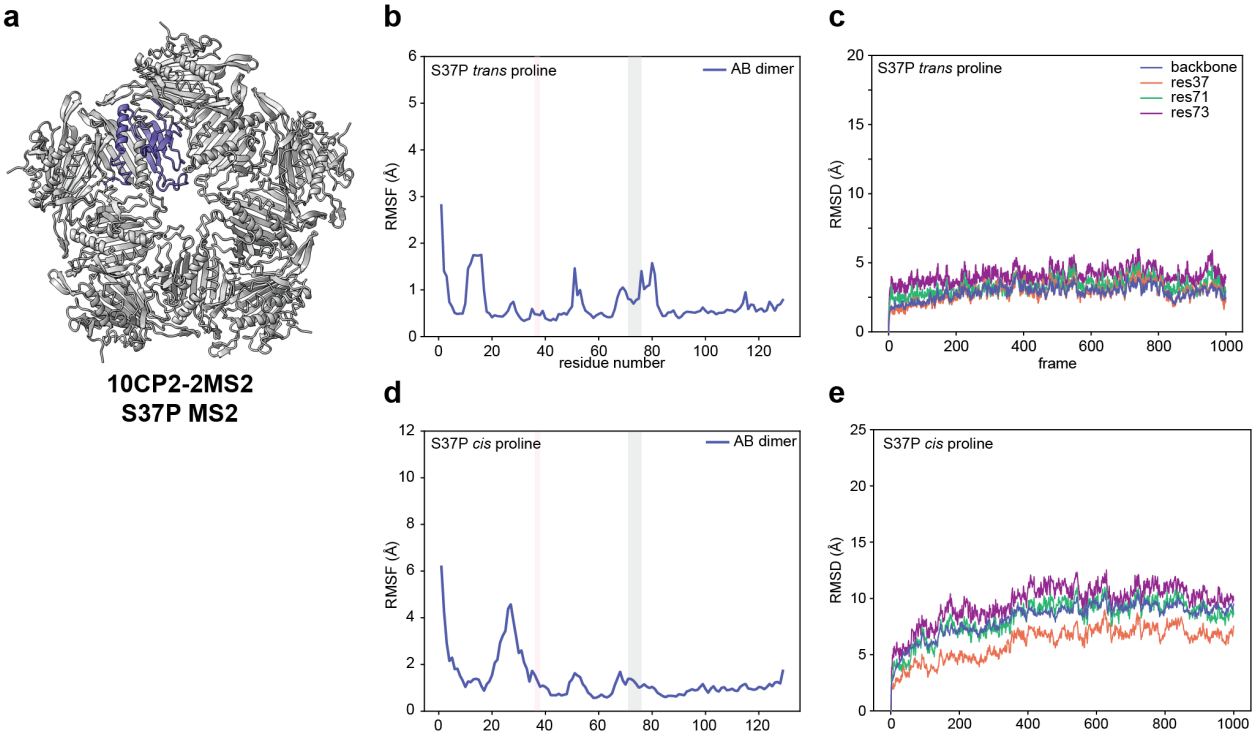


Figure 3.39: **(A)** S37P MS2 10CP2-2MS2 input structure for molecular dynamics simulations. Inner facing AB dimer monomer (blue) is highlighted. Graphs showing root mean square fluctuation (RMSF) over the course of the trajectory for *trans* **(B)** and *cis* **(D)** proline input structures. Residues 36-38 (pink) and 71-76 (grey) are highlighted. Graphs showing root mean square deviation (RMSD) over the course of the trajectory for *trans* **(C)** and *cis* **(E)** proline input structures.

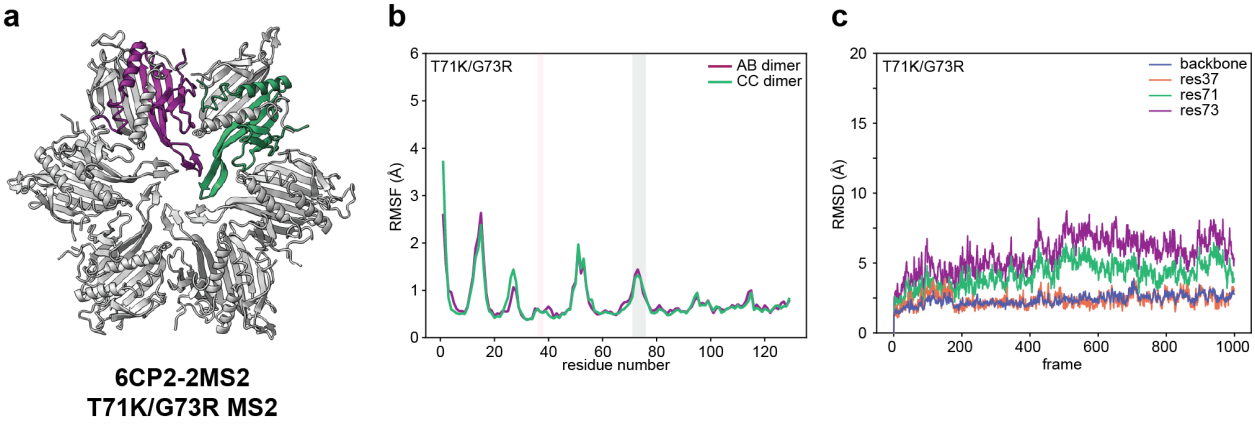


Figure 3.40: **(A)** T71K/G73R MS2 6CP2-2MS2 input structure for molecular dynamics simulations. Inner facing AB dimer monomer (purple) and inner facing CC dimer monomer (green) are highlighted. **(B)** Graph showing root mean square fluctuation (RMSF) over the course of the trajectory. Residues 36-38 (pink) and 71-76 (grey) are highlighted. **(C)** Graph showing root mean square deviation (RMSD) over the course of the trajectory.

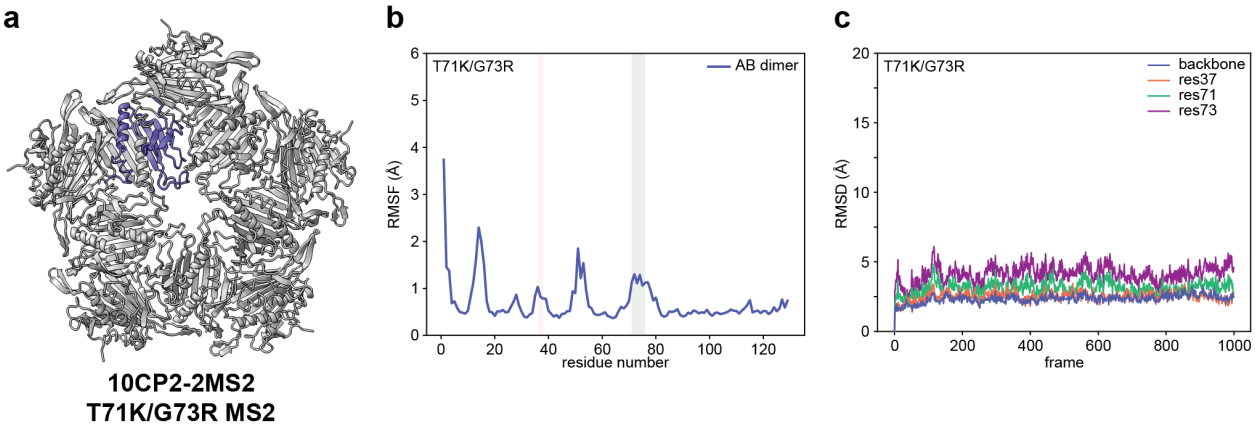


Figure 3.41: **(A)** T71K/G73R MS2 10CP2-2MS2 input structure for molecular dynamics simulations. Inner facing AB dimer monomer (blue) is highlighted. **(B)** Graph showing root mean square fluctuation (RMSF) over the course of the trajectory. Residues 36-38 (pink) and 71-76 (grey) are highlighted. **(C)** Graph showing root mean square deviation (RMSD) over the course of the trajectory.

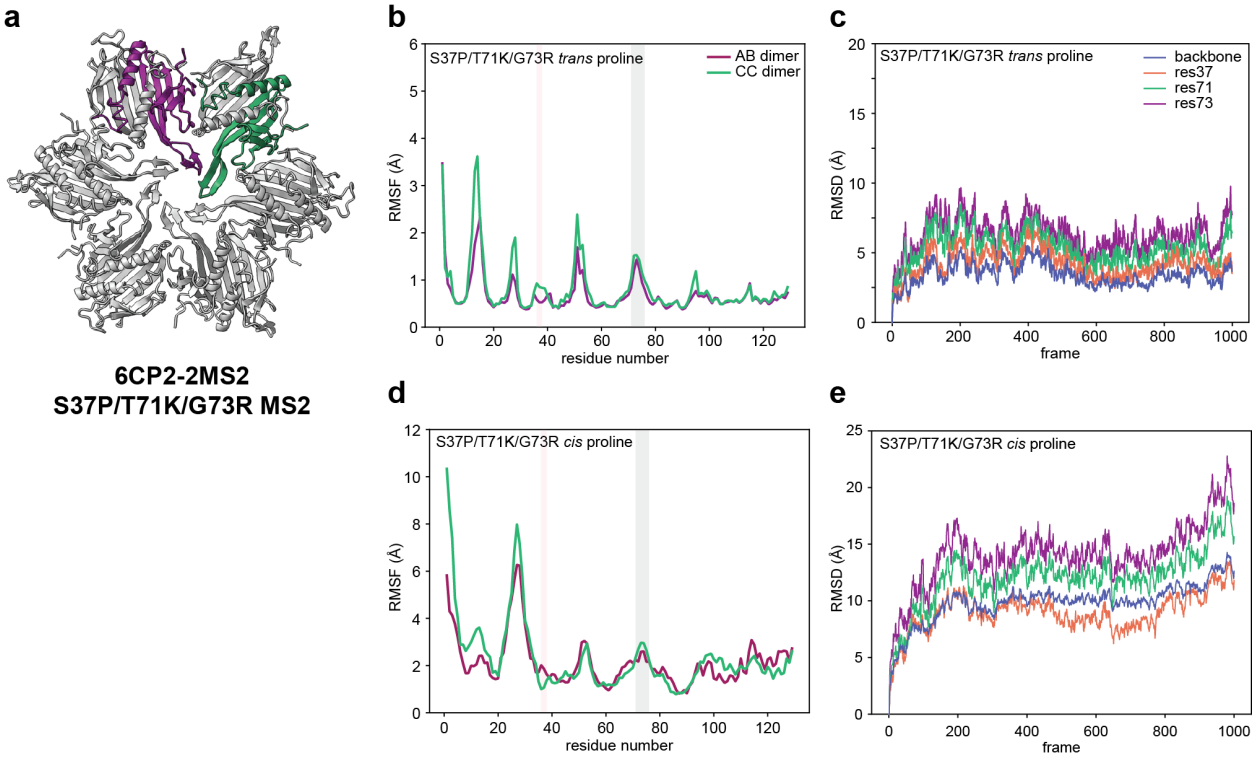


Figure 3.42: **(A)** S37P/T71K/G73R MS2 6CP2-2MS2 input structure for molecular dynamics simulations. Inner facing AB dimer monomer (purple) and inner facing CC dimer monomer (green) are highlighted. Graphs showing root mean square fluctuation (RMSF) over the course of the trajectory for *trans* **(B)** and *cis* **(D)** proline input structures. Residues 36-38 (pink) and 71-76 (grey) are highlighted. Graphs showing root mean square deviation (RMSD) over the course of the trajectory for *trans* **(C)** and *cis* **(E)** proline input structures.

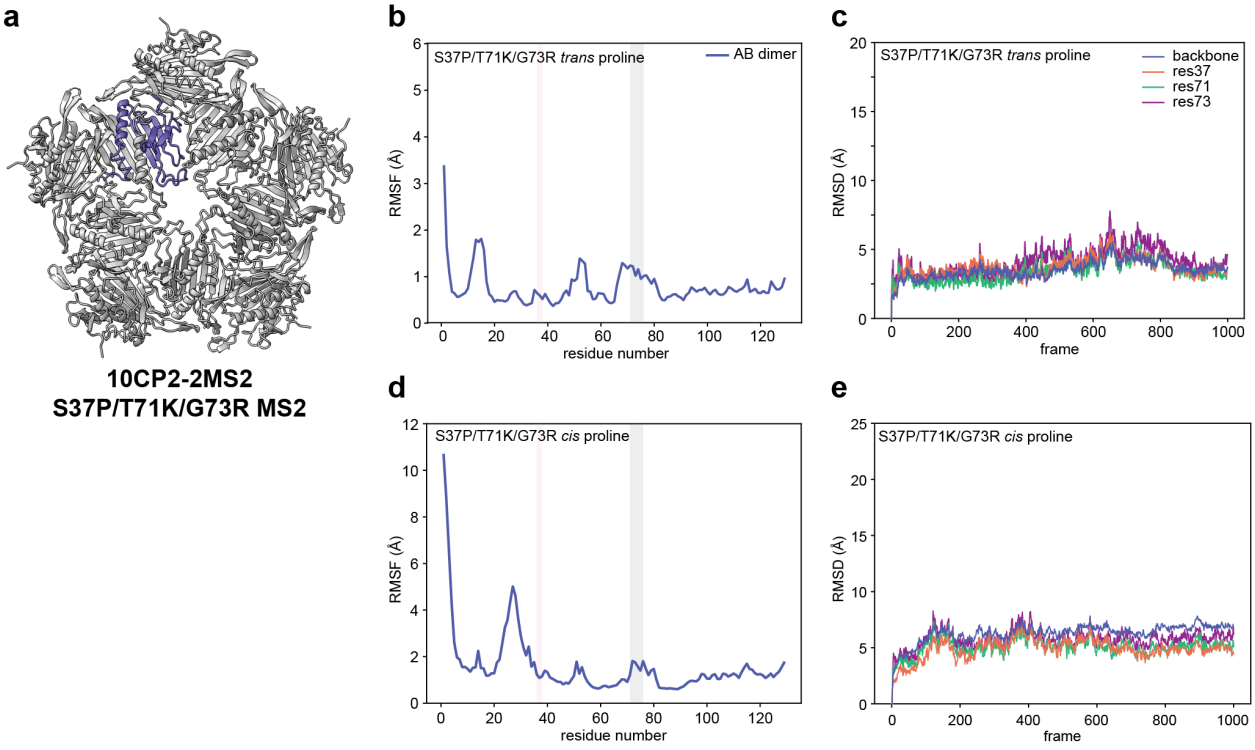


Figure 3.43: **(A)** S37P/T71K/G73R MS2 10CP2-2MS2 input structure for molecular dynamics simulations. Inner facing AB dimer monomer (blue) is highlighted. Graphs showing root mean square fluctuation (RMSF) over the course of the trajectory for *trans* **(B)** and *cis* **(D)** proline input structures. Residues 36-38 (pink) and 71-76 (grey) are highlighted. Graphs showing root mean square deviation (RMSD) over the course of the trajectory for *trans* **(C)** and *cis* **(E)** proline input structures.

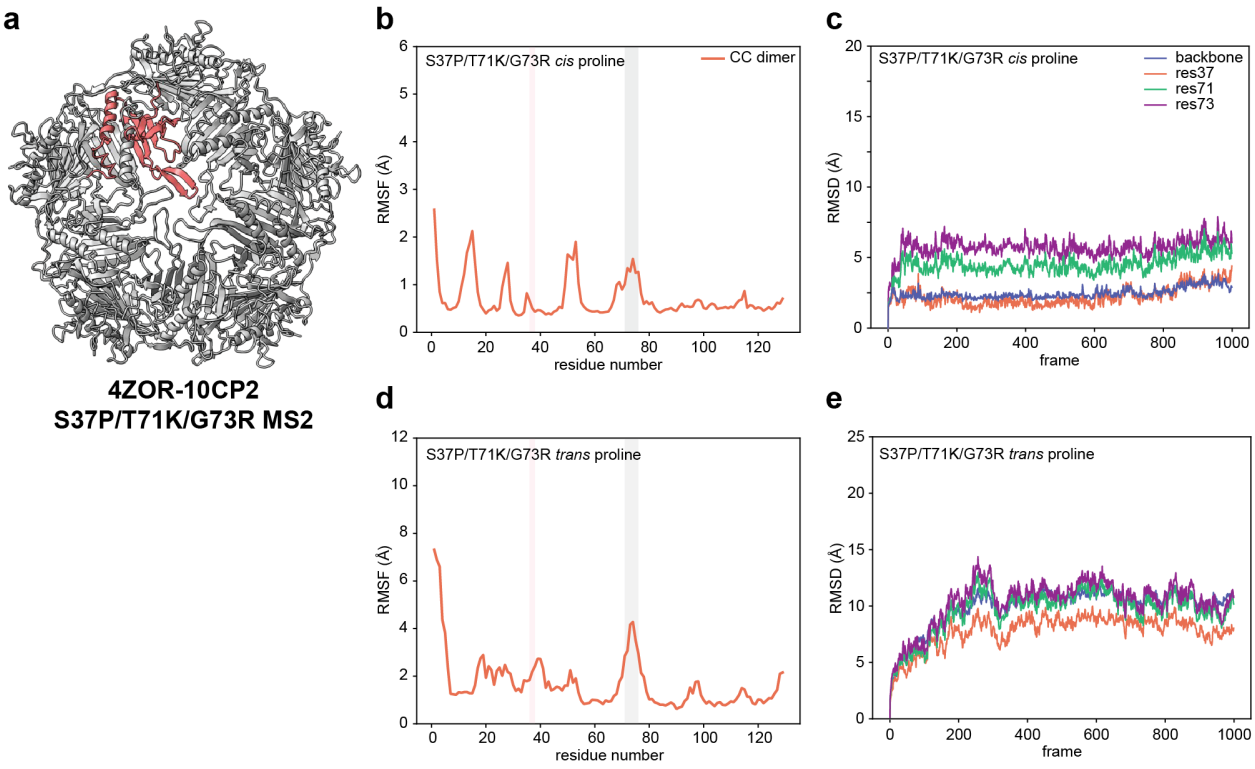


Figure 3.44: **(A)** S37P/T71K/G73R MS2 10CP2-4ZOR input structure for molecular dynamics simulations. Inner facing dimer monomer (orange) is highlighted. Graphs showing root mean square fluctuation (RMSF) over the course of the trajectory for *cis* **(B)** and *trans* **(D)** proline input structures. Residues 36-38 (pink) and 71-76 (grey) are highlighted. Graphs showing root mean square deviation (RMSD) over the course of the trajectory for *cis* **(C)** and *trans* **(E)** proline input structures.

Bibliography

(1) Louten, J. *Essential Human Virology* **2016**, 19–29.

(2) Crick, F. H. C.; Watson, J. D. *Nature* **1956**, *177*, Publisher: Nature Publishing Group, 473–475.

(3) Caspar, D. L.; Klug, A. *Cold Spring Harbor Symposia on Quantitative Biology* **1962**, *27*, 1–24.

(4) Twarock, R.; Luque, A. *Nature Communications* **2019**, *10*, Publisher: Nature Publishing Group, 4414.

(5) Li, H.-Y.; Han, J.-F.; Qin, C.-F.; Chen, R. *Vaccine* **2013**, *31*, 3281–3287.

(6) Rodríguez-Limas, W. A.; Tyo, K. E.; Nielsen, J.; Ramírez, O. T.; Palomares, L. A. *Microbial Cell Factories* **2011**, *10*, 33.

(7) Fernandes, F.; Teixeira, A. P.; Carinhas, N.; Carrondo, M. J.; Alves, P. M. *Expert Review of Vaccines* **2013**, *12*, 225–236.

(8) Scotti, N.; Rybicki, E. P. *Expert Review of Vaccines* **2013**, *12*, 211–224.

(9) Welsch, S.; Müller, B.; Kräusslich, H.-G. *Febs Letters* **2007**, *581*, 2089–2097.

(10) Mortola, E.; Roy, P. *FEBS letters* **2004**, *576*, 174–178.

(11) Banskota, S.; Raguram, A.; Suh, S.; Du, S. W.; Davis, J. R.; Choi, E. H.; Wang, X.; Nielsen, S. C.; Newby, G. A.; Randolph, P. B.; Osborn, M. J.; Musunuru, K.; Palczewski, K.; Liu, D. R. *Cell* **2022**, *185*, 250–265.e16.

(12) Hamilton, J. R.; Tsuchida, C. A.; Nguyen, D. N.; Shy, B. R.; McGarrigle, E. R.; Sandoval Espinoza, C. R.; Carr, D.; Blaeschke, F.; Marson, A.; Doudna, J. A. *Cell Reports* **2021**, *35*, 109207.

(13) Hamilton, J. R.; Chen, E.; Perez, B. S.; Sandoval Espinoza, C. R.; Kang, M. H.; Trinidad, M.; Ngo, W.; Doudna, J. A. *Nature Biotechnology* **2024**, Publisher: Nature Publishing Group, 1–9.

(14) An, M.; Raguram, A.; Du, S. W.; Banskota, S.; Davis, J. R.; Newby, G. A.; Chen, P. Z.; Palczewski, K.; Liu, D. R. *Nature Biotechnology* **2024**, Publisher: Nature Publishing Group, 1–12.

(15) Zhang, W.; Cao, S.; Martin, J. L.; Mueller, J. D.; Mansky, L. M.; Zhang, W.; Cao, S.; Martin, J. L.; Mueller, J. D.; Mansky, L. M. *AIMS Biophysics* **2015**, *2*, 343–369.

(16) Fuenmayor, J.; Gòdia, F.; Cervera, L. *New Biotechnology* **2017**, *39*, 174–180.

(17) Huang, X.; Wang, X.; Zhang, J.; Xia, N.; Zhao, Q. *npj Vaccines* **2017**, *2*, Publisher: Nature Publishing Group, 1–9.

(18) Keating, G. M.; Noble, S. *Drugs* **2003**, *63*, 1021–1051.

(19) Block, S. L.; Nolan, T.; Sattler, C.; Barr, E.; Giacoletti, K. E. D.; Marchant, C. D.; Castellsagué, X.; Rusche, S. A.; Lukac, S.; Bryan, J. T.; Cavanaugh, P. F.; Reisinger, K. S.; Protocol 016 Study Group *Pediatrics* **2006**, *118*, 2135–2145.

(20) Syed, Y. Y. *Drugs & Therapy Perspectives* **2022**, *38*, 373–381.

(21) Monie, A.; Hung, C.-F.; Roden, R.; Wu, T.-C. *Biologics: Targets and Therapy* **2008**, *2*, 107–113.

(22) Cox, M. M. *Vaccine* **2012**, *30*, 1759–1766.

(23) Deng, M.-p.; Hu, Z.-h.; Wang, H.-l.; Deng, F. *Virologica Sinica* **2012**, *27*, 145–153.

(24) Lai, C.-C.; Cheng, Y.-C.; Chen, P.-W.; Lin, T.-H.; Tzeng, T.-T.; Lu, C.-C.; Lee, M.-S.; Hu, A. Y.-C. *Journal of Biological Engineering* **2019**, *13*, 78.

(25) Rajaram, S.; Wojcik, R.; Moore, C.; Ortiz de Lejarazu, R.; de Lusignan, S.; Montomoli, E.; Rossi, A.; Pérez-Rubio, A.; Trilla, A.; Baldo, V.; Jandhyala, R.; Kassianos, G. *Vaccine* **2020**, *38*, 6047–6056.

(26) O'Flaherty, R.; Bergin, A.; Flampouri, E.; Mota, L. M.; Obaidi, I.; Quigley, A.; Xie, Y.; Butler, M. *Biotechnology Advances* **2020**, *43*, 107552.

(27) Nooraei, S.; Bahrulolum, H.; Hoseini, Z. S.; Katalani, C.; Hajizade, A.; Easton, A. J.; Ahmadian, G. *Journal of Nanobiotechnology* **2021**, *19*, 59.

(28) Vicente, T.; Roldão, A.; Peixoto, C.; Carrondo, M. J. T.; Alves, P. M. *Journal of Invertebrate Pathology* **2011**, *107 Suppl*, S42–48.

(29) Mohsen, M. O.; Zha, L.; Cabral-Miranda, G.; Bachmann, M. F. *Seminars in Immunology* **2017**, *34*, 123–132.

(30) Chan, H. L.-Y.; Thompson, A.; Martinot-Peignoux, M.; Piratvisuth, T.; Cornberg, M.; Brunetto, M. R.; Tillmann, H. L.; Kao, J.-H.; Jia, J.-D.; Wedemeyer, H.; Locarnini, S.; Janssen, H. L. A.; Marcellin, P. *Journal of Hepatology* **2011**, *55*, 1121–1131.

(31) Shouval, D.; Roggendorf, H.; Roggendorf, M. *Medical Microbiology and Immunology* **2015**, *204*, 57–68.

(32) Zucker, R. M.; Ortenzio, J. N. R.; Boyes, W. K. *Cytometry Part A* **2016**, *89*, 169–183.

(33) Mohsen, M. O.; Bachmann, M. F. *Cellular & Molecular Immunology* **2022**, *19*, Publisher: Nature Publishing Group, 993–1011.

(34) Pipeline, Icosavax `https://icosavax.com/pipeline/` (accessed 03/18/2024).

(35) Hepatitis E vaccines `https://www.who.int` (accessed 04/15/2024).

(36) Laurens, M. B. *Human Vaccines & Immunotherapeutics* **2019**, *16*, 480–489.

(37) Datoo, M. S. et al. *The Lancet* **2024**, *403*, Publisher: Elsevier, 533–544.

(38) Valentine, R. C.; Strand, M. *Science* **1965**, *148*, Publisher: American Association for the Advancement of Science, 511–513.

(39) Chang, J.-Y.; Gorzelnik, K. V.; Thongchol, J.; Zhang, J. *Viruses* **2022**, *14*, 225.

(40) Garrido, N. d. M.; Crone, M. A.; Ramlaul, K.; Simpson, P. A.; Freemont, P. S.; Aylett, C. H. S. *Molecular Microbiology* **2020**, *113*, 143–152.

(41) Biela, A. P.; Naskalska, A.; Fatehi, F.; Twarock, R.; Heddle, J. G. *Communications Materials* **2022**, *3*, 7.

(42) Hartman, E. C.; Tullman-Ercek, D. *Current Opinion in Systems Biology* **2019**, *14*, 25–31.

(43) Al-Mawsawi, L. Q.; Wu, N. C.; Olson, C. A.; Shi, V. C.; Qi, H.; Zheng, X.; Wu, T.-T.; Sun, R. *Retrovirology* **2014**, *11*, 124.

(44) Ferguson, A. L.; Mann, J. K.; Omarjee, S.; Ndung'u, T.; Walker, B. D.; Chakraborty, A. K. *Immunity* **2013**, *38*, 606–617.

(45) Lauring, A. S.; Andino, R. *Journal of Virology* **2011**, *85*, Publisher: American Society for Microbiology, 3780–3791.

(46) Visher, E.; Whitefield, S. E.; McCrone, J. T.; Fitzsimmons, W.; Lauring, A. S. *PLOS Pathogens* **2016**, *12*, Publisher: Public Library of Science, e1005856.

(47) Betancourt, A. J. *Genetics* **2009**, *181*, 1535–1544.

(48) Acevedo, A.; Brodsky, L.; Andino, R. *Nature* **2014**, *505*, Publisher: Nature Publishing Group, 686–690.

(49) Hartman, E. C.; Lobba, M. J.; Favor, A. H.; Robinson, S. A.; Francis, M. B.; Tullman-Ercek, D. *Biochemistry* **2019**, *58*, Publisher: American Chemical Society, 1527–1538.

(50) Brauer, D. D.; Hartman, E. C.; Bader, D. L. V.; Merz, Z. N.; Tullman-Ercek, D.; Francis, M. B. *Journal of the American Chemical Society* **2019**, *141*, Publisher: American Chemical Society, 3875–3884.

(51) Robinson, S. A.; Hartman, E. C.; Ikwuagwu, B. C.; Francis, M. B.; Tullman-Ercek, D. *Biomacromolecules* **2020**, *21*, Publisher: American Chemical Society, 4194–4204.

(52) Asensio, M. A.; Morella, N. M.; Jakobson, C. M.; Hartman, E. C.; Glasgow, J. E.; Sankaran, B.; Zwart, P. H.; Tullman-Ercek, D. *Nano Letters* **2016**, *16*, Publisher: American Chemical Society, 5944–5950.

(53) Brauer, D. D.; Santiago, C. B.; Merz, Z. N.; McCarthy, E.; Tullman-Ercek, D.; Francis, M. B. Comprehensive Fitness Landscape of a Multi-Geometry Protein Capsid Informs Machine Learning Models of Assembly, Pages: 2021.12.21.473721 Section: New Results, 2021.

(54) Ikwuagwu, B.; Hartman, E.; Mills, C. E.; Tullman-Ercek, D. *Virology* **2023**, *579*, 137–147.

(55) Zhao, L.; Kopylov, M.; Potter, C. S.; Carragher, B.; Finn, M. G. *ACS Nano* **2019**, *13*, Publisher: American Chemical Society, 4443–4454.

(56) Brown, S. D.; Fiedler, J. D.; Finn, M. G. *Biochemistry* **2009**, *48*, Publisher: American Chemical Society, 11155–11157.

(57) Pokorski, J. K.; Hovlid, M. L.; Finn, M. G. *ChemBioChem* **2011**, *12*, 2441–2447.

(58) Chackerian, B.; Caldeira, J. d. C.; Peabody, J.; Peabody, D. S. *Journal of Molecular Biology* **2011**, *409*, 225–237.

(59) Crossey, E.; Frietze, K.; Narum, D. L.; Peabody, D. S.; Chackerian, B. *PLOS ONE* **2015**, *10*, Publisher: Public Library of Science, e0132560.

(60) Frietze, K. M.; Roden, R. B.; Lee, J.-H.; Shi, Y.; Peabody, D. S.; Chackerian, B. *Cancer Immunology Research* **2016**, *4*, 157–164.

(61) Seitz, I.; Saarinen, S.; Kumpula, E.-P.; McNeale, D.; Anaya-Plaza, E.; Lampinen, V.; Hytönen, V. P.; Sainsbury, F.; Cornelissen, J. J. L. M.; Linko, V.; Huiskonen, J. T.; Kostiainen, M. A. *Nature Nanotechnology* **2023**, *18*, Publisher: Nature Publishing Group, 1205–1212.

(62) Zhao, Z.; Wang, J. C.-Y.; Zhang, M.; Lyktey, N. A.; Jarrold, M. F.; Jacobson, S. C.; Zlotnick, A. *Nature Communications* **2021**, *12*, Publisher: Nature Publishing Group, 589.

(63) Giessen, T. W. *Annual Review of Biochemistry* **2022**, *91*, Publisher: Annual Reviews, 353–380.

(64) Planamente, S.; Frank, S. *Biochemical Society Transactions* **2019**, *47*, 765–777.

(65) Jutz, G.; van Rijn, P.; Santos Miranda, B.; Böker, A. *Chemical Reviews* **2015**, *115*, Publisher: American Chemical Society, 1653–1701.

(66) Azuma, Y.; Edwardson, T. G. W.; Hilvert, D. *Chemical Society Reviews* **2018**, *47*, Publisher: The Royal Society of Chemistry, 3543–3557.

(67) Tetter, S.; Terasaka, N.; Steinauer, A.; Bingham, R. J.; Clark, S.; Scott, A. J. P.; Patel, N.; Leibundgut, M.; Wroblewski, E.; Ban, N.; Stockley, P. G.; Twarock, R.; Hilvert, D. *Science* **2021**, *372*, 1220–1224.

(68) Terasaka, N.; Azuma, Y.; Hilvert, D. *Proceedings of the National Academy of Sciences* **2018**, *115*, Publisher: Proceedings of the National Academy of Sciences, 5432–5437.

(69) Kwon, S.; Giessen, T. W. *ACS Synthetic Biology* **2022**, *11*, Publisher: American Chemical Society, 3504–3515.

(70) Hsia, Y.; Bale, J. B.; Gonen, S.; Shi, D.; Sheffler, W.; Fong, K. K.; Nattermann, U.; Xu, C.; Huang, P.-S.; Ravichandran, R.; Yi, S.; Davis, T. N.; Gonen, T.; King, N. P.; Baker, D. *Nature* **2016**, *535*, 136–139.

(71) Yang, E. C. et al. Computational design of non-porous, pH-responsive antibody nanoparticles, Pages: 2023.04.17.537263 Section: New Results, 2023.

(72) De Haas, R. J.; Brunette, N.; Goodson, A.; Dauparas, J.; Yi, S. Y.; Yang, E. C.; Dowling, Q.; Nguyen, H.; Kang, A.; Bera, A. K.; Sankaran, B.; de Vries, R.; Baker, D.; King, N. P. *Proceedings of the National Academy of Sciences* **2024**, *121*, Publisher: Proceedings of the National Academy of Sciences, e2314646121.

(73) Dowling, Q. M.; Park, Y.-J.; Gerstenmaier, N.; Yang, E. C.; Wargacki, A.; Hsia, Y.; Fries, C. N.; Ravichandran, R.; Walkey, C.; Burrell, A.; Veesler, D.; Baker, D.; King, N. P. Hierarchical design of pseudosymmetric protein nanoparticles, Pages: 2023.06.16.545393 Section: New Results, 2023.

(74) Butterfield, G. L.; Lajoie, M. J.; Gustafson, H. H.; Sellers, D. L.; Nattermann, U.; Ellis, D.; Bale, J. B.; Ke, S.; Lenz, G. H.; Yehdego, A.; Ravichandran, R.; Pun, S. H.; King, N. P.; Baker, D. *Nature* **2017**, *552*, Publisher: Nature Publishing Group, 415–420.

(75) Smith, M. T.; Hawes, A. K.; Bundy, B. C. *Current Opinion in Biotechnology* **2013**, *24*, 620–626.

(76) McKay, C. S.; Finn, M. G. *Chemistry & Biology* **2014**, *21*, 1075–1101.

(77) Tilley, S. D.; Joshi, N. S.; Francis, M. B. In *Wiley Encyclopedia of Chemical Biology*; John Wiley & Sons, Ltd: 2008, pp 1–16.

(78) Marmelstein, A. M.; Lobba, M. J.; Mogilevsky, C. S.; Maza, J. C.; Brauer, D. D.; Francis, M. B. *Journal of the American Chemical Society* **2020**, *142*, Publisher: American Chemical Society, 5078–5086.

(79) Maza, J. C.; Bader, D. L. V.; Xiao, L.; Marmelstein, A. M.; Brauer, D. D.; ElSohly, A. M.; Smith, M. J.; Krska, S. W.; Parish, C. A.; Francis, M. B. *Journal of the American Chemical Society* **2019**, *141*, Publisher: American Chemical Society, 3885–3892.

(80) Mogilevsky, C. S.; Lobba, M. J.; Brauer, D. D.; Marmelstein, A. M.; Maza, J. C.; Gleason, J. M.; Doudna, J. A.; Francis, M. B. *Journal of the American Chemical Society* **2021**, *143*, Publisher: American Chemical Society, 13538–13547.

(81) Tong, G. J.; Hsiao, S. C.; Carrico, Z. M.; Francis, M. B. *Journal of the American Chemical Society* **2009**, *131*, Publisher: American Chemical Society, 11174–11178.

(82) ElSohly, A. M.; Netirojjanakul, C.; Aanei, I. L.; Jager, A.; Bendall, S. C.; Farkas, M. E.; Nolan, G. P.; Francis, M. B. *Bioconjugate chemistry* **2015**, *26*, 1590–1596.

(83) Brune, K. D.; Leneghan, D. B.; Brian, I. J.; Ishizuka, A. S.; Bachmann, M. F.; Draper, S. J.; Biswas, S.; Howarth, M. *Scientific Reports* **2016**, *6*, Publisher: Nature Publishing Group, 19234.

(84) Hartzell, E. J.; Lieser, R. M.; Sullivan, M. O.; Chen, W. *ACS Nano* **2020**, *14*, Publisher: American Chemical Society, 12642–12651.

(85) Reddington, S. C.; Howarth, M. *Current Opinion in Chemical Biology* **2015**, *29*, 94–99.

(86) Tang, S.; Xuan, B.; Ye, X.; Huang, Z.; Qian, Z. *Scientific Reports* **2016**, *6*, Publisher: Nature Publishing Group, 25741.

(87) Patterson, D.; Schwarz, B.; Avera, J.; Western, B.; Hicks, M.; Krugler, P.; Terra, M.; Uchida, M.; McCoy, K.; Douglas, T. *Bioconjugate Chemistry* **2017**, *28*, Publisher: American Chemical Society, 2114–2124.

(88) Brune, K. D.; Buldun, C. M.; Li, Y.; Taylor, I. J.; Brod, F.; Biswas, S.; Howarth, M. *Bioconjugate Chemistry* **2017**, *28*, Publisher: American Chemical Society, 1544–1551.

(89) Muik, A.; Reul, J.; Friedel, T.; Muth, A.; Hartmann, K. P.; Schneider, I. C.; Münch, R. C.; Buchholz, C. J. *Biomaterials* **2017**, *144*, 84–94.

(90) Mao, H.; Hart, S. A.; Schink, A.; Pollok, B. A. *Journal of the American Chemical Society* **2004**, *126*, Publisher: American Chemical Society, 2670–2671.

(91) Jaroszewicz, W.; Morcinek-Orłowska, J.; Pierzynowska, K.; Gaffke, L.; Węgrzyn, G. *FEMS Microbiology Reviews* **2022**, *46*, fuab052.

(92) Lino, C. A.; Caldeira, J. C.; Peabody, D. S. *Journal of Nanobiotechnology* **2017**, *15*, 13.

(93) Hassani-Mehraban, A.; Creutzburg, S.; van Heereveld, L.; Kormelink, R. *BMC Biotechnology* **2015**, *15*, 80.

(94) Barassi, C.; Soprana, E.; Pastori, C.; Longhi, R.; Buratti, E.; Lillo, F.; Marenzi, C.; Lazzarin, A.; Siccardi, A. G.; Lopalco, L. *Journal of Virology* **2005**, *79*, Publisher: American Society for Microbiology, 6848–6858.

(95) Caldeira, J. C.; Peabody, D. S. *Journal of Nanobiotechnology* **2011**, *9*, 22.

(96) Sun, Y.; Sun, Y.; Zhao, R. *Journal of Bioscience and Bioengineering* **2017**, *124*, 242–249.

(97) Marcandalli, J. et al. *Cell* **2019**, *176*, 1420–1431.e17.

(98) Ellis, D. et al. *Cell Reports* **2023**, *42*, 113552.

(99) Hutchinson, G. B. et al. *Nature Communications* **2023**, *14*, Publisher: Nature Publishing Group, 6195.

(100) Stephanopoulos, N.; Tong, G. J.; Hsiao, S. C.; Francis, M. B. *ACS Nano* **2010**, *4*, Publisher: American Chemical Society, 6014–6020.

(101) Mohsen, M. O.; Vogel, M.; Riether, C.; Muller, J.; Salatino, S.; Ternette, N.; Gomes, A. C.; Cabral-Miranda, G.; El-Turabi, A.; Ruedl, C.; Kundig, T. M.; Dermime, S.; Knuth, A.; Speiser, D. E.; Bachmann, M. F. *Frontiers in Immunology* **2019**, *10*, Publisher: Frontiers, DOI: 10.3389/fimmu.2019.01015.

(102) Tumban, E.; Peabody, J.; Peabody, D. S.; Chackerian, B. *Vaccine* **2013**, *31*, 4647–4654.

(103) Lensch, V.; Gabba, A.; Hincapie, R.; Bhagchandani, S. H.; Basak, A.; Alam, M. M.; Irvine, D. J.; Shalek, A. K.; Johnson, J. A.; Finn, M. G.; Kiessling, L. L. Glycan-costumed virus-like particles promote type 1 anti-tumor immunity, 2024.

(104) Chung, Y. H.; Cai, H.; Steinmetz, N. F. *Advanced Drug Delivery Reviews* **2020**, *156*, 214–235.

(105) Glasgow, J. E.; Capehart, S. L.; Francis, M. B.; Tullman-Ercek, D. *ACS Nano* **2012**, *6*, Publisher: American Chemical Society, 8658–8664.

(106) Lavelle, L.; Michel, J.-P.; Gingery, M. *Journal of Virological Methods* **2007**, *146*, 311–316.

(107) Ashley, C. E.; Carnes, E. C.; Phillips, G. K.; Durfee, P. N.; Buley, M. D.; Lino, C. A.; Padilla, D. P.; Phillips, B.; Carter, M. B.; Willman, C. L.; Brinker, C. J.; Caldeira, J. d. C.; Chackerian, B.; Wharton, W.; Peabody, D. S. *ACS Nano* **2011**, *5*, Publisher: American Chemical Society, 5729–5745.

(108) Kolesanova, E. F.; Melnikova, M. V.; Bolshakova, T. N.; Rybalkina, E. Y.; Sivov, I. G. *Acta Naturae* **2019**, *11*, 98–101.

(109) Aanei, I. L.; ElSohly, A. M.; Farkas, M. E.; Netirojjanakul, C.; Regan, M.; Taylor Murphy, S.; O'Neil, J. P.; Seo, Y.; Francis, M. B. *Molecular Pharmaceutics* **2016**, *13*, Publisher: American Chemical Society, 3764–3772.

(110) Aanei, I. L.; Huynh, T.; Seo, Y.; Francis, M. B. *Bioconjugate Chemistry* **2018**, *29*, Publisher: American Chemical Society, 2526–2530.

(111) Hu, H.; Masarapu, H.; Gu, Y.; Zhang, Y.; Yu, X.; Steinmetz, N. F. *ACS Applied Materials & Interfaces* **2019**, *11*, Publisher: American Chemical Society, 18213–18223.

(112) Park, J.; Gao, H.; Wang, Y.; Hu, H.; Simon, D. I.; Steinmetz, N. F. *Journal of Materials Chemistry B* **2019**, *7*, Publisher: The Royal Society of Chemistry, 1842–1846.

(113) Obermeyer, A. C.; Capehart, S. L.; Jarman, J. B.; Francis, M. B. *PLOS ONE* **2014**, *9*, Publisher: Public Library of Science, e100678.

(114) McNeale, D.; Dashti, N.; Cheah, L. C.; Sainsbury, F. *WIREs Nanomedicine and Nanobiotechnology* **2023**, *15*, Publisher: John Wiley & Sons, Ltd, e1869.

(115) Aanei, I. L.; Glasgow, J. E.; Capehart, S. L.; Francis, M. B. In *Virus-Derived Nanoparticles for Advanced Technologies: Methods and Protocols*, Wege, C., Lomonossoff, G. P., Eds.; Methods in Molecular Biology; Springer: New York, NY, 2018, pp 303–317.

(116) Glasgow, J. E.; Asensio, M. A.; Jakobson, C. M.; Francis, M. B.; Tullman-Ercek, D. *ACS Synthetic Biology* **2015**, *4*, Publisher: American Chemical Society, 1011–1019.

(117) Herbert, F. C.; Brohlin, O. R.; Galbraith, T.; Benjamin, C.; Reyes, C. A.; Luzuriaga, M. A.; Shahrivarkevishahi, A.; Gassensmith, J. J. *Bioconjugate Chemistry* **2020**, *31*, Publisher: American Chemical Society, 1529–1536.

(118) O'Neil, A.; Prevelige, P. E.; Basu, G.; Douglas, T. *Biomacromolecules* **2012**, *13*, Publisher: American Chemical Society, 3902–3907.

(119) O'Neil, A.; Reichhardt, C.; Johnson, B.; Prevelige, P. E.; Douglas, T. *Angewandte Chemie International Edition* **2011**, *50*, 7425–7428.

(120) Wu, M.; Brown, W. L.; Stockley, P. G. *Bioconjugate Chemistry* **1995**, *6*, 587–595.

(121) Rhee, J.-K.; Hovlid, M.; Fiedler, J. D.; Brown, S. D.; Manzenrieder, F.; Kitagishi, H.; Nycholat, C.; Paulson, J. C.; Finn, M. G. *Biomacromolecules* **2011**, *12*, Publisher: American Chemical Society, 3977–3981.

(122) Fiedler, J. D.; Brown, S. D.; Lau, J.; Finn, M. *Angewandte Chemie (International ed. in English)* **2010**, *49*, 9648–9651.

(123) Das, S.; Zhao, L.; Crooke, S. N.; Tran, L.; Bhattacharya, S.; Gaucher, E. A.; Finn, M. G. *Biomacromolecules* **2020**, *21*, Publisher: American Chemical Society, 2432–2439.

(124) Charpilienne, A.; Nejmeddine, M.; Berois, M.; Parez, N.; Neumann, E.; Hewat, E.; Trugnan, G.; Cohen, J. *Journal of Biological Chemistry* **2001**, *276*, Publisher: Elsevier, 29361–29367.

(125) Brillault, L.; Jutras, P. V.; Dashti, N.; Thuenemann, E. C.; Morgan, G.; Lomonossoff, G. P.; Landsberg, M. J.; Sainsbury, F. *ACS Nano* **2017**, *11*, Publisher: American Chemical Society, 3476–3484.

(126) Robert, M.-A.; Lytvyn, V.; Deforet, F.; Gilbert, R.; Gaillet, B. *Molecular Biotechnology* **2017**, *59*, 9–23.

(127) Kaczmarczyk, S. J.; Sitaraman, K.; Young, H. A.; Hughes, S. H.; Chatterjee, D. K. *Proceedings of the National Academy of Sciences* **2011**, *108*, Publisher: Proceedings of the National Academy of Sciences, 16998–17003.

(128) Research, C. f. B. E. a. *FDA* **2024**, Publisher: FDA.

(129) Wang, D.; Tai, P. W. L.; Gao, G. *Nature Reviews Drug Discovery* **2019**, *18*, Publisher: Nature Publishing Group, 358–378.

(130) Manchester, M.; Singh, P. *Advanced Drug Delivery Reviews* **2006**, *58*, 1505–1522.

(131) Singh, P.; Prasuhn, D.; Yeh, R. M.; Destito, G.; Rae, C. S.; Osborn, K.; Finn, M. G.; Manchester, M. *Journal of Controlled Release* **2007**, *120*, 41–50.

(132) Kaiser, C. R.; Flenniken, M. L.; Gillitzer, E.; Harmsen, A. L.; Harmsen, A. G.; Jutila, M. A.; Douglas, T.; Young, M. J. *International Journal of Nanomedicine* **2007**, *2*, 715–733.

(133) Lam, P.; Steinmetz, N. F. *WIREs Nanomedicine and Nanobiotechnology* **2018**, *10*, e1487.

(134) Andrzej S. Pitek; Jameson, Slater A.; Veliz, Frank A.; Shukla, Sourabh; Steinmetz, Nicole F. *Biomaterials* **2016**, *89*, 89–97.

(135) Lee, K. L.; Shukla, S.; Wu, M.; Ayat, N. R.; El Sanadi, C. E.; Wen, A. M.; Edelbrock, J. F.; Pokorski, J. K.; Commandeur, U.; Dubyak, G. R.; Steinmetz, N. F. *Acta Biomaterialia* **2015**, *19*, 166–179.

(136) Azizgolshani, O.; Garmann, R. F.; Cadena-Nava, R.; Knobler, C. M.; Gelbart, W. M. *Virology* **2013**, *441*, 12–17.

(137) Zhou, Y.; Maharaj, P. D.; Mallajosyula, J. K.; McCormick, A. A.; Kearney, C. M. *Molecular Biotechnology* **2015**, *57*, 325–336.

(138) Maharaj, P. D.; Mallajosyula, J. K.; Lee, G.; Thi, P.; Zhou, Y.; Kearney, C. M.; McCormick, A. A. *International Journal of Molecular Sciences* **2014**, *15*, Number: 10 Publisher: Multidisciplinary Digital Publishing Institute, 18540–18556.

(139) Smith, M. L.; Corbo, T.; Bernales, J.; Lindbo, J. A.; Pogue, G. P.; Palmer, K. E.; McCormick, A. A. *Virology* **2007**, *358*, 321–333.

(140) Sun, S.; Li, W.; Sun, Y.; Pan, Y.; Li, J. *Biochemical and Biophysical Research Communications* **2011**, *407*, 124–128.

(141) Fang, P.-Y.; Gómez Ramos, L. M.; Holguin, S. Y.; Hsiao, C.; Bowman, J. C.; Yang, H.-W.; Williams, L. D. *Nucleic Acids Research* **2017**, *45*, 3519–3527.

(142) Pan, Y.; Jia, T.; Zhang, Y.; Zhang, K.; Zhang, R.; Li, J.; Wang, L. *International Journal of Nanomedicine* **2012**, *7*, 5957–5967.

(143) Yao, Y.; Jia, T.; Pan, Y.; Gou, H.; Li, Y.; Sun, Y.; Zhang, R.; Zhang, K.; Lin, G.; Xie, J.; Li, J.; Wang, L. *International Journal of Molecular Sciences* **2015**, *16*, Number: 4 Publisher: Multidisciplinary Digital Publishing Institute, 8337–8350.

(144) Wu, M.; Sherwin, T.; Brown, W. L.; Stockley, P. G. *Nanomedicine: Nanotechnology, Biology and Medicine* **2005**, *1*, 67–76.

(145) Sun, Y.; Sun, Y.; Zhao, R.; Gao, K. *BMC Biotechnology* **2016**, *16*, 46.

(146) Henke, S.; Rohmann, A.; Bertling, W.; Dingermann, T.; Zimmer, A. *Pharmaceutical Research* **2000**, *17*, 1062–1070.

(147) Sakai, C.; Hosokawa, K.; Watanabe, T.; Suzuki, Y.; Nakano, T.; Ueda, K.; Fujimuro, M. *Biochemical and Biophysical Research Communications* **2021**, *581*, 103–109.

(148) Schoonen, L.; Maassen, S.; Nolte, R. J. M.; van Hest, J. C. M. *Biomacromolecules* **2017**, *18*, Publisher: American Chemical Society, 3492–3497.

(149) Pretto, C.; van Hest, J. C. M. *Bioconjugate Chemistry* **2019**, *30*, Publisher: American Chemical Society, 3069–3077.

(150) Wu, Z.; Bayón, J. L.; Kouznetsova, T. B.; Ouchi, T.; Barkovich, K. J.; Hsu, S. K.; Craig, S. L.; Steinmetz, N. F. *Nano Letters* **2024**, *24*, Publisher: American Chemical Society, 2989–2997.

(151) Hartman, E. C.; Jakobson, C. M.; Favor, A. H.; Lobba, M. J.; Álvarez-Benedicto, E.; Francis, M. B.; Tullman-Ercek, D. *Nature Communications* **2018**, *9*, Number: 1 Publisher: Nature Publishing Group, 1385.

(152) Pistono, P. E.; Huang, P.; Brauer, D. D.; Francis, M. B. *ACS Chemical Biology* **2022**, Publisher: American Chemical Society, DOI: 10.1021/acschembio.2c00318.

(153) Blanco, E.; Shen, H.; Ferrari, M. *Nature Biotechnology* **2015**, *33*, 941–951.

(154) Mitchell, M. J.; Billingsley, M. M.; Haley, R. M.; Wechsler, M. E.; Peppas, N. A.; Langer, R. *Nature Reviews Drug Discovery* **2021**, *20*, 101–124.

(155) Wen, A. M.; Steinmetz, N. F. *Chemical Society Reviews* **2016**, *45*, Publisher: The Royal Society of Chemistry, 4074–4126.

(156) Dedeo, M. T.; Finley, D. T.; Francis, M. B. In *Progress in Molecular Biology and Translational Science*, Howorka, S., Ed.; Molecular Assembly in Natural and Engineered Systems, Vol. 103; Academic Press: 2011, pp 353–392.

(157) Wu, W.; Hsiao, S. C.; Carrico, Z. M.; Francis, M. B. *Angewandte Chemie (International ed. in English)* **2009**, *48*, 9493–9497.

(158) Lundstrom, K. *Diseases* **2018**, *6*, Number: 2 Publisher: Multidisciplinary Digital Publishing Institute, 42.

(159) Rothbard, J. B.; Jessop, T. C.; Lewis, R. S.; Murray, B. A.; Wender, P. A. *Journal of the American Chemical Society* **2004**, *126*, Publisher: American Chemical Society, 9506–9507.

(160) Daniels, D. S.; Schepartz, A. *Journal of the American Chemical Society* **2007**, *129*, Publisher: American Chemical Society, 14578–14579.

(161) McNaughton, B. R.; Cronican, J. J.; Thompson, D. B.; Liu, D. R. *Proceedings of the National Academy of Sciences* **2009**, *106*, Publisher: National Academy of Sciences Section: Biological Sciences, 6111–6116.

(162) Lawrence, M. S.; Phillips, K. J.; Liu, D. R. *Journal of the American Chemical Society* **2007**, *129*, 10110.

(163) Lechanteur, A.; Sanna, V.; Duchemin, A.; Evrard, B.; Mottet, D.; Piel, G. *Nanomaterials* **2018**, *8*, Number: 5 Publisher: Multidisciplinary Digital Publishing Institute, 270.

(164) Ni, C.-Z.; Syed, R.; Kodandapani, R.; Wickersham, J.; Peabody, D. S.; Ely, K. R. *Structure* **1995**, *3*, 255–263.

(165) Galaway, F. A.; Stockley, P. G. *Molecular Pharmaceutics* **2013**, *10*, Publisher: American Chemical Society, 59–68.

(166) Knapman, T. W.; Morton, V. L.; Stonehouse, N. J.; Stockley, P. G.; Ashcroft, A. E. *Rapid Communications in Mass Spectrometry* **2010**, *24*, 3033–3042.

(167) Kato, Y.; Ozawa, S.; Miyamoto, C.; Maehata, Y.; Suzuki, A.; Maeda, T.; Baba, Y. *Cancer Cell International* **2013**, *13*, 89.

(168) Thompson, D. B.; Cronican, J. J.; Liu, D. R. *Methods in enzymology* **2012**, *503*, 293–319.

(169) Lyskov, S. et al. *PLOS ONE* **2013**, *8*, Publisher: Public Library of Science, e63906.

(170) Der, B. S.; Kluwe, C.; Miklos, A. E.; Jacak, R.; Lyskov, S.; Gray, J. J.; Georgiou, G.; Ellington, A. D.; Kuhlman, B. *PLOS ONE* **2013**, *8*, Publisher: Public Library of Science, e64363.

(171) Dou, J.; Doyle, L.; Jr. Greisen, P.; Schena, A.; Park, H.; Johnsson, K.; Stoddard, B. L.; Baker, D. *Protein Science* **2017**, *26*, 2426–2437.

(172) Romero, P. A.; Arnold, F. H. *Nature Reviews Molecular Cell Biology* **2009**, *10*, Number: 12 Publisher: Nature Publishing Group, 866–876.

(173) Reetz, M. T. *Angewandte Chemie International Edition* **2013**, *52*, 2658–2666.

(174) Boyatzis, A. E.; Bringans, S. D.; Piggott, M. J.; Duong, M. N.; Lipscombe, R. J.; Arthur, P. G. *Journal of Proteome Research* **2017**, *16*, Publisher: American Chemical Society, 2004–2015.

(175) Martino, M. L.; Crooke, S. N.; Manchester, M.; Finn, M. *Biomacromolecules* **2021**, *22*, 3332–3341.

(176) Strauss, J. H.; Sinsheimer, R. L. *Journal of Molecular Biology* **1963**, *7*, 43–54.

(177) Stonehouse, N. J.; Stockley, P. G. *FEBS Letters* **1993**, *334*, 355–359.

(178) Clogston, J. D.; Patri, A. K. In *Characterization of Nanoparticles Intended for Drug Delivery*, McNeil, S. E., Ed.; Methods in Molecular Biology; Humana Press: Totowa, NJ, 2011, pp 63–70.

(179) Søndergaard, C. R.; Olsson, M. H. M.; Rostkowski, M.; Jensen, J. H. *Journal of Chemical Theory and Computation* **2011**, *7*, Publisher: American Chemical Society, 2284–2295.

(180) Olsson, M. H. M.; Søndergaard, C. R.; Rostkowski, M.; Jensen, J. H. *Journal of Chemical Theory and Computation* **2011**, *7*, Publisher: American Chemical Society, 525–537.

(181) Fittipaldi, A.; Ferrari, A.; Zoppé, M.; Arcangeli, C.; Pellegrini, V.; Beltram, F.; Giacca, M. *The Journal of Biological Chemistry* **2003**, *278*, 34141–34149.

(182) Preta, G.; Cronin, J. G.; Sheldon, I. M. *Cell Communication and Signaling* **2015**, *13*, 24.

(183) Thompson, D. B.; Villaseñor, R.; Dorr, B.; Zerial, M.; Liu, D. R. *Chemistry & Biology* **2012**, DOI: 10.1016/j.chembiol.2012.06.014.

(184) Futaki, S.; Nakase, I. *Accounts of Chemical Research* **2017**, *50*, Publisher: American Chemical Society, 2449–2456.

(185) Lv, H.; Zhang, S.; Wang, B.; Cui, S.; Yan, J. *Journal of Controlled Release* **2006**, *114*, 100–109.

(186) Hunter, A. C.; Moghimi, S. M. *Biochimica et Biophysica Acta (BBA) - Bioenergetics* **2010**, *1797*, 1203–1209.

(187) Evans, B. C.; Nelson, C. E.; Yu, S. S.; Beavers, K. R.; Kim, A. J.; Li, H.; Nelson, H. M.; Giorgio, T. D.; Duvall, C. L. *JoVE (Journal of Visualized Experiments)* **2013**, e50166.

(188) Nguyen, L. T.; Atobe, K.; Barichello, J. M.; Ishida, T.; Kiwada, H. *Biological and Pharmaceutical Bulletin* **2007**, *30*, 751–757.

(189) Kumar, Y.; Kuche, K.; Swami, R.; Katiyar, S. S.; Chaudhari, D.; Katare, P. B.; Banerjee, S. K.; Jain, S. *International Journal of Pharmaceutics* **2020**, *573*, 118889.

(190) Junutula, J. R. et al. *Nature Biotechnology* **2008**, *26*, 925–932.

(191) Okeley, N. M.; Miyamoto, J. B.; Zhang, X.; Sanderson, R. J.; Benjamin, D. R.; Sievers, E. L.; Senter, P. D.; Alley, S. C. *Clinical Cancer Research* **2010**, *16*, Publisher: American Association for Cancer Research Section: Cancer Therapy: Preclinical, 888–897.

(192) Doronina, S. O.; Toki, B. E.; Torgov, M. Y.; Mendelsohn, B. A.; Cerveny, C. G.; Chace, D. F.; DeBlanc, R. L.; Gearing, R. P.; Bovee, T. D.; Siegall, C. B.; Francisco, J. A.; Wahl, A. F.; Meyer, D. L.; Senter, P. D. *Nature Biotechnology* **2003**, *21*, 778–784.

(193) Sutherland, M. S. K.; Sanderson, R. J.; Gordon, K. A.; Andreyka, J.; Cerveny, C. G.; Yu, C.; Lewis, T. S.; Meyer, D. L.; Zabinski, R. F.; Doronina, S. O.; Senter, P. D.; Law, C.-L.; Wahl, A. F. *Journal of Biological Chemistry* **2006**, *281*, Publisher: Elsevier, 10540–10547.

(194) Koga, Y.; Manabe, S.; Aihara, Y.; Sato, R.; Tsumura, R.; Iwafuji, H.; Furuya, F.; Fuchigami, H.; Fujiwara, Y.; Hisada, Y.; Yamamoto, Y.; Yasunaga, M.; Matsumura, Y. *International Journal of Cancer* **2015**, *137*, 1457–1466.

(195) Hietpas, R. T.; Jensen, J. D.; Bolon, D. N. A. *Proceedings of the National Academy of Sciences* **2011**, *108*, Publisher: National Academy of Sciences Section: Biological Sciences, 7896–7901.

(196) Neun, B. W.; Dobrovolskaia, M. A. In *Characterization of Nanoparticles Intended for Drug Delivery*, McNeil, S. E., Ed.; Methods in Molecular Biology; Humana Press: Totowa, NJ, 2011, pp 215–224.

(197) Gasteiger, E.; Hoogland, C.; Gattiker, A.; Duvaud, S.; Wilkins, M. R.; Appel, R. D.; Bairoch, A. In *The Proteomics Protocols Handbook*, Walker, J. M., Ed.; Humana Press: Totowa, NJ, 2005, pp 571–607.

(198) IPC 2.0: prediction of isoelectric point and pKa dissociation constants | Nucleic Acids Research | Oxford Academic (accessed 10/26/2021).

(199) Lobba, M. J.; Fellmann, C.; Marmelstein, A. M.; Maza, J. C.; Kissman, E. N.; Robinson, S. A.; Staahl, B. T.; Urnes, C.; Lew, R. J.; Mogilevsky, C. S.; Doudna, J. A.; Francis, M. B. *ACS Central Science* **2020**, *6*, Publisher: American Chemical Society, 1564–1571.

(200) Maza, J. C.; Ramsey, A. V.; Mehare, M.; Krska, S. W.; Parish, C. A.; Francis, M. B. *Organic & Biomolecular Chemistry* **2020**, *18*, Publisher: The Royal Society of Chemistry, 1881–1885.

(201) Bird, R. E.; Lemmel, S. A.; Yu, X.; Zhou, Q. A. *Bioconjugate Chemistry* **2021**, *32*, Publisher: American Chemical Society, 2457–2479.

(202) Cielens, I.; Ose, V.; Petrovskis, I.; Strelnikova, A.; Renhofa, R.; Kozlovska, T.; Pumpens, P. *FEBS Letters* **2000**, *482*, 261–264.

(203) Rumnieks, J.; Ose, V.; Tars, K.; Dislers, A.; Strods, A.; Cielens, I.; Renhofa, R. *Virology* **2009**, *391*, 187–194.

(204) Ronzitti, G.; Gross, D.-A.; Mingozzi, F. *Frontiers in Immunology* **2020**, *11*, Publisher: Frontiers, DOI: 10.3389/fimmu.2020.00670.

(205) Shukla, S.; Eber, F. J.; Nagarajan, A. S.; DiFranco, N. A.; Schmidt, N.; Wen, A. M.; Eiben, S.; Twyman, R. M.; Wege, C.; Steinmetz, N. F. *Advanced Healthcare Materials* **2015**, *4*, _eprint: https://onlinelibrary.wiley.com/doi/pdf/10.1002/adhm.201400641, 874–882.

(206) Arnida; Malugin, A.; Ghandehari, H. *Journal of Applied Toxicology* **2010**, *30*, 212–217.

(207) Liu, X.; Wu, F.; Tian, Y.; Wu, M.; Zhou, Q.; Jiang, S.; Niu, Z. *Scientific Reports* **2016**, *6*, Number: 1 Publisher: Nature Publishing Group, 24567.

(208) De Ruiter, M. V.; van der Hee, R. M.; Driessen, A. J. M.; Keurhorst, E. D.; Hamid, M.; Cornelissen, J. J. L. M. *Journal of Controlled Release* **2019**, *307*, 342–354.

(209) Valegård, K.; Liljas, L.; Fridborg, K.; Unge, T. *Nature* **1990**, *345*, Number: 6270 Publisher: Nature Publishing Group, 36–41.

(210) Horn, H. W.; Swope, W. C.; Pitera, J. W.; Madura, J. D.; Dick, T. J.; Hura, G. L.; Head-Gordon, T. *The Journal of Chemical Physics* **2004**, *120*, 9665–9678.

(211) Lu, C.; Wu, C.; Ghoreishi, D.; Chen, W.; Wang, L.; Damm, W.; Ross, G. A.; Dahlgren, M. K.; Russell, E.; Von Bargen, C. D.; Abel, R.; Friesner, R. A.; Harder, E. D. *Journal of Chemical Theory and Computation* **2021**, *17*, Publisher: American Chemical Society, 4291–4300.

(212) Humphrey, W.; Dalke, A.; Schulten, K. *Journal of Molecular Graphics* **1996**, *14*, 33–38, 27–28.

(213) Gowers, R. J.; Linke, M.; Barnoud, J.; Reddy, T. J. E.; Melo, M. N.; Seyler, S. L.; Domański, J.; Dotson, D. L.; Buchoux, S.; Kenney, I. M.; Beckstein, O. *Proceedings of the 15th Python in Science Conference* **2016**, Conference Name: Proceedings of the 15th Python in Science Conference, 98–105.

(214) Michaud-Agrawal, N.; Denning, E. J.; Woolf, T. B.; Beckstein, O. *Journal of Computational Chemistry* **2011**, *32*, 2319–2327.

(215) GraphPad Prism 10 Curve Fitting Guide - Equation: Boltzmann sigmoid (accessed 11/06/2023).